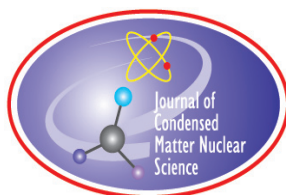


JOURNAL OF CONDENSED MATTER NUCLEAR SCIENCE

Experiments and Methods in Cold Fusion

VOLUME 14, October 2014



JOURNAL OF CONDENSED MATTER NUCLEAR SCIENCE

Experiments and Methods in Cold Fusion

Editor-in-Chief

Jean-Paul Biberian
Marseille, France

Editorial Board

Peter Hagelstein
MIT, USA

Xing Zhong Li
Tsinghua University, China

Edmund Storms
KivaLabs, LLC, USA

George Miley
*Fusion Studies Laboratory,
University of Illinois, USA*

Michael McKubre
SRI International, USA

JOURNAL OF CONDENSED MATTER NUCLEAR SCIENCE

Volume 14, October 2014

© 2014 ISCMNS. All rights reserved. ISSN 2227-3123

This journal and the individual contributions contained in it are protected under copyright by ISCMNS and the following terms and conditions apply.

Electronic usage or storage of data

JCMNS is an open-access scientific journal and no special permissions or fees are required to download for personal non-commercial use or for teaching purposes in an educational institution.

All other uses including printing, copying, distribution require the written consent of ISCMNS.

Permission of the ISCMNS and payment of a fee are required for photocopying, including multiple or systematic copying, copying for advertising or promotional purposes, resale, and all forms of document delivery.

Permissions may be sought directly from ISCMNS, E-mail: CMNSEditor@iscmns.org. For further details you may also visit our web site: <http://www.iscmns.org/CMNS/>

Members of ISCMNS may reproduce the table of contents or prepare lists of articles for internal circulation within their institutions.

Orders, claims, author inquiries and journal inquiries

Please contact the Editor in Chief, CMNSEditor@iscmns.org or webmaster@iscmns.org



JOURNAL OF CONDENSED MATTER NUCLEAR SCIENCE

Volume 14

2014

CONTENTS

EDITORIAL

LETTER TO THE EDITOR

- Comment on the Article ‘Simulation of Crater Formation on LENR Cathodes Surfaces’ 1
M. Tsirlin

RESEARCH ARTICLES

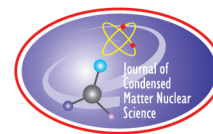
- Response to Comment on the Article ‘Simulation of Crater Formation on LENR Cathodes Surfaces’ 5
Jacques Ruer
- Evidence for Excess Energy in Fleischmann–Pons-Type Electrochemical Experiments 15
D.D. Domínguez, A.E. Moser and J.H. He
- The Use of CR-39 Detectors in LENR Experiments 29
P.A. Mosier-Boss, L.P.G. Forsley and P.J. McDaniel
- Transient Vacancy Phase States in Palladium after High Dose-rate Electron Beam Irradiation 50
Mitchell Swartz and Peter L. Hagelstein
- On the Mechanism of Tritium Production in Electrochemical Cells 61
Stanislaw Szpak and Frank Gordon
- The Pd + D Co-Deposition: Process, Product, Performance 68
Stanislaw Szpak
- Cathode to Electrolyte Transfer of Energy Generated in the Fleischmann–Pons Experiment 76
Stanislaw Szpak and Frank Gordon

Sonofusion: Ultrasound-Activated He Production in Circulating D ₂ O <i>Roger S. Stringham</i>	79
Low-energy Nuclear Reactions Driven by Discrete Breathers <i>V.I. Dubinko</i>	87

Editorial

It is my great pleasure to introduce this new volume of the Journal of Condensed Matter Nuclear Science. This is another living testimony to the excellent work achieved by so many scientists from worldwide who continue in the field in spite of the difficulties due to the lack of acknowledgment by our peers. In this volume, there is for the first time in this journal an exchange between two scientists discussing a previous work through comments of an article. I think that this is very important, because nobody holds the truth, and because experiments as well as theories can be criticized. All the papers in this journal are anonymously peer reviewed, but it is up to each reader to also be a reviewer.

Jean-Paul Biberian
(Editor-in-Chief)
October 2014



Letter to the Editor

Comment on the article ‘Simulation of Crater Formation on LENR Cathodes Surfaces’

M. Tsirlin*

University of Missouri-SKINR, MO, 65211-7010, USA

Abstract

Formation of small craters on the surface of Pd cathode during electrolysis in electrolytes based on heavy water is sometimes interpreted as a consequence of low-temperature nuclear reactions. In this note we discuss the validity of these statements.

© 2014 ISCMNS. All rights reserved. ISSN 2227-3123

Keywords: Craters, Low-Energy Nuclear Reactions, Origin, Pd cathodes

Reference [1] discusses the processes of heat transfer which accompany the local emission of heat on the surface of Pd craters during the electrolytic hydrogenation (or deuteration). However, these notes are not about the model presented in the paper, or the corresponding results of the calculations. Reference [1] attracts the reader's attention with the bold assertion, accompanied by appropriate references, about nuclear reactions as a cause of formation of these craters. So, in the first sentence of the Abstract Ruer argues: “Many authors reported the presence of small-size craters on the surface of cathodes after Low-Energy Nuclear Reaction (LENR)”. The author continues: “It is conjectured the craters result from violent reactions, perhaps of nuclear origin.” Moreover, in the discussion following this, the author repeatedly reiterated this statement, without giving any arguments in its favor. It should be said that this statement about the probably nuclear origin of the craters is widespread in LENR literature. Interestingly, Mizuno, perhaps one of the first who found the craters on the surface of metals during electrolytic hydrogenation [2], does not say anything about its nuclear origin, but astutely points out the heterogeneity of the electric field on the cathode's surface and the possibility of local hydrogen recombination associated with this heterogeneity. In a comprehensive review [3], which discusses the morphological and energetic characteristics of the craters, Nagel made reasonable suggestions about the expediency of studies of the craters to understand LENR.

However, in a number of publications, some of which are cited in Ref. [1], the authors report on experimental results, which, in their opinion, are evidence of the localization of nuclear reactions in the craters. In some cases, this assertion is not supported by any experimental justification [4,5]. In others [6–8] the authors adduce the results

*E-mail: tsirlin.mark@hotmail.com

of SEM-EDS analysis of the craters, which they say prove its nuclear nature. For example, Ref. [6] reported SEM detection of Ti, Mn, Fe, Cr and Ni on the surface of the cathode. The authors believe that the nuclear origin of these elements is proved by their absence in the starting metal. The weakness of this argument is that, as shown in numerous experiments, the cathode surface has always been contaminated by various metal and non-metal impurities during the process of electrolysis. This is particularly the case with experiments by Energetics Technologies [9]. The distribution of these elements over the cathode surface is very uneven. It replicates the non-uniformity of the electric field. In addition, metal elements as Ni, Na, K, Li (the latter found by XRD method in the form of lithium aluminate LiAlO_2) have been detected time and again after electrolysis experiments. Such contamination on the cathodes surface has been observed in open cells as well as in closed ones. Here is another typical example. Reference [7] reported the detection with EDS of Al, O, Ca, Mg and Si in the craters (or “blisters,” in the terminology of the authors). The blisters formed on the surface of the Pd cathode during the co-deposition process. The authors believe that the detected elements are products of nuclear reactions. Interestingly, all the newly formed nuclei are stable. Anyway, there is no mention of the presence of any radiation sources of charged particles or photons, except for point sources of IR radiation. There are Al, Mg, Ca, Si, Zn at concentrations up to 20% revealed in the zone close to the blisters. Naturally, these impurities exist on the cathode surface not in elemental form, but in the form of binary and multicomponent high-enthalpy phases (oxides, oxycarbides, spinels, aluminates, etc.).

It is alleged that these impurities have a nuclear origin, because otherwise, according to the authors, they should be uniformly distributed over the cathode surface. This argument is incorrect because intensive surface diffusion of elements in the process of electrolysis occurs, due to strong heterogeneity of the electric field at the cathode surface^a. Therefore, we cannot exclude the high probability of concentrated contaminants near the craters. Regarding the results of the EDS analysis of Pd cathodes reported in Ref. [8], the detection of the high concentration of Ag in the craters testifies only to rapid Ag migration, perhaps involving electro-capillary effect, from the lead wire to the cathode surface. This is likely because the authors have presented analytical data for the part of the cathode surface close to the contact zone. It should be borne in mind that reliable identification of Ag in Pd matrix with EDS method is possible only at very high concentrations of Ag due to the overlap $L\beta_1\text{Pd}$ and $L\alpha_1\text{Ag}$ spectral lines. The authors did not assess the amount of heat that would be generated by such a highly developed reaction of the nucleus of Pd with a proton (deuteron) and the formation of an Ag nucleus. A rough estimate shows that in this case the Pd sample must instantly evaporate, not to mention other, more dramatic consequences. A large number of analyses of the craters carried out by Energetics Technologies (Israel) with SEM and XRD methods. They can be summarized as follows:

- (1) The craters arise on the Pd cathode during electrolysis with electrolytes made from light or heavy water.
- (2) The craters appear when there is excess heat production, but they also appear when there is no excess heat.
- (3) The crater areas usually do not contain impurities other than carbon and platinum.
- (4) The concentration of Pt in the melted zone is increased, as compared with the rest of the cathode surface; that is easy to explain due to the phase transition of the first kind and by the higher melting point of Pt, as compared to that of Pd.
- (5) The experimentally observed concentration of the craters is so low that the total amount of heat required for their formation is incomparably smaller than the experimentally measured excess heat, when heat is detected. Thus if we assume that all excess heat, e.g., 1 J is realized through formation of the craters, the craters have to cover the entire surface of the cathode with a mean density of $10^6 - 10^7 \text{ cm}^{-2}$. The experimentally measured concentration of craters is just about 5–6 orders of magnitude less than this; hence, the corresponding amount of heat cannot be detected by any known calorimeter.

^aThis effect is caused, for example, by growth of the secondary and negative Pd crystals during the electrolytic process. Certainly, simultaneously with Pd, all other elements move onto the cathode surface. This is a very important circumstance that should not be overlooked.

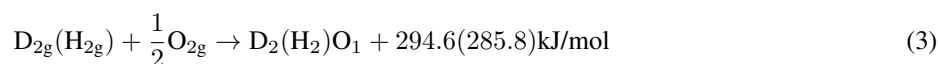
The absence of radiation from LENR is usually explained by the dissipation of the energy in the lattice (e.g., by a change in its phonon or plasmon spectra). However, if we assume the craters are of nuclear origin, we must also assume that the zone of their thermal influence is very small, and has no effect on the energy spectrum of the metal as a whole.

Of course, the possibility that nuclear reactions form the craters cannot be excluded from consideration. However, this hypothesis should be substantiated only with detection products of such reactions located close to the crater area. On the other hand, searching for the nuclear products should be preceded by the search of the less exotic sources of heat as the cause of the phenomenon.

An example of such mundane sources may be, e.g., reaction of recombination of atomic deuterium (hydrogen):



Release of the heat of recombination due to a local fast desorption of D (H) at loading ≈ 1 , is quite sufficient, as is evident from (1) and (2), to melt the corresponding mass of Pd ($\Delta H_m \text{Pd} = 16.7 \text{ kJ/g} - \text{at.}$). This is true, as is easily seen, and for smaller ratios D/Pd, especially in view of the high probability of the oxidation reaction of deuterium (hydrogen):



The high probability of reaction (3) is conditioned by the presence of dissolved oxygen in the electrolyte and free oxygen which is released at the anode, with vigorous stirring of the electrolyte in the inter-electrode space, especially at high current densities. The causes of the local sudden emission of an absorbed gas, the further scenario of the behavior of metal near the places of gas emission, rate of mass and heat transfer of the associated processes should be the subject of further research. By the way, the subject of the article, which was the reason for writing these notes, was research into one of the aspects of the phenomenon under discussion.

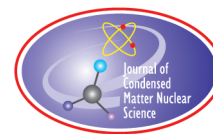
Of course, the simple conjecture offered here suffers from one significant “disadvantage” – it does not need in the excess heat effect (FP-effect) for the interpretation of the phenomenon.

From the above, it seems obvious that the assertion of the nuclear origin of the craters on the basis of the available experimental data is premature. Thus, the question of the nature of the craters, which appear during the electrolytic deuteration or hydrogenation of Pd remains open, and is a challenge for both theorists and experimentalists involved in the unraveling of the mysterious LENR phenomenon.

References

- [1] J. Ruer, Simulation of crater formation on LENR cathode surfaces, *J. Condensed Matter Nucl. Sci.* **4** (2011) 161–172.
- [2] T. Mizuno, *Nuclear Transmutation: The Reality of Cold Fusion*, Infinite Energy Press, Concord, USA, 1998, p. 151.
- [3] D.J. Nagel, Characteristics and energetics of craters in LENR experimental materials, *J. Condensed Matter Nucl. Sci.* **10**(2013) 1–14).
- [4] M. Srinivasan, Hot spots, chain events and micro-nuclear explosions, in Vittorio Violante and Francesca Sarti (Eds.), *Proc. of the 15th Int. Conf. on Condensed Matter Nuclear Science*, Rome, Italy, (2009), pp. 240–245.
- [5] M. Srinivasan, Neutron emission in bursts and hot spots: neutron emission in bursts and hot spots: signature of micro-nuclear explosions? *J. Condensed Matter Nucl. Sci.* **4** (2011) 161–172.

- [6] Y. Toriyabe, T. Miguno, T. Ohmori and Y. Aoki, Elemental analysis of palladium electrodes after Pd/Pd light water critical electrolysis, in A. Takahashi, Ken-ichiro. Ota and Ya. Iwamura (Eds.), *Proc. of the 12th Int. Conf. on Cold Fusion*, Yokohama, Japan (2005), pp. 253–263.
- [7] S. Szpak, P.A. Mosier-Boss, F. Gordon, J. Dea, M. Miles, J. Khim and L. Forsley, LENR research using co-deposition, in D. Nagel and M. Melich (Eds.), *Proc. the 14th Int. Conf. on Condensed Matter Nuclear Science*, Washington, DC (2008), pp. 766–771.
- [8] W. Zhang and J. Dash, Excess heat reproducibility and evidence of anomalous elements after electrolysis in Pd/D₂O + H₂SO₄ electrolysis cells, *13th Int. Conf. on Condensed Matter Nuclear Science*, Sochi, 2007.
- [9] Energetics Technologies (Israel), Unpublished data.



Research Article

Response to Comment on the Article ‘Simulation of Crater Formation on LENR Cathodes Surfaces’

Jacques Ruer*

Abstract

In Ref. [1] the kinetics of heat transfer during the heat bursts at the origin of the formation of the micro-craters on Pd cathodes during electrolysis are discussed. It is assumed that LENR is the source of energy. In Ref. [2], M. Tsirlin made several comments. The present paper answers these comments. Tsirlin thinks it is premature to accept the fact that craters result from LENR events. Other less exotic phenomena should be considered first to explain the crater formation, before nuclear reactions. Tsirlin proposes three potential heat sources:

- (A) Recombination (molarization) of atomic hydrogen.
- (B) Oxidation of the hydrogen at the cathode surface by oxygen evolved at the anode.
- (C) Sudden emissions of the absorbed gas.

The three phenomena are examined and discussed here.

- The energy balance involved during hydrogen recombination does not match the energy required to create a crater.
- The oxidation process of the cathode is too slow to produce eruptions.
- Craters may result from the breakout of some of the many micro-cavities filled with hydrogen at high pressure. Mechanism C might explain some features observed on Pd cathodes, such as craters gathered along surface defects. However, this mechanism alone cannot explain the presence of frozen debris.

It seems that depending on the experimental setup, different types of craters may be obtained. Craters with a smooth internal wall could be developed by fast and very energetic heat bursts, while craters with a rough internal wall would be formed by the breakout of micro-cavities. More investigations are needed.

© 2014 ISCMNS. All rights reserved. ISSN 2227-3123

Keywords: Cooling, Craters, Expansion, Hydride dissociation, LENR, Melting

1. Introduction

In Ref. [1], the kinetics of heat transfer during heat bursts that form micro-craters on Pd cathodes during electrolysis are discussed. In Ref. [2], Tsirlin made several comments about this. The present paper answers these comments.

*E-mail: jsr.ruer@orange.fr

Many authors reported the presence of small size craters on the surface of palladium cathodes after LENR electrolysis experiments. Their structure, observed by scanning electron microscopy, seems to indicate they result from micro-eruptions. In some cases, a fraction of the metal is frozen, as if the metal were melted during the eruption. It is conjectured the craters result from violent reactions [3–7].

In Ref. [1], the kinetics of heat transfer are investigated. The main teachings are summarized in a subsequent section. In the article, it is assumed, as a starting hypothesis, that the violent reactions are of nuclear origin.

This assumption prompted comments from Tsirlin [2], summarized below. For Tsirlin, accepting that craters result from LENR events is clearly premature. He proposes some non-nuclear phenomena which should be considered first in order to find out their potential contribution to crater formation.

These comments and suggestions are quite interesting. As an answer to Tsirlin's comments, the phenomena proposed are briefly examined.

2. Simulation of heat Flow During Crater Formation – A Summary of Ref. [1]

The crater diameters generally range between 2 and 50 μm . A few are larger. In most cases, the craters are circular. Some of them exhibit evident signs of fusion of a fraction of the solids. Kim [3] and Nagel [4] proposed a correlation between the crater diameters and the energy involved in their formation. Starting from the corresponding assumption, it can be derived that the enthalpy released raises the temperature of the crater content to about 2000 K.

The purpose of Ref. [1] was to examine the heat transfer between a small quantity of metal at 2000 K and the surroundings by cooling via conduction and radiation. The aim was to determine within an order of magnitude the maximum duration of the event before complete cooling. The simulation considers an initial sphere of metal at 2000 K embedded in the bulk of metal. The model calculates the temperature evolution by conduction.

Because of the small dimensions of the objects considered, the cooling rate is extremely fast. For example, a 50 μm diameter crater is cooled in less than 1 μs .

If the metal piece at 2000 K is located at the surface of the cathode, some heat is lost by radiation. It is shown that radiative cooling has little influence.

The model does not need a physical explanation of why the temperature of a metal piece is suddenly brought at 2000 K. The same model can be used to simulate heat bursts other than LENR. On the other hand, the model does not give any hint about the origin of the energy. It teaches only that if heat bursts occur, the lifetime of the hot spots is very short.

Several difficulties are raised by the simulation, which are listed in paragraph §5 of [1]. A paradox appears, because if LENR phenomena develop on particular structures of the solids (Nuclear Active Environment), these structures should be destroyed as the solid melts down, so that the reaction should stop immediately.

3. Summary of the Comments Made by Tsirlin [2]

Tsirlin took the opportunity to comment my paper to stress that the origin of craters is a subject which deserves caution. In LENR literature, it is widely believed that the origin of cratering is of some form of nuclear energy. In Tsirlin's view, many arguments in favor of this assertion are questionable.

Tsirlin discusses the detection of transmutation products. My own competences do not allow me to make any comment in this field, so I leave it to others to address this point.

Regarding the craters, Tsirlin is in the best position to comment on the pictures in Ref. [1], as he was involved in the project which published the pictures reproduced in Figs. 3 and 4. The studies performed at Energetics Technologies allow Tsirlin to make important statements which are taken into consideration here:

- The craters arise on palladium cathodes in electrolytes made with light or heavy water.

Table 1. Basic hypotheses.

<i>Hypothesis 1</i>	The solids involved in the crater formation are PdH _x hydrides, with $x \approx 1$
<i>Hypothesis 2</i>	The crater is formed by a sudden heat burst originating from the solids contained within the crater volume before the eruption
<i>Hypothesis 3</i>	The matter is ejected at high temperature (2000 K)

- Craters are observed with or without generation of excess heat.
- The surface density of craters is relatively low. Summing up all the energy related to the craters formed on the cathode gives an insignificant power. Whatever the origin of the crater energy, excess heat, when present, is much larger and must be produced by other processes.

Tsirlin considers the assertion about the nuclear origin of the craters premature, and invites us to consider first less exotic sources of heat as cause of the phenomenon.

Three potential sources are proposed:

- (A) Recombination of atomic hydrogen (deuterium).
- (B) Reaction of oxygen coming into contact with the hydrogen loaded cathode because of vigorous stirring of the electrolyte.
- (C) Sudden emission of the absorbed gas.

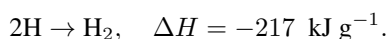
4. Basic Assumptions

The three possible phenomena are examined below. In this discussion, we consider the hypotheses listed in Table 1. They are similar to the assumptions in Ref. [1]. We shall see later that this set of hypotheses may have to be revised.

The three hypotheses are sufficient to retain the main teaching of the model presented in Ref. [1], i.e. the crater formation is very fast. For instance, the heat release and the ejection are completed in less than 1 μ s for a 50 μ m diameter crater.

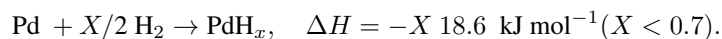
5. MECHANISM A : Atomic Hydrogen Recombination

The recombination of atomic hydrogen into molecules yields a large quantity of heat:



In fact, the hydrogen contained in the palladium cathode is not in a free atomic form, but it is instead dissolved in the metallic matrix or combined as hydride. When hydrogen gas is put in contact with palladium, the sequence of reactions summarized in Fig. 1 takes place:

According to the literature [8], the complete sequence corresponds to the formula:



The above diagram shows the schematic sequence of palladium hydride formation.

The reaction is exothermic, indicating that palladium hydride is a stable compound. Then too, if we consider the reverse reaction, some heat must be brought to the system to dissociate the hydride and release the hydrogen.

The formation enthalpy of palladium hydride PdH_x depends on the loading quantity X.

In Ref. [8], values are given for different values of X at a temperature of 298 K:

$$X < 0.7 : \Delta H = -18.6 \pm 0.3 \text{ kJ mol}^{-1} \text{H (plateau } \alpha - \beta \text{ of the Pd - H}_2 \text{ diagram)}$$

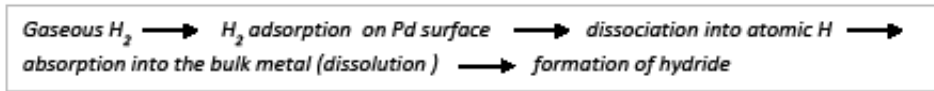


Figure 1. Schematic sequence of palladium hydride formation.

$$0.7 < X < 0.86 : \Delta H = X \cdot 46.71 - 50.38 \text{ kJ mol}^{-1} \text{H}.$$

Figure 2 shows the corresponding relationships. It can be concluded that the hydride stability decreases when the loading factor increases. However, up to $X = 1$ the formation remains fundamentally exothermic.

To simplify the calculations, one can consider the average enthalpy of formation when $X = 1$. To do this and for the ease of the calculation, it is assumed that $\Delta H = 0$ for $X = 1$ (see Fig. 2). The average value obtained is:

$$\Delta H = -16 \text{ kJ mol}^{-1} \text{ for PdH}_x \text{ with } X = 1.$$

This is an approximation, but it is sufficient for the present discussion.

In Ref. [1], Fig. 5 shows that the heating of palladium metal up to 2000 K requires 640 kJ.kg^{-1} , or 68 kJ mol^{-1} . This value includes the latent heat of fusion of palladium (16.7 kJ mol^{-1}), and the sensible heat of the solid and liquid metal.

In fact, these values correspond to the enthalpy of metallic palladium only and do not take into account the presence of the hydrogen dissolved or combined with the metal, which is also involved in the eruption. This should be taken into account. If we assume that the crater results from the melting of PdH up to 2000 K, the overall energy requirement is the sum of:

PdH dissociation	16.0 kJ mol^{-1}	(6)
Pd enthalpy at 2000 K	68.0 kJ mol^{-1}	
$\frac{1}{2} \text{H}_2$ enthalpy at 2000 K	25.4 kJ mol^{-1}	
Total	$109.4 \text{ kJ mol}^{-1}$	

Several authors showed that hydrides may contain a large amount of vacancies, so-called super abundant vacancies (SAV) [9,10]. The total energy of the ordered defect hydride corresponding to the formula Pd_3VacH_4 is lower than

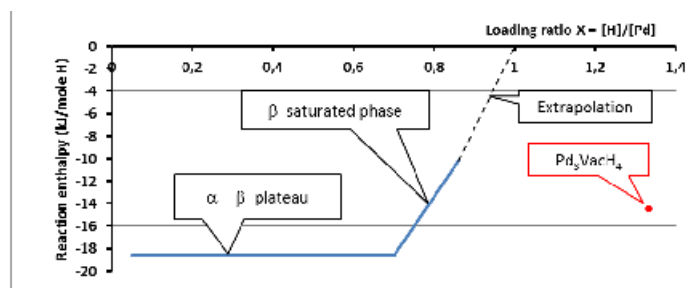


Figure 2. Pd-H₂ reaction enthalpy – the relationship up to $X = 0.86$ is from Ref. [8] – the extrapolation between $X = 0.86$ and 1.0 is from the author – Value for Pd_3VacH_4 is from Ref. [10].

the ideal defect-free PdH hydride. The calculated formation enthalpy of the SAV hydride is -0.15 eV, or -14.49 kJ mol $^{-1}$ H. This value is plotted in Fig. 2 for H/Pd = $4/3 = 1.33$

Hydrogen absorption is exothermic up to high hydrogen loading rates. As a consequence, the outgassing of the hydride following the sequence opposite to the one shown in Fig. 1 must consume heat to proceed.

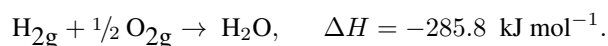
According to this pure thermodynamic analysis, it appears unlikely that a sudden and spontaneous release of hydrogen could generate the heat bursts able to melt the metal accompanied by a flux of hot hydrogen.

6. MECHANISM B: Reaction with Oxygen

Tsirlin invites us to consider the situation in an electrolysis experiment. Oxygen bubbles are generated on the anode, part of the oxygen is dissolved in the electrolyte, and because of the vigorous stirring of the bath, some oxygen bubbles can come close to the cathode. The bubbles are considered to be the major source of oxygen available to drive the oxidation process.

Let us imagine that some bubbles of oxygen come into contact with the cathode and stick to it (Fig. 3).

The following chemical reaction may arise:



The reaction must logically take place at the cathode surface. The hydrogen may be hydrogen adsorbed on the cathode before the approach of the oxygen bubble, or hydrogen absorbed within the palladium migrating to the surface.

Let us consider the case of a $50 \mu\text{m}$ diameter crater. The energy for the formation is 3.2×10^{-5} J if we keep the value of 68 kJ mol^{-1} considered in [1]. According to the discussion in the above, the crater formation energy should rather be $109.4 \text{ kJ mol}^{-1}$. The energy of formation of this $50 \mu\text{m}$ crater is then 5.1×10^{-5} J.

If we make the rough and optimistic assumption that all the heat produced by oxidation of hydrogen is transferred without any loss to the metal, the volume of oxygen required to generate the desired heat burst is at least $V = 2 \times 10^{-12} \text{ m}^3$. This corresponds to a $160 \mu\text{m}$ diameter spherical bubble at standard conditions. The reaction spot is supposed to have the final crater diameter, $50 \mu\text{m}$ in this case, with a surface $S = 2 \times 10^{-9} \text{ m}^2$.

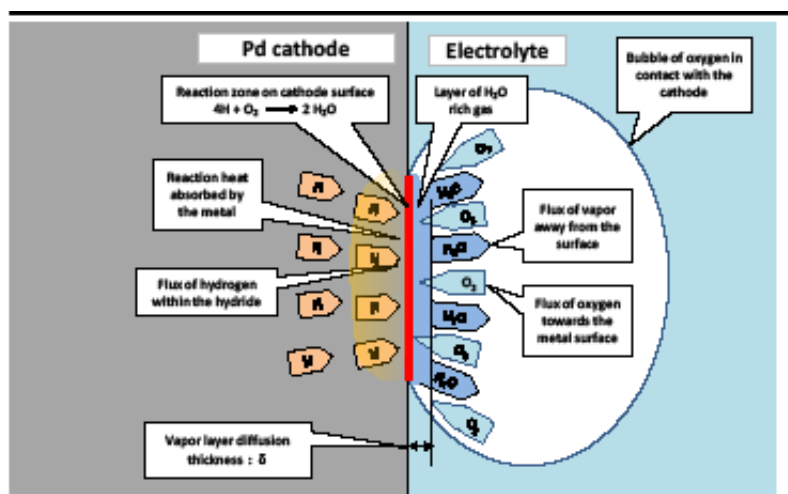


Figure 3. schematic interpretation of an oxygen bubble in contact with the cathode.

Let us further assume that the reaction between hydrogen and oxygen is instantaneous. The reaction rate is then governed by the diffusion of the reactant species:

- Diffusion of oxygen within the bubble towards the cathode surface.
- Diffusion of hydrogen within the metal towards the surface.

The H_2O formed on the metal surface must go away from the surface. The water molecules can only migrate into the oxygen bubble. Inside the bubble attached to the cathode, a layer of vapor-rich gas is formed over the reaction spot. The oxygen must then diffuse across this layer to reach the metal.

Let us consider for example that the vapor layer attached to the metal over the reaction spot has a thickness of $\delta = 10 \mu\text{m}$. The diffusion coefficient of oxygen is about $D = 0.3 \text{ cm}^2 \text{ s}^{-1}$ or $D = 3 \times 10^{-5} \text{ m}^2 \text{ s}^{-1}$.

The order of magnitude of the transfer rate of oxygen is:

$$Q = \frac{DS}{\delta}.$$

The time required to transfer the volume of oxygen V is:

$$t = \frac{V}{Q}, \quad t = \frac{V\delta}{DS}.$$

With the values used here, we obtain $t = 330 \mu\text{s}$

This is only accurate to within an order of magnitude. As the reaction proceeds, the temperature rise can accelerate the diffusion. On the other hand, the vapor layer grows and the oxygen diffusion slows down. In any case, this value is clearly much longer than the crater formation, by almost three orders of magnitude. As a result, the oxidation mechanism is relatively slow and cannot explain alone the fast formation of the craters as they are observed on the surface of cathodes.

7. MECHANISM C: Sudden Emission of Absorbed Gas

The third mechanism proposed by Tsirlin is a sudden emission of the hydrogen absorbed in the cathode.

It is known that in palladium loaded with hydrogen, many cavities appear under the influence of the stresses resulting from the hydrogen introduction into the metal lattice [11]. The cavities are filled with hydrogen gas at a pressure which can be very high.

Super abundant vacancies (SAV) can also generate micro-voids. In Ref. [12], experiments are reported with palladium loaded at high hydrogen pressure at 800°C . The vacancies coalesce together to form pores 20–30 nm in size when present in the interior of the metal, and 1–3 μm when condensed at the surface. Moreover, the pores are dispersed homogeneously across the surface.

We can imagine the following scenario (Fig. 4):

- The hydrogen combines with the palladium to form the β phase hydride.
- Many small cavities appear, as a result of mechanical stresses and dislocations, or as a result of SAV formation. The micro-cavities are filled by hydrogen at high pressure.
- At a given moment, a cavity close to the surface breaks out and the gas content is released into the environment. The local hydrogen pressure is suddenly relieved.
- The pressure of hydrogen is still high in the surrounding hydride and micro-cavities. The distribution of the stresses in the solid becomes non-uniform. This drives the disintegration of the solid locally. Small debris are ejected by the gas flow, leaving a crater.

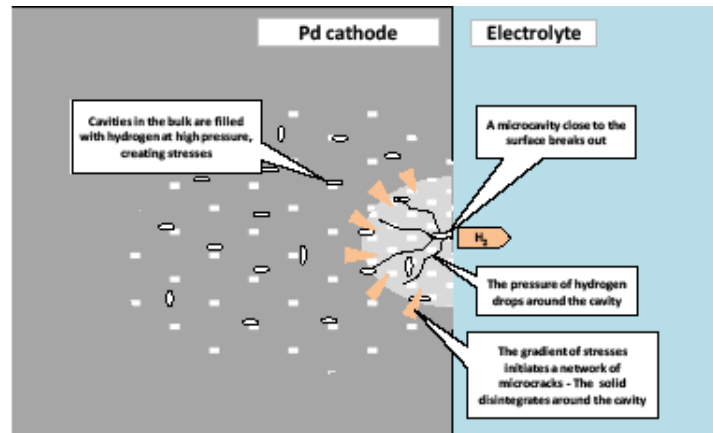


Figure 4. Schematic view of hydride disintegration.

- The order of magnitude of the disintegration propagation is the sound velocity in the solid, in the range of 10^3 m s^{-1} . A small crater can be formed in the very short time calculated in the paper.

This is only an outline of a possible mechanism. More studies would have to be made to refine the process, in particular the mechanical behavior of the solids during the disintegration.

The initial breakout may preferentially occur where the surface presents pre-existing defects. This may explain why craters are sometimes seen aligned along surface defects. See for example Fig. 5, reproduced from Ref. [5].

This model does not explain why the temperature can rise to very high values, or why some craters exhibit frozen material.

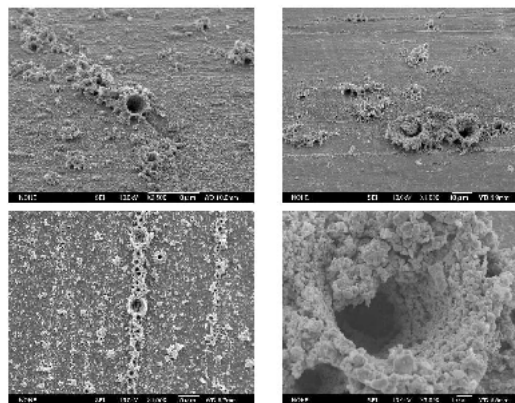


Figure 5. SEM photographs of craters on palladium cathode surfaces after 10 days of electrolysis in a light water based electrolyte. Scale lines are shown at the bottom of each photograph. Ref. [5].

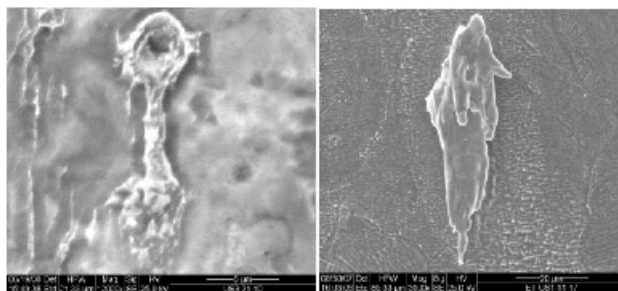


Figure 6. Example of craters found on the surface of palladium cathodes that were subjected to intermittent application of ultrasound cavitation during electrolysis in an heavy water based electrolyte, Ref. [6].

8. Rough Craters and Smooth Craters

All craters are not alike. A review of the different morphologies is given in Ref. [4]. Two different examples are shown in Figs. 5 and 6.

Figure 5 is taken from a paper by Toriyabe, Mizuno and Ohmori [5]. The craters were observed on palladium after 10 days of electrolysis in light water. The craters whose maximum size is over $10\ \mu\text{m}$ are located along pre-existing scratches on the surface. The crater walls are very rough, with many small pieces of fractured metal. No evident sign of fusion can be seen. Mechanism C described above could explain the rough structure observed in this case.

Figure 6 reproduces two micrographs obtained at Energetic Technologies during experimentation with ultrasonic excitation [6]. The picture on the left shows a crater with a diameter of $3\ \mu\text{m}$. Apparently, molten matter spouted out of the crater and formed a kind of “micro-lava flow” about $10\ \mu\text{m}$ long. It seems that the cathode surface was vertical during the test, and the flow is in the downward direction. Tsirlin could confirm this.

The picture on the right shows another microscopic lava flow. It extends $40\ \mu\text{m}$ downwards. The crater at the origin of the flow cannot be seen, probably because it is hidden behind the frozen eruption.

These two examples exhibit smooth crater walls and lava flow shapes.

Let us suppose that the “micro lava flows” were formed by a flow of fused matter which dripped along the surface before cooling down. For cathodes immersed in water, the cooling is very fast. However, if the eruption takes place when a bubble of hydrogen is present at the same location, the cooling may take more time. Heat flow calculations could be made to clarify the phenomena, although this is not done here.

We can calculate the minimum duration of the flow of melted matter as follows:

- The matter located at the tip of the “lava flow” follows a trajectory with a speed which can only be smaller than the free fall velocity of an object induced by gravity
- The distance traveled under the influence of gravity is given by the formula:

$$Z = \frac{1}{2}gt^2 \text{ with } g = 9.81\ \text{m s}^{-2} \text{ acceleration of gravity}$$

- Considering the flow lengths shown in Fig. 6 ($10\text{--}40\ \mu\text{m}$), the duration of the free fall is $1.4 \times 10^{-3}\ \text{s}$ to $2.8 \times 10^{-3}\ \text{s}$.

The actual duration of the flow is probably longer, because the velocity has to be slower than a free fall. The important point is that the phenomena at the origin of the flows visible on the microphotographs lasts several milliseconds. This order of magnitude is completely different from the one considered before ($10^{-6}\ \text{s}$), which resulted from the set of

hypotheses listed in Table 1.

This means that these hypotheses are not valid ways to simulate the phenomena at play during the formation of the craters shown in Fig. 6. Moreover, the shape of the “lava flows” seems to indicate that the gas velocity during the eruption was relatively modest. Otherwise the molten metal would have been ejected away from the cathode surface.

9. Further Research is Needed

The conclusion of this investigation is that additional observations should be undertaken.

In the case of “smooth craters”, it would be important to determine the elemental composition of the “micro lava flows”, to check the influence of a possible contamination.

If a partial melting actually occurs during the formation of some craters, a high temperature is reached during a short time. Molten metal at 2000 K must emit photons in the visible range. The presence of impurities on the surface may lower locally the metal melting temperature, but the peak temperature is still probably sufficient to emit photons in the visible range. A simple method to assess the peak temperature of hot spots is to observe the surface of the cathode during electrolysis. An experiment could be conducted in a dark chamber. A photon detector or a photographic camera with a long exposure time would detect the tiny light flashes emitted by the craters, if any.

In Ref. [7], an infrared camera was used to record the evolution of the temperature of a Pd film co-deposited on a Ni screen during electrolysis in heavy water. Hot spots were detected. The maximum temperature could not be assessed, because it exceeded the IR camera range. It is proposed here to perform similar experiments with photon detectors in the visible range. If the observations are made at two different wavelengths, the ratio of the light energies may give an indication of the temperature level reached.

It is conjectured that no photons in the visible range will be observed under the experimental conditions producing rough craters. In contrast, the formation of smooth craters should be characterized by light emissions, if the morphology of these craters results from partial melting.

10. Conclusions

Tsirlin considers that the assertion about the nuclear origin of craters is premature and that other prosaic sources of energy should be investigated first. He proposes three potential phenomena that should be evaluated. As an answer, this paper presents a first approach of the three proposed mechanisms:

- *A- Recombination of atomic hydrogen:* The hydrogen dissolved in the metal is in monoatomic form. The hydrogen absorption in palladium is exothermic. From a pure thermodynamic point of view, the reverse reaction (dissociation of the hydride, followed by the recombination of the hydrogen molecule) can only consume heat. Therefore, this mechanism cannot explain the spontaneous heat bursts observed.
- *B- Reaction with oxygen:* The hydrogen on the palladium surface can react with oxygen present in the bath. However, the reaction velocity is limited by the diffusion of the reactant species. This mechanism cannot proceed at the rate required to generate the heat bursts able to form craters.
- *C- Sudden emissions of absorbed gas:* Palladium loaded with hydrogen contains many micro-cavities filled with hydrogen at high pressure. Some cavities located close to the surface can break-out and initiate the formation of craters. This mechanism can explain the role of surface defects in the crater localization. However, it cannot explain the presence of melted matter found in some cases.

While some craters have a rough surface, which might be explained by mechanism C, others exhibit smooth shapes, indicating that melting takes place during the eruption. The origin of the fast and strong heat bursts remains unexplained.

It is suggested to confirm the temperature level reached during cratering. This can be done by monitoring the emission of visible photons during electrolysis in an experiment designed for this purpose. A temperature level of 2000 K must be accompanied by the emission of photons in the visible range, which can be easily detected.

In any case, it is important to keep in mind the fact that craters are only one aspect of the phenomena taking place. When an experiment yields some excess heat, the energy involved in the crater eruptions is a small fraction of the total heat measured. This means that the source of the excess heat is not directly linked to the craters. The craters are intriguing objects, which attract attention. It is tempting to draw a relationship between these micro-explosions and the excess heat, but other phenomena must be responsible for the major part of the excess heat.

I want to express my thanks to Tsirlin for his comments. My initial paper was not intended to discuss the LENR phenomenon, but only to have a look at the kinetics of crater formation. His invitation to consider less exotic explanations attracted my interest. For the moment, it does not seem that the potential mechanisms proposed can explain all the features of the craters.

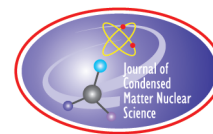
More research is needed.

Acknowledgement

The author is grateful to Jed Rothwell for his editorial suggestions.

References

- [1] J. Ruer, Simulation of crater formation on LENR cathodes surfaces, *J. Condensed Matter Nucl. Sci.* **12** (2013) 1–16.
- [2] M. Tsirlin, The craters and low-energy nuclear reaction (LENR)–Some comments on the article “Simulation of Crater Formation on LENR Cathodes Surfaces”.
- [3] Y.E. Kim, Theory of Bose–Einstein condensation mechanism for deuteron-induced nuclear reactions in micro/nano-scale metal grains and particles, *Naturwissenschaften*, Published online 14 May 2009, DOI 10.1007/s00114-009-0537-6.
- [4] David J. Nagel, Characteristics and energetics of craters in LENR experimental materials, *J. Condensed Matter Nucl. Sci.* **10** (2013) 1–14.
- [5] Y. Toriyabe, T. Mizuno, T. Ohmori and Y. Aoki, Elemental analysis of palladium electrodes after Pd/Pd light water critical electrolysis, *Proc. ICCF 12* (2005). www.icmns.org/iccf12/ToriyabeY.pdf
- [6] I. Dardik, T. Zilov, H. Branover, A. El-Boher, E. Greenspan, B. Khachaturov, V. Krakov, S. Lesin, A. Shapiro and M. Tsirlin, Ultrasonically-excited electrolysis experiments at energetics technologies, *ICCF-14 Int. Conf. on Condensed Matter Nucl. Sci.*, 2008, Washington, DC, USA.
- [7] S. Szpak, P.A. Mosier-Boss and F.E. Gordon, Experimental evidence for LENR in a polarized Pd/D lattice, NDIA 2006 Naval S&T Partnership Conference, Washington DC— <http://lenr-canr.org/acrobat/SzpakSexperiment.pdf>
- [8] Y. Sakamoto, M. Imoto, K. Takai, T. Yanaru and K. Ohshima, Calorimetric enthalpies for palladium-hydrogen (deuterium) systems at H(D) contents up to about $[H]/([D])/[Pd]=0.86$, *J. Phys. Condensed Matter* **8-3229** (1996) <http://iopscience.iop.org/0953-8984/8/18/015>
- [9] Y. Fukai, *The Metal–Hydrogen System*, Springer, Berlin, 2005.
- [10] C. Zhang and A. Alavi, First-principles study of superabundant vacancy formation in metal hydrides, *J. Am. Chem. Soc.* **127** (2005) 9808–9817.
- [11] R.A. Oriani, The physical and metallurgical aspects of hydrogen in metals, *ICCF 4*, 1993.
- [12] D.S. dos Santos, S.S.M. Tavares, S. Miraglia, D. Fruchart and D.R. dos Santos, Analysis of the nanopores produced in nickel and palladium by high hydrogen pressure, *J. Alloys and Compounds* **356–357** (2003) 258–262.



Research Article

Evidence for Excess Energy in Fleischmann–Pons-Type Electrochemical Experiments

D.D. Dominguez*, D.A. Kidwell, K.S. Grabowski and D.L. Knies

Chemistry and Materials Science Divisions, Naval Research Laboratory, Washington, DC 20375-5320, USA

A.E. Moser and J.H. He

Nova Research Inc., Alexandria, VA 22308, USA

Abstract

The production of excess energy in palladium cathodes electrochemically loaded with deuterium (the Fleischmann–Pons Experiment) has been debated in the literature since its first publication in 1989. In a subset of 61 trials, we electrochemically loaded palladium–rhodium foil cathodes with deuterium from alkaline solutions of heavy water in specially designed closed calorimeter cells. We observed excess energy bursts in the range 2.4–44.3 kJ in 6% of these experiments. Additionally, a conservative estimate of the total integrated output energy is greater than the total integrated input energy in these experiments. This paper documents the steps taken to examine these results thoroughly for calibration/measurement errors and instrumental artifacts. A 2.4 kJ energy burst is at least four times greater than the energy released by oxidizing deuterium in the cell headspace. The data and subsequent elimination of alternative explanations for excess energy production lead us to conclude that the excess energy is real and of yet unknown origin.

© 2014 ISCMNS. All rights reserved. ISSN 2227-3123

Keywords: Calorimetry, Deuterium, Excess energy, Palladium

1. Introduction

The most significant claim in the early publications by Fleischmann and Pons was of excess energy production in palladium cathodes electrochemically loaded with deuterium [1–5]. Experiments were described in which “bursts” of excess energy were generated in palladium rod electrodes after several weeks or months of electrolysis. Excess energy produced at high current densities ($500\text{--}1000\text{ mA cm}^{-2}$) was tens of watts over many days and reached a cumulative total of MJ cm^{-3} of palladium and often caused the electrolyte temperature to reach the boiling point. These extraordinary results were attributed to unknown nuclear processes since any other cause such as chemistry or non-nuclear physical energy was implausible [1–5]. The neutron and tritium generation rates were orders of magnitude

*E-mail: dawn.dominguez@nrl.navy.mil. Fax: 011-202-767-0594; Tel: 011-202-767-2998

lower than produced by D–D fusion reactions at high temperatures for the given amounts of excess energy measured. Thus, the excess energy claim seemed to defy conventional understanding of chemistry or nuclear physics and to require new science to explain its origin.

Since the early publications by Fleischmann and Pons, numerous accounts of excess energy production in palladium cathodes electrochemically loaded with deuterium have been reported [6–13]. However, in spite of mounting evidence, criticism has been that the excess energy observed is either due to overlooked chemistry, measurement errors (such as calibration issues), or instrumental artifacts [14,15]. Due to the significant potential scientific and practical payoffs should this evidence be correct, further research has been conducted.

Excess energy in the early Fleischmann and Pons work can be classified as two types: (1) Type A was a relatively constant gain in the power out vs. the power in (Fig. 1a) that starts fairly quickly and is not dependent on the current density. We have seen Type A behavior occasionally in our systems but these offsets ($<10\%$ in our cases) could be dismissed as due to calorimeter calibration shifts or attributed to unknown chemistry. (2) Type B behavior is a large energy burst (Fig. 1b) that happens after considerable electrolysis and was observed in one of the early Fleischmann and Pons experiments [2,3]. These bursts are rarer than Type A behavior but are almost impossible to dismiss as calibration errors or stored energy. For our work, we adopted the sandwich electrode configuration attributed to Vittorio Violanti (ENEA) [13]. Experiments at Energetics Technologies (ET-Omer, Israel), SRI Int. (Menlo Park, CA), and ENEA (Frascati, Italy) have also reported excess energy with varying levels of reproducibility with this electrode configuration. Energetics Technologies found Type B excess energy in eight of approximately 800 experiments ($\sim 1\%$). In six of their experiments, the excess energy measured was 1–3 MJ [16]. In 23 attempts at replicating the Energetics Technologies results, eleven SRI experiments (48%) generated 100–500 kJ excess energy [17,18]. Selecting only those results where the percentage of excess power is at least 50% greater than the input power at any given time, SRI found 4 of 23 (17%) experiments produced an excess but none of these were clearly Type B behavior. Similarly, 4 of 10 (40%) experiments at ENEA produced at least 50% excess power with one of Type B behavior [18,19]. The choice of at least a 50% excess power is arbitrary, but is large enough to exclude measurement artifacts. Other excess energy-producing experiments carried out at ET, SRI and ENEA exhibited smaller power bursts (mW) often seen superimposed on low levels of excess power (mW) lasting for many days (up to 40 days). Although using a different electrochemical cell design, Storms reported that 3 of 80 (4%) Fleischmann–Pons-type experiments showed excess energy [20].

Two types of excess energy are shown in Fig. 1. Figure 1a shows a slow rise in excess energy vs. time. Figure 1b shows a large energy burst that resembles those bursts that are the subject of this paper. The constant rise in excess energy vs. time is often seen and we termed this Type A heat. By integration over a long time, this small excess can be an appreciable amount of excess energy, claimed by some to be above that possible from chemical means or storage. On the other hand, the constant rise could be construed as a calibration error or a change in instrumental calibration.

This paper describes our observations of Type B behavior from a subset of 61 similar cathodes out of more than 300 separate experiments. This subset was chosen to focus on a palladium–rhodium cathode material prepared by the same process from the same source of palladium, alloyed in a similar manner, and electrolyzed in 1 M LiOD electrolyte with Pt anodes. High-quality commercial instrumentation custom designed for these electrochemical studies was used. The data presented do not include results from experiments on pure palladium cathodes, control samples, or cathode materials prepared under other conditions or run with anodes other than Pt.

Our results demonstrate that the large excess energy observed in our experiments was a real phenomenon worthy of scientific inquiry and was NOT due to calibration/measurement errors. Although under different conditions than the sets discussed here, our remaining 240+ experiments showed no excess energy or Type A behavior and therefore will be discussed elsewhere.

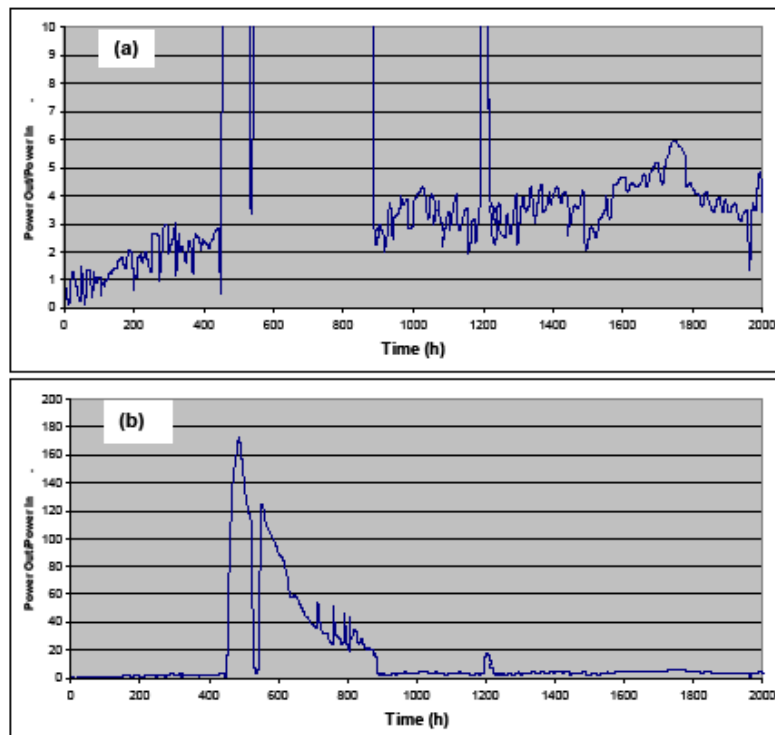


Figure 1. Examples of two types of excess energy taken from the literature. Figure 1a is an expansion of Fig. 1b. The data were acquired in an open cell configuration [2,3] and re-plotted from [2]. A ratio of 1 would indicate that the power out = power in, which would be expected from conventional chemistry.

2. Experimental

2.1. Materials

A 90 at.% palladium–10 at.% rhodium alloy (abbreviated as Pd₉₀Rh₁₀) was prepared using hydrogen-torch melting on an alumina plate. High-purity palladium (99.95%, Produits Artistiques Métaux Précieux (PAMP)) and rhodium were used. In the preparation, rhodium pieces were initially wrapped with palladium foil to reduce rhodium oxidation. The torch melting process lasted for a few minutes until a melt ball formed. After air cooling, the palladium–rhodium alloy was repeatedly cold-rolled and annealed at 850°C in a vacuum furnace (10^{-5} – 10^{-6} Torr) to form 50 μm thick ribbons. The ribbons were then annealed at 450°C for 30 min and 850°C for 90 min in a vacuum furnace. Prior to each new electrochemical experiment, the 50 μm thick foil cathodes were chemically etched in 50% *aqua regia* for 2 min.

Heavy water electrolyte (1 M LiOD) was freshly prepared in a glove bag with an argon atmosphere prior to each new electrochemical experiment by dissolving lithium foil (99.9%, Johnson Matthey) in deuterium oxide (99.9 % isotopic purity, Cambridge Isotope Laboratory). High surface area catalysts, 0.5% palladium on alumina (Sud-Chemie) and Pt electrode on carbon fiber paper (Johnson Matthey), were used to recombine the evolved deuterium and oxygen gases. The recombination catalysts were contained in the perforated chamber above the electrodes near the cell top (Fig. 2).

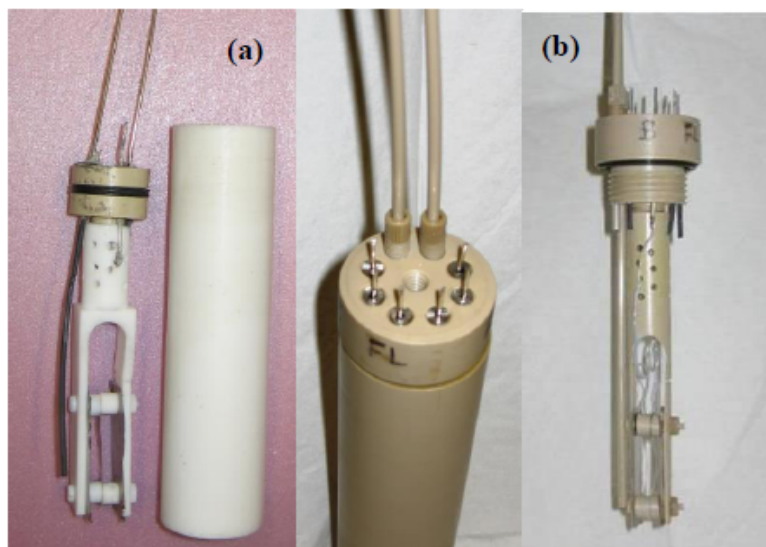


Figure 2. Photographs showing (a) the Teflon cell with PEEK cell top fitted with two syringe needles and black polypropylene tubing for chemical additions to the electrolyte and (b) PEEK cell with PEEK tubing replacing the syringe needles and polypropylene tubing inside the cell.

2.2. Electrolytic cells

Experiments were conducted in two different types of specially designed electrochemical cells. The initial excess energy observation occurred during an electrochemical experiment with a $\text{Pd}_{90}\text{Rh}_{10}$ cathode in an all-Teflon cell (25 mm internal diameter, 13.5 cm length) with a PEEK (PolyEther Ether Ketone) cell top (Fig. 2a). Two stainless steel syringe needles (18 gauge) penetrated through the PEEK top to the cell interior to allow chemical additions to the electrolyte with minimal disturbance. One needle was used as an air vent and the other as an addition port. Black polyethylene tubing was attached to the addition port needle so electrolyte could be drawn into a syringe from the cell bottom during chemical additions and electrolyte exposure to the stainless steel would be minimal (there is some splashing during the cell operation inside the cell). In later experiments, Teflon cells were replaced with identically-sized all-PEEK cells. In the redesigned cells, PEEK tubing (0.125 in, 3.2 mm diameter) replaced the syringe needles to eliminate the possibility of shorts and reduce contamination by metals, in particular, those that might leach from the nickel-plated brass Luer-lock tips. Photos of a PEEK cell and interior PEEK cell parts are presented in Fig. 2b.

Thermodynamically closed (no correction for evolved chemical enthalpy is needed) electrochemical cells were used with the ENEA/Violante “sandwich” electrode configuration. The electrode dimensions for the cells were: cathode (40 mm \times 5 mm \times 50 μm), Pt (99.9%) foil anodes (45 mm \times 20 mm \times 180 μm) and cathode–anode spacing of 5 mm. Teflon-coated 0.5 mm diameter Pt wires provided connections by spot-welding them to Pt disks and to 1 mm diameter Pt wires extending through the PEEK cell top. The Pt disks made contact with the electrodes through pressure applied by finger tightening screws threaded through the electrodes, Pt disks and PEEK spacers.

2.3. Calorimeter and calibration

The four-position calorimeter, custom made for this application by Hart R&D Inc., Mapleton, UT, was a Peltier-type system with a linear response from 0 to 10 W and ± 1 mW sensitivity. The Hart calorimeter is described in more detail

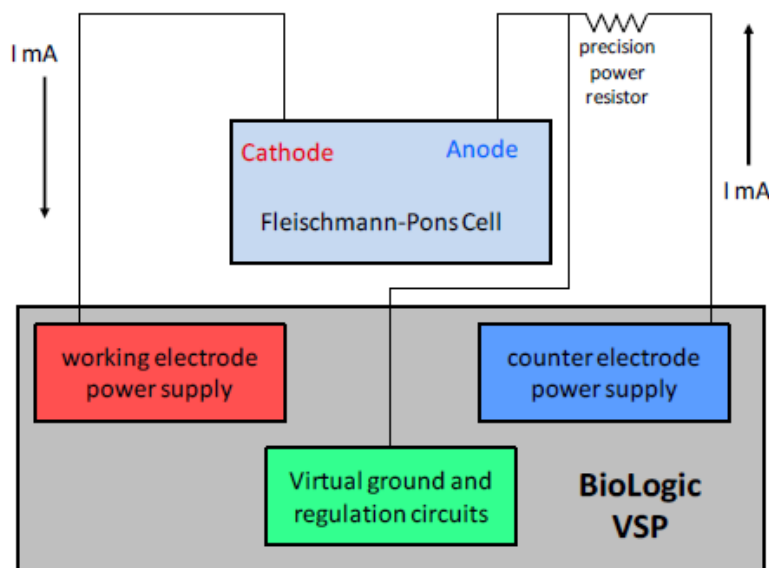


Figure 3. Schematic drawing showing basic experimental design with the Fleischmann–Pons cell, BioLogic VSP power supply, and a precision power resistor.

elsewhere [21,22] and was typically maintained at 25.00, 40.00, or 60.00°C in a water bath with a thermal stability of $\pm 0.002^\circ\text{C}$. The calorimeter was initially and intermittently calibrated using a 2.7 ohm stainless steel-coated Inconel resistor immersed in water inside non-operating cells and with external 100 Ω resistors (calibration heaters) provided for each calorimeter position. Calibration experiments were also run periodically using Pt or Ni foil cathodes in 1 M LiOD, and using Pd foil cathodes in 1 M LiOH with electrolysis occurring. Additionally, each experiment was calibrated during the initial application of power into the cell with the assumption that lower power operation would show no excess energy.

2.4. Experimental procedures and data collection

Calorimetric measurements were carried out isothermally under constant current or constant power conditions. A schematic drawing showing the basic experimental design is shown in Fig. 3. In a given experiment, two or three cells were placed in the calorimeter and run concurrently under identical conditions. Power was supplied to the cells using three of five channels from a computer-controlled power supply (BioLogic VSP Modular Potentiostat/Galvanostat/electrochemical impedance spectroscopy). The input power to an electrochemical cell was determined as the product of the current supplied by the VSP and the cell voltage. Current input to the cell was confirmed by measuring the voltage drop across a wire wound precision power resistor (0.5–5 Ω , 1%, 10 W). Electrolytic loading of a cathode was started at a low current (50 mA) or low power (50 mW) input to the cell. During a typical experiment, the current/power was gradually increased to a maximum of 2 A or 9 W in 8–10 steps of 4–6 h duration each.

Chemical compounds (Raney nickel, cobalt sulfate and nickel sulfate) known to produce oxide or magnetic interfaces on the surface of the cathodes were occasionally added to the electrolyte in attempts to initiate excess energy production. The chemicals (reagent grade) were added to the electrolyte (24 mL) in the cells in 10–50 mg quantities

during cell operation by: (1) placing the additive in a 2 mL all-glass syringe, (2) venting the cell by removing the vent port seal, (3) removing the addition port seal and attaching the syringe to the addition port, (4) pumping electrolyte into and out of the syringe a few times, (5) removing the syringe and resealing the cell. Additions were usually made sequentially in the order listed above once the input power stabilized at its maximum programmed value. Most additions did not produce excess energy. Raney nickel (Raney nickel is a 1:1 alloy by weight of aluminum and nickel and the aluminum undergoes oxidation) reacting with hydroxide is exothermic and 50 mg should produce 488 J from standard heats of formation. Raney nickel reaction with hydroxide is rapid but the heat evolution was often obscured by the endothermic spike due to the addition. In any case, if chemistry were causing the heat bursts, it should occur after every addition.

Four point resistance measurements were made in initial experiments. However, to reduce the measurement complexity and make the system more robust and reliable, these measurements were discontinued in later experiments. It was also our opinion that the information gained from resistance measurements was not worth the risk of a possible extra energy source due to a possible intermittent instrument failure. Limited tritium measurements were made on electrolyte solutions from heat producing and non-heat producing cells before and after electrolysis using the liquid scintillation method on a Beckman LS-6500 Multi-purpose Scintillation Counter. No evidence of tritium production was observed. The cathodes were not checked for tritium.

Electrochemical and calorimetric data were collected at 1 s intervals using EC-Lab software provided by BioLogic. Experiments were carried out in a limited-access building located in a controlled-access laboratory. The building was vibration-isolated and RF-shielded and the laboratory space within was temperature controlled to $20.0 \pm 0.1^\circ\text{C}$. Examination of ingress logs showed that no unauthorized individuals entered around the times of the events.

3. Results and Discussion

During the course of this work, it was determined that many sources of palladium used historically in successful Fleischmann–Pons experiments actually came from one producer (Engelhard). ICP-MS analysis for trace impurities on older cathodes indicated a change likely was made in the palladium processing by the supplier [23]. Older cathodes had Al, Rh, and Pt present whereas newer cathodes had Zr, Hf, and Y, but little Rh or Pt. A change in processing using zirconia crucibles likely occurred to account for the new presence of Zr and Y. The levels of these impurities were in the ppm range so the palladium met the supplier stated purity. However, newer lots did not always etch the same and some were mechanically harder than older lots. The Pd₉₀Rh₁₀ alloy was developed as it was thought the hypothesized processing changes might have been responsible for newer palladium cathodes showing no excess energy (about 100 attempts for us) whereas the success rate claimed for older palladium materials was much higher for other investigators.

The Pd-rich Pd–Rh alloys are an exception to the general rule that Pd alloying results in decreased absorbed hydrogen [24,25]. Desorption via non-electrochemical recombination reactions (Tafel reactions) is less efficient when using Pd–Rh alloy than when using pure Pd [26] potentially allowing more efficient loading. We decided to incorporate Rh at levels near its miscibility point with Pd rather than at trace levels as in the older material. The Pd–Rh alloys are significantly more resistant to chemical etching. This was thought to be important, as the etching step is one of the least controlled steps in the cathode preparation. It was expected the enhanced chemical resistance would allow for more reproducible surface features. It is known that mechanical properties of elemental metals can be improved by even small alloy additions. Also, alloy addition has a pronounced effect on grain size distribution and indentation hardness. Following our standard rolling and annealing procedures, typical grains were 20–60 μm in size. After the *aqua regia* etch, the foils typically exhibited rough grains with steep sides and deep grain boundaries.

Historically, many electrochemical experiments were run for months before excess power was observed. Long run times were hypothesized to concentrate impurities on the cathode surface [7]. Initially, our experiments were carried

out in closed Teflon cells with no capability for chemical additions, and no excess power was produced. To mimic the concentration process and improve the prospects for observing excess power, cells were modified to allow chemical additions. However, prior to the change in cathode material from pure palladium to the Pd₉₀Rh₁₀ alloy, cells run with chemical additions still showed little or no excess power.

The first calorimetric experiment with a Pd₉₀Rh₁₀ foil cathode (cathode #1) and chemical additions showed excess energy. The experiment was carried out in constant current mode at 25°C in a Teflon cell (Fig. 2a) and the data obtained are displayed in Fig. 4. The figure shows plots of electrochemical input and output powers to/from the cell, current,

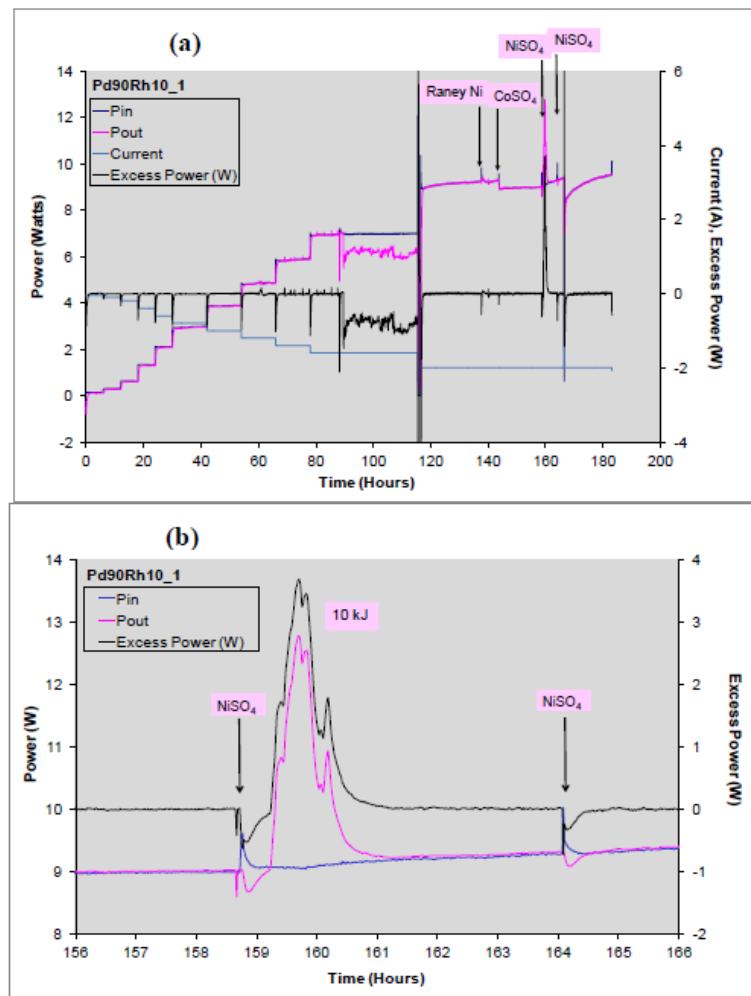


Figure 4. (a) Plots of input power (P_{in}), output power (P_{out}) on left vertical axis, and current, excess power on right vertical axis as a function of time for Pd₉₀Rh₁₀ cathode #1 run at 25°C in a Teflon cell with chemical additions to the 1 M LiOD electrolyte as indicated. Cumulative excess energy is not plotted because of a data gap (due to a loose connection) from 89 to 116 h. (b) An enlargement of the power plots shown in (a) from 156 to 166 h.

and excess power ($P_{\text{out}} - P_{\text{in}}$) vs. time. Input and output powers were calculated continuously. The steady state data during the initial eight step increase in current were fit to provide an in situ calibration, assuming no excess energy was produced during that time. The variation in fitting coefficients between runs was less than 1% over two years, which confirmed the stable performance of the Hart calorimeter. Additional calibrations performed using resistors placed inside the cells agreed with those obtained from the power steps. In other experiments, using pressure vessels and H_2 combustion, the energy produced was within 1% of that calculated from literature value.

After loading the palladium-rhodium cathode (cathode #1), an instability in the P_{out} measurement occurred at about 89 h due to a loose connection on the Hart calorimeter that persisted until the system was temporarily stopped, repaired, and restarted at about 116 h with a constant current of 2 A (Fig. 4). Once the system regained stability, chemical additions (Raney nickel, cobalt sulfate and nickel sulfate) were made to the cell. As shown in Fig. 4, an endothermic transient is observed as the consequence of introducing cooler material into the cell during each addition. About 36 min following the third chemical addition, evidence of excess power appeared in the data. Excess power peaked at a maximum of almost 4 W with 9 W input (42% excess) and persisted for over 90 min (Fig. 4b). A fourth chemical addition (nickel sulfate) was added to the electrolyte solution following appearance of the spike and recovery of the baseline. The fourth addition produced no additional excess energy.

Calculated energy generated during the 90-minute interval was about 10 kJ. Chemical energy produced by metal salt additions cannot account for the excess energy observed. In fact, the most energetic chemical reaction conceivable in the cell would be the combustion of deuterium. That reaction could produce approximately 600 J (see below). The 10 kJ observed in the experiment is at least 15 times greater than the energy released by oxidizing deuterium. It is not known whether chemical impurities were fully or even partially responsible for triggering the energy burst observed. Moreover, since this was the first large excess energy burst seen in our laboratory and metal syringe needles were used, it was hypothesized that a short of the needle to ground could have caused the burst.

Although, calculations could show that a short through the electrolyte would be insufficient to cause the apparent energy, this prospect was thoroughly examined. While there was no evidence that a short had occurred during the excess energy-producing experiment with cathode #1, the cells were redesigned to eliminate the possibility of a short in future experiments. The redesigned cells were all plastic (PEEK) except for the Pt wire feed through penetrating the PEEK cell tops, which were protected with a tight-fitting plug (not shown). Notably, PEEK tubing replaced the metal syringe needles and the polyethylene tubing in the new cells as shown in Fig. 2b.

$\text{Pd}_{90}\text{Rh}_{10}$ cathode #27 was run in an all-PEEK cell without chemical additions. Excess energy was observed with this cathode where an electrical short was thought to be physically impossible. However, a special condition on the external wiring MAY have permitted a short to form intermittently.^a Figure 5 shows the time evolution of the calculated excess power and cumulative excess energy possibly obtained on $\text{Pd}_{90}\text{Rh}_{10}$ cathode #27. At the start of the experiment, the electrochemical cell was operated with a constant current of 20 mA. The current was stepped up to 50 mA at 8 h while maintaining a power balance. But, at 9.6 h the cell began to produce a large amount of excess power and it continued to do so for the next 5 h. During this time, while the input power fluctuated, the power output approached a maximum of ~ 10 W. No chemical additions were intentionally made during this experiment as the step increase in input power was not completed. However, the cell may have been contaminated with chemical impurities that were carried over from additions made in previous experiments as the input tubes were not acid cleaned to avoid degradation

^aBriefly, the VSP can supply the required amount of power without generating an error if there is a direct short of the anode to earth ground, the VSP power supply is in constant power mode, and the electrolyte is 1M. If the VSP were in constant current mode, an error message would be reported during such a short. Errors were not reported during constant current mode operation of cathodes 1 and 60, but were intermittently seen for cathode 27. Regardless of the mode of operation, the resistance of the short to earth ground must be less than 2-3 ohms for the VSP to supply sufficient power to account for the observed heat. We have no evidence that shorts occurred during the observed excess energy events and during the many hours of null results, no errors were ever reported.), then the VSP could not supply sufficient power to account for the observed heat. We have no evidence that shorts occurred during the observed excess energy events and in the many hours of null results, no errors were ever reported.

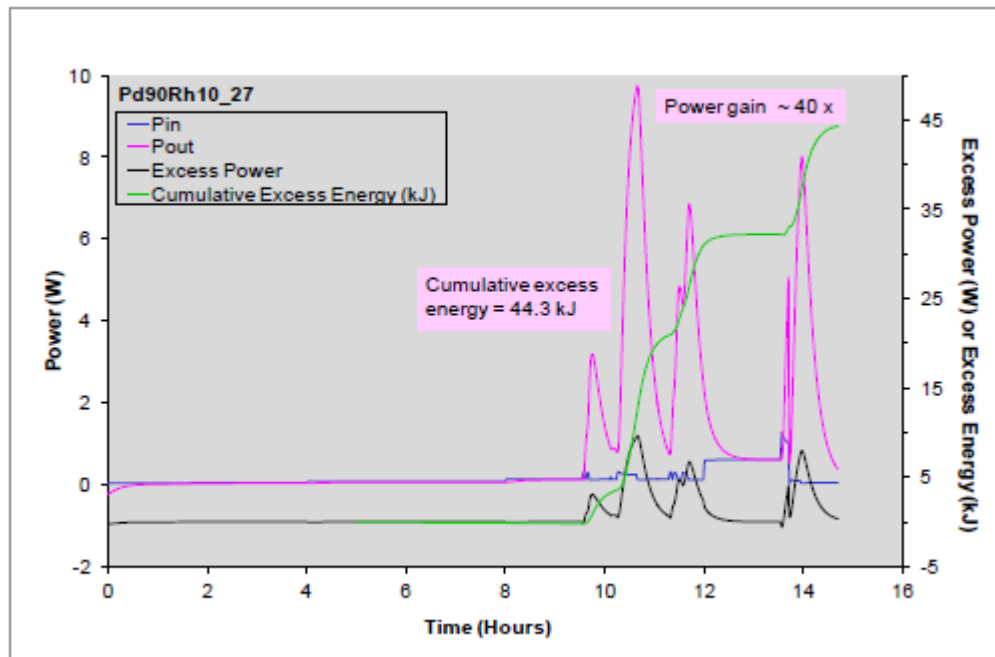


Figure 5. Variation of input power (P_{in}), output power (P_{out}) on left vertical axis and excess power, excess energy on right vertical axis with time for Pd₉₀Rh₁₀ cathode #27 in 1 M LiOD run at 25°C in an all-PEEK cell. The total electrical input energy from 0 to 14.7 h was 8.3 kJ. The cumulative excess energy exceeded the total input energy by 45 kJ.

of the PEEK. The cumulative excess energy generated from the series of bursts was 44 kJ, assuming a short did not occur. This represents a maximum power gain of almost 40 times and an energy gain over 6.

Excess power and cumulative excess energy produced with Pd₉₀Rh₁₀ cathode #54 run in an all-PEEK cell, in constant power mode without chemical additions are shown in Fig. 6. In this instance, the excess power burst occurred with an input power of 4 W and excess power production reached a 2.5 W maximum, or approximately 63% of the input power. The integrated value of excess energy generated from the burst was about 2.4 kJ. The cell returned to power balance after a step increase in power to 7 W. Again, no chemical addition was intentionally made to the electrolyte since the step increase in power was incomplete.

Pd₉₀Rh₁₀ cathode #60 was run in an all-PEEK cell with chemical additions. Excess power and cumulative excess energy obtained in the mostly constant power experiment with cathode #60 are presented in Fig. 7. The figure shows the cell in power balance with $P_{out} = P_{in}$ and excess power equal to near zero at the start of the experiment. The cell remained in power balance during step increases in power to 9 W in constant power mode and for another 2 h near 9 W while in constant current mode. Then, the cell voltage suddenly increased, raising the input power to a preset limit of 12 W, and a large excess power burst was observed, followed by a second similar burst approximately 10 h later. Excess power from these bursts reached ~83% of the input power, or about 10 W maximum. Integrated values of excess energy produced in the two bursts were 18.2 and 14.7 kJ, respectively, which was 6–8 times greater than in cathode #54. The trigger for these excess energy bursts is unknown. The first burst occurred before any chemical addition was intentionally made to the electrolyte. A Raney nickel addition was made prior to the second excess energy burst. However, it is not known whether the addition was in any way responsible for initiating the burst.

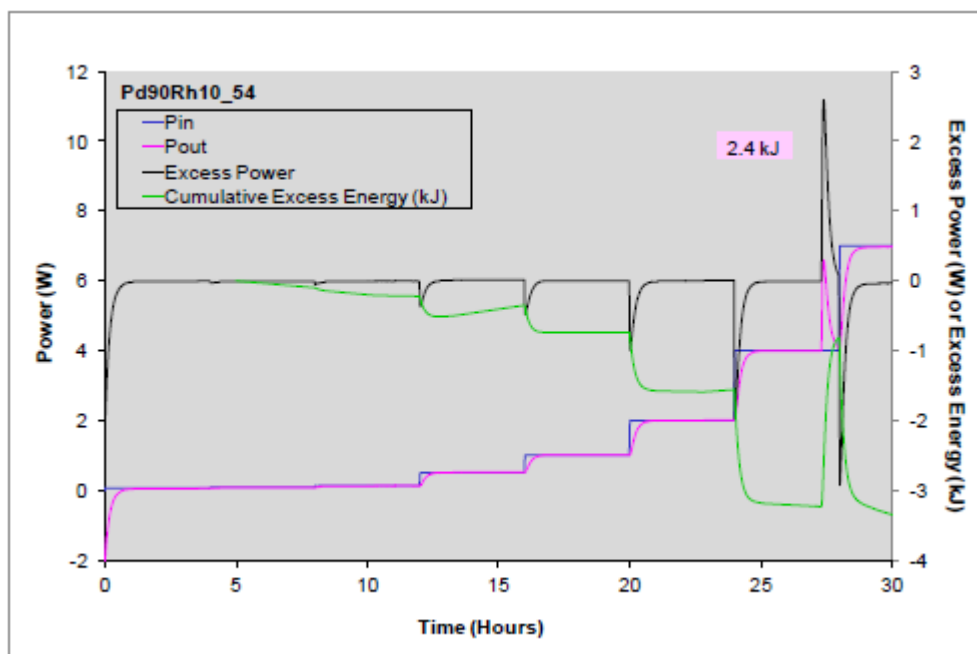


Figure 6. Plots of input power (P_{in}), output power (P_{out}) on left vertical axis and excess power, excess energy on right vertical axis as a function of time for a Pd₉₀Rh₁₀ cathode #54 run at 60°C in an all-PEEK cell with 1 M LiOD.

For a closed electrochemical cell, power output should equal power input. Thus, the expected excess power ($P_{out} - P_{in}$) should equal zero. Deviations from this expectation may be attributed either to simple chemistry or, if shown not to be a measurement artifact, to new science. Energy can be stored in two forms during electrolysis. In the first, energy is used to heat the cell contents. The negative spikes observed in the excess power plot during the power steps are due to the instantaneous change in the electrochemical input power whereas the Hart calorimeter response is limited by its time constant (~ 15 min) needed to heat the components. From several non-energy-producing cells, it takes approximately 8 kJ (7.8 ± 0.6 kJ, $n = 7$) to heat a cell to its steady-state operating temperature with a power input of 9W (see Fig. 7a). This heat can be recovered when power is removed and the cell cools down. The second form is stored chemical energy. The most energetic chemical reaction conceivable in the cell would be combustion of deuterium by oxygen. If only oxygen filled the headspace (~ 25 mL, 1 atm pressure) above the electrolyte (to produce maximum oxidizing energy) and deuterium was somehow sequestered in the palladium cathode and suddenly released to react with the oxygen, approximately 600 J could be produced. This is four times less than the 2.4 kJ observed on the low end of the energy bursts (cathode #54). Furthermore, stored chemistry (the production of H_2 and O_2 is accounted for in our energy balance) is not evident because such stored chemical energy must come from somewhere in addition to the energy used to heat the cell. If there were appreciable stored energy, the cumulative excess energy would be more negative than 8 kJ by that amount of stored chemical energy. This has not been observed in our experiments. The heat pulses cannot arise from the heat content of the cell as there is no known mechanism in an isothermal system by which this heat can be converted to a heat pulse and thereby concentrate the heat. This would violate the first law of thermodynamics. To reiterate, the observed energy bursts must come from some other source

than cumulative stored energy. Although we believe it to be unrealistic, and if one assumed that all the excess input energy went into stored chemical energy powering some unknown chemical reaction (which in itself would be very energy dense) instead of heat, one still could not account for the two cells with Pd₉₀Rh₁₀ cathode #27 (Fig. 5) and cathode #60 (Fig. 7), where the cumulative energy output (~ 25 kJ) greatly exceeds the energy input even considering the 8 kJ necessary to heat the cells.

Following each of these excess energy-producing experiments, an extensive investigation was undertaken to examine the possible cause of these events. These efforts focused on electrical shorting as the only instrumental artifact that could conceivably explain the data. In these investigations, the requirements and consequences of electrical shorts deliberately produced in the power supply, inside the cell or external to the cell and calorimeter were exhaustively explored. Some of the excess power data could be reproduced by shorting the power supply in a certain manner as explained in footnote a. However, the likelihood that a short ($\sim 1 \Omega$) could form and then disappear and reform in the manner necessary to mimic the data (cathode #60) was extremely remote, given the care taken to prevent such an occurrence. Detailed results of our investigations on the effect of electrical shorts in the experiments described will be published separately.

Results of the four excess energy-producing experiments presented have some similarities and differences worth noting. Experiments were all carried out on Pd₉₀Rh₁₀ foil cathodes in 1 M LiOD electrolyte and all displayed large magnitude (≥ 2.4 kJ) excess energy bursts that could not be accounted for by chemistry. Since the cathode volumes were about 0.01 cm^3 , the excess energy generated was approximately 1 MJ cm^{-3} which is similar to that observed by Fleischmann and Pons [1–3]. Two of the four cathodes were run in experiments with constant current while the other two cathodes were run with constant power. The four experiments were run isothermally at three different temperatures, 25, 40, and 60°C, and excess energy bursts were obtained in three different Hart calorimeter positions and run using three different VSP channels. During each excess energy-producing experiment, one or two additional cells, run concurrently under identical conditions in the calorimeter, did not produce excess energy. These disparate results indicate a power supply or calorimeter malfunction is an unlikely source of experimental error. Moreover, there doesn't seem to be any individual temperature, cell, calorimeter position or VSP channel that is particularly favorable for producing the excess energy results observed. In addition, null results acquired on more than 100 other Pd₉₀Rh₁₀ cathodes and on a large set of palladium cathodes run before and after the excess energy results serve as control experiments and provide sufficient evidence that the instruments were performing correctly throughout and measurement or calibration errors were non-existent.

We observed large amounts (tens of kJs) of excess energy in four out of 61 similar experiments ($\sim 6\%$). These bursts are much greater than chemical energy and are similar to those observed in other laboratories. We cannot rule out an instrumental artifact for one cathode. However, the other three cathodes have signatures that differ from a short in substantial ways. For example, cathode #60 requires more power than a short could provide and has none of the disturbances in other channels that would indicate a short. The result from cathode #27 *could* be due to an instrumental artifact caused by a short under very selective conditions as it had disturbances in the other channels and a lower power output which could be provided by the power supply. As such, the demonstration of cathode #27 as an unconventional energy source should be discounted at this time. This particular kind of instrumental artifact will be discussed in detail in a subsequent paper, but an instrumental artifact is not consistent with the results from the other three positive cathodes. Although the number of events is small, these results taken in combination with others acquired under varied conditions reduces the chance of an unrealized systematic error. Thus, we propose that this data set showing large events whose energy production is above chemistry in a thoroughly vetted system demonstrates new science that should be explored.

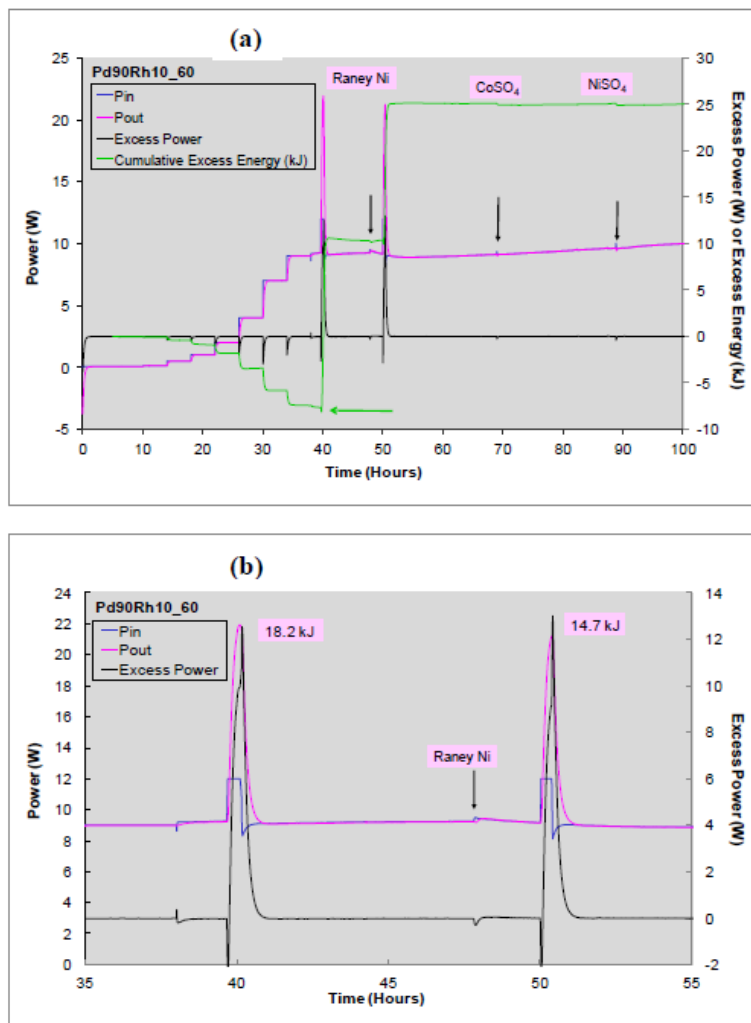


Figure 7. (a) Plots of input power (P_{in}), output power (P_{out}) on left vertical axis and excess power, excess energy on right vertical axis as a function of time for Pd₉₀Rh₁₀ cathode #60 run at 40°C in an all-PEEK cell with chemical additions to the 1 M LiOD electrolyte as indicated. (b) An enlargement of the power plots presented in (a) from 35 to 55 h showing the two large excess power bursts.

4. Conclusions

From over 300 Fleischmann–Pons-type calorimetric experiments, a subset of 61 experiments on a palladium–rhodium alloy cathode material, Pd₉₀Rh₁₀, electrochemically loaded with deuterium in 1 M LiOD electrolyte solution are presented. Three to four of these experiments produced Type B excess energy bursts too large (≥ 2.4 kJ) to be of chemical origin. The large collection of null results confirmed that the instruments were performing correctly and measurement errors were non-existent. We achieved some success initiating a few excess energy events with incubation times of days (vs. weeks or months) using cathodes made with the palladium–rhodium alloy and with chemicals

deliberately added to the cells. Shorter incubation periods can minimize drifts that might occur over long experiment times and, thus, simplify the data analysis and interpretation. The levels of excess energy produced and reproducibility achieved in our experiments is comparable to what has been reported in some of the literature. Attempts to improve the reproducibility and understand the initiation and source of these energy bursts are continuing in our laboratory.

Acknowledgements

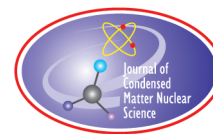
The financial support of the Defense Advanced Research Projects Agency and the Defense Threat Reduction Agency is gratefully acknowledged. The views, opinions, and/or findings contained in this manuscript are those of the authors and should not be interpreted as representing the official views or policies, either expressed or implied, of the Naval Research Laboratory or the Department of Defense.

Approved for Public Release, Distribution Unlimited

References

- [1] M. Fleischmann, S. Pons and M. Hawkins, Electrochemically-induced nuclear fusion of deuterium, *J. Electroanal. Chem.* **261** (1989) 301–308.
- [2] S. Pons, Calorimetry of the palladium–deuterium system, *Proc. of the First Annual Conference on Cold Fusion* (Salt Lake City, UT, 1990), pp. 1–19.
- [3] M. Fleischmann, S. Pons, M.W. Anderson, L.J. Li and M. Hawkins, Calorimetry of the palladium–deuterium–heavy water system, *J. Electroanal. Chem.* **287** (1990) 293–348.
- [4] S. Pons and M. Fleischmann, The calorimetry of electrode reactions and measurements of excess enthalpy generation in the electrolysis of D₂O using Pd-based Cathodes, in: T. Bressani, E. Del Giudice, G. Preparata (Eds.), *The Science of Cold Fusion*, Conference Proc. , Vol. 33 (Italian Physical Society, Bologna, Italy, 1991), pp. 349–362.
- [5] M. Fleischmann and S. Pons, Calorimetry of the Pd–D₂O system: from simplicity via complications to simplicity, *Phys. Lett. A* **176** (1993) 118–129.
- [6] M.C.H. McKubre, R. Rocha-Filho, S.I. Smedley, F.L. Tanzella, S. Crouch-Baker, T.O. Passell and J. Santucci, Isothermal flow calorimetric investigations of the D/Pd system, in: T. Bressani, E. Del Giudice, G. Preparata (Eds.), *The Science of Cold Fusion, Conf. Proc. ,* Vol. 33 (Italian Physical Society, Bologna, Italy, 1991), pp. 419–443.
- [7] M.C.H. McKubre, S. Crouch-Baker, A.M. Riley, S.I. Smedley and F.L. Tanzella, Excess power observations in electrochemical studies of the D/Pd system; the influence of loading, in: *Proc. of the Third Int. Conf. Cold Fusion, “Frontiers of Cold Fusion”* (Universal Academy Press, Tokyo, Japan 1992), pp. 139–150.
- [8] M.C.H. McKubre, S. Crouch-Baker, R.C. Rocha-Filho, S.I. Smedley, F.L. Tanzella, T.O. Passell and J. Santucci, Isothermal flow calorimetric investigations of the D/Pd and H/Pd systems, *J. Electroanal. Chem.* **368** (1994) 55–66.
- [9] M.H. Miles, R.A. Hollins, B.F. Bush, J.J. Lagowski and R.E. Miles, Correlation of excess power and helium production during D₂O and H₂O electrolysis using palladium cathodes, *J. Electroanal. Chem.* **346** (1993) 99–114.
- [10] E. Storms, Measurements of excess heat from a Pons–Fleischmann-Type electrolytic cell using palladium sheet, *Fusion Technol.* **23** (1993) 230–256.
- [11] I. Dardik, T. Zilov, H. Branover, A. El-Boher, E. Greenspan, B. Khachatorov, V. Krakov, S. Lesin and M. Tsirlin, Excess heat in electrolysis experiments at Energetics Technologies, Presented at the *11th Int. Conf. Condensed Matter Nuclear Science*, Marseilles, France, November 1–6, 2004.
- [12] I. Dardik, T. Zilov, H. Branover, A. El-Boher, E. Greenspan, B. Khachatorov, V. Krakov, S. Lesin and M. Tsirlin, Progress in electrolysis experiments at Energetics Technologies, Presented at the *12th Int. Conf. Condensed Matter Nuclear Science*, Yokohama, Japan, November 27–December 2, 2005.
- [13] V. Violante, F. Sarto, E. Castagna, M. McKubre, F. Tanzella, G. Hubler, D. Knies, K. Grabowski, T. Zilov, I. Dardik and C. Sibilia, Joint scientific advances in condensed matter nuclear science, in: *8th Int. Workshop on Anomalies in Hydrogen /Deuterium Loaded Metals*, Sicily (2007) 1–9.
- [14] DoE Review Panel, Report of the Review of Low Energy Nuclear Reactions (2004).

- [15] K.L. Shanahan, Comments on “A new look at low-energy nuclear reaction research”, *J. Environ. Monit.* **12** (2010) 1756–1764.
- [16] I. Dardik, T. Zilov, H. Branover, A. El-Boher, E. Greenspan, B. Khachatorov, V. Krakov, S. Lesin, A. Shapiro and M. Tsirlin, Ultrasonically-excited electrolysis experiments at Energetics Technologies, in: *ICCF-14 Int. Conf. Condensed Matter Nuclear Science*, Washington, DC, USA (2008), pp. 106–122.
- [17] M.C.H. McKubre, The importance of replication, in: *ICCF-14 Int. Conf. Condensed Matter Nuclear Science*, Washington, DC, USA (2008), pp. 673–688.
- [18] M.C.H. McKubre, F.L. Tanzella, I. Dardik, A. El-Boher, T. Zilov, E. Greenspan, C. Sibilila, V. Violante, Replication of Condensed Matter Heat Production, in: *Low-Energy Nuclear Reactions Sourcebook*, J. Marwan (Ed.), ACS Symposium Series 998, Oxford University Press (2008), 219.
- [19] V. Violante, F. Sarto, E. Castagna, M. Sansovini, S. Lecci, D.L. Knies, K.S. Grabowski and G.K. Hubler, Material Science on Pd–D System to Study the Occurrence of Excess Power, in: *ICCF-14 Int. Conf. Condensed Matter Nuclear Science*, Washington, DC, USA (2008), pp. 429–436.
- [20] E. Storms, A study of those properties of palladium that influence excess energy production by the “Pons–Fleischmann” effect, *Infinite Energy* **2** (1996) 50–75.
- [21] S.C. Barrowes and H.E. Bergeson, Linear, high precision, redundant calorimeter, *Fusion Technol.* **26** (1994) 365–368.
- [22] D.D. Dominguez, D.A. Kidwell, D.L. Knies, J.H. He, K.S. Grabowski, G.K. Hubler and V. Violante, Are oxide interfaces necessary in Fleischmann–Pons-Type experiments? *J. Condensed Matter Nucl. Sci.* **8** (2012) 219–230.
- [23] D.A. Kidwell, Considerations for ultra-trace analysis of metals in a palladium matrix, in: *ICCF-14 Int. Conf. Condensed Matter Nuclear Science*, Washington, DC, USA (2008), pp. 180–194.
- [24] A. Zurowski, M. Lukaszewski and A. Czerwinski, Electrosorption of hydrogen into palladium–rhodium alloys, *Electochim. Acta* **51** (2006) 3112–3117.
- [25] A.K.M. Fazel Kibria, Deuterium solubility and electrical resistance of palladium–rhodium alloys, *Int. J. Hydrogen Energy* **25** (2000) 997–1003.
- [26] J. A. Zurowski, M. Lukaszewski, A. Czerwinski, Electrosorption of hydrogen into palladium–rhodium alloys, *Electochim. Acta* **53** (2008) 7812–7816.



Research Article

The Use of CR-39 Detectors in LENR Experiments

P.A. Mosier-Boss*

Research Laboratory of Electronics, Massachusetts Institute of Technology, Cambridge, MA 02139, USA

L.P.G. Forsley

JWK International Corp., Annandale, VA 22003, USA

P.J. McDaniel

University of New Mexico, Albuquerque, NM 87131, USA

Abstract

In this communication, the use of CR-39 detectors to detect energetic charged particles and neutrons in LENR experiments is discussed. The main advantages of these detectors over real-time electronic detectors are its integration capability and its ability to speciate energetic particles. Unlike real-time detectors, CR-39 can be placed in close proximity to the cathode and can be used for both electrolysis experiments and gas loading. These advantages of CR-39 detectors over real time, electronic detectors are particularly important when energetic particle emissions occur either sporadically in bursts or at a low flux.

© 2014 ISCMNS. All rights reserved. ISSN 2227-3123

Keywords: Charged particles, CR-39, Neutrons, Real-time electronic detectors

1. Introduction

Columbia Resin 39 (CR-39) is an allyl glycol carbonate plastic that is optically clear and amorphous. In 1978, Cartwright et al. [1] were the first to show that CR-39 could be used to detect nuclear particles. As an energetic, charged particle traverses through the plastic, it creates along its path an ionization trail that is more sensitive to chemical etching than the bulk material. After etching with an aqueous 6 M NaOH solution between 60 and 70°C for six or more hours, tracks due to the energetic particles remain in the form of pits that can be examined with the aid of an optical microscope. As will be discussed in this communication, the size, depth of penetration, and shape of the track provides information about the mass, charge, energy, and direction of motion of the particle that created the track [2].

Since its introduction as a solid state nuclear track detector (SSNTD), CR-39 has found extensive use as a charged-particle spectrometer to study inertial-confinement-fusion (ICF) plasma [3] and to detect secondary neutrons and cos-

*E-mail: pboss@san.rr.com

Table 1. Summary of LENR Experiments Using CR-39.^a

Researcher	Experiment	Conclusions
X.Z. Li et al. [5]	D ₂ (H ₂) gas loading of Pd foils	Track density: Pd/D ₂ >>>> Pd/H ₂ > D ₂
Jin et al. [6]	D ₂ gas loading of YBCO pellets and powder	Circular tracks with diameters between 2 and 7 μm (for comparison ²⁴¹ Am α tracks have a diameter of 6 μm)
Lipson et al. [7]	Electrochemically load Au/Pd/PdO heterostructures with D. Once loaded put cathode in contact with CR-39 and cycle temperature	Detected tracks consistent with 2.5–3.0 MeV p and 0.5–1.5 MeV t
Roussetski [8]	Electrochemically load Au/Pd/PdO and PdO/Pd/PdO heterostructures with D. Once loaded put cathode in contact with CR-39 and cycle temperature	Detected tracks consistent with ~ 3.0 MeV p, ~ 1 MeV t, triple tracks due to 14.1 MeV n. The number of tritons needed to create triple tracks greater than the yield of DD tritons.
Karabut et al. [9]	Glow discharge of Ti cathodes in D ₂ gas. CR-39 detectors covered in Al foils	Detected 3 MeV p, 1.7 MeV p or 2.3 MeV d, and 13.5 ± 2.0 MeV α
Oriani and Fisher [10]	Pd sheet foil, electrolysis in Li ₂ SO ₄ /D ₂ O, CR-39 placed above and below Pd cathode	Track density of CR-39 used is electrolysis experiments (150–3760 tracks cm^{-2}) greater than CR-39 used in controls (59–541 tracks cm^{-2})
Lipson et al. [11]	Cathode was 50 μm thick Pd foil in contact with CR-39. Electrolysis in Li ₂ SO ₄ /H ₂ O	Tracks were concentrated in areas where the cathode was in contact with the CR-39 detector
Lipson et al. [12]	Cathode was thin Pd films in contact with CR-39. Cu and Al spacers separated the Pd cathode from the detector. Electrolysis in Li ₂ SO ₄ /H ₂ O	Tracks in CR-39 detectors consistent with 1.7 MeV p and 11–16 MeV α
Roussetski et al. [13]	Irradiate TiH _x and TiD _x films with psec laser beam. CR-39 in chamber either bare or covered with Al or Cu films	Detected 3 MeV p, n, and ≥ 10 MeV α
Lipson et al. [14]	TiD _x and Pd/PdO:D _x targets stimulated with a electron beam. Target surrounded by CR-39 covered with various metal foils	Detected 3 MeV p and 11–20 MeV α
Mosier-Boss et al. [15–18]	Pd/D codeposition on Ni screen and Ag, Au, Pt wires in contact with CR-39. Electrolysis in D ₂ O and H ₂ O	Detected tracks due to energetic charged particles and triple tracks due to 14.1 MeV n. Track density: D ₂ O >>>> H ₂ O
Tanzella et al. [19]	Pd/D codeposition on Ag wire in contact with CR-39 covered with either 6 μm Mylar or 60 μm polyethylene	Detected tracks due to 3 MeV p, 2.5 MeV n, 12.6–17.5 MeV p, 14.1 MeV n, and ≥ 12 MeV α

^a p = proton, t = triton, d = deuteron, n = neutron, α = alpha

mic rays at the international space station (ISS) [4]. This detector has also been used in a number of low-energy nuclear reaction experiments for over two decades. These experiments and their results are summarized in Table 1. As shown in Table 1, these detectors have been used in gas phase experiments as well as electrolysis and glow discharge experiments. Hydriding materials used include Pd, Ti, Pd/PdO heterostructures, and YBCO. Energetic particles detected in LENR experiments include protons, alphas, tritons, and neutrons.

Lately, there has been much discussion on the validity of using SSNTDs in place of electronic, real-time detectors in LENR experiments. It has been argued that SSTNDs are a relatively new detector material whose use has not been fully vetted by the scientific community. In this communication, we indicate that the physics community has indeed fully evaluated and characterized SSNTDs such as CR-39 for energetic particle detection. We also discuss the advantages and disadvantages of SSNTDs and show that these detectors are not only ideal but are, in many cases, the detector of choice for use in LENR experiments to elucidate the nuclear nature of the phenomenon.

2. Overview of Real-time Methods to Detect Neutrons and Charged Particles

2.1. Neutron detection

Neutrons have no charge. Consequently, these particles cannot be detected directly. Instead indirect methods are used. In these methods, the neutrons interact with other atomic nuclei and it is the response of that interaction that is detected. In general, there are two categories of neutron interaction with other atomic nuclei. These are neutron capture or elastic scattering. In the neutron capture method, a target nucleus captures a neutron to create an unstable nucleus. This unstable nucleus then spontaneously loses energy by either emitting ionizing charged particles or gamma/X-rays. These are the decay products that are then detected. Because the cross sections for neutron capture are lower at high neutron energies, moderators are typically used to slow down the neutrons so that capture can occur. As a result, the energy of the neutron cannot be determined by this method. Neutron detectors that rely upon neutron capture include BF_3 and ^3He detectors. The efficiencies of these detectors for fast neutrons are of the order of 7.6×10^{-3} when in direct contact with the source [19]. The efficiency decreases with d^2 , where d is the distance between the source and the detector. Srinivasen et al. [20] used three BF_3 counters embedded in a paraffin moderator block to monitor neutron emissions from a commercial Milton Roy diffusion type hydrogen generator. The cathode was comprised of 16 $\text{Pd}_{0.75}\text{Ag}_{0.25}$ straws that were 3 mm OD and 200 mm in length. The total surface area was 301 cm^2 , much larger than is typically used in most LENR experiments. Neutrons were observed to occur in bursts. De Ninno et al. [21,22] used a BF_3 detector to monitor deuterium gas loading of 100 g of Ti shavings. Changes in temperature and pressure were used to create nonequilibrium conditions in adsorption/desorption of deuterium in the lattice. Neutron emissions were observed to occur in bursts that were between 35 and 500 times above background.

In the elastic scattering method, the neutron scatters off nuclei causing the struck nucleus to recoil. The recoiling nucleus can ionize and excite additional atoms through collisions. These collisions produce charge and/or scintillation light which are then detected. Since these types of detectors do not require moderators, the energy of the neutrons can be determined. However, these detectors also respond to gamma and X-rays. Consequently, a pulse-shape analyzer is required to differentiate neutrons of a given energy from gamma/X-rays. An example of a neutron detector that relies upon elastic scattering is the NE-213 liquid-scintillation detector. This detector was used by Lipson et al. [7] to measure neutron emissions from their Au/Pd/PdO:D heterostructures during exothermic deuterium desorption. To decrease the natural neutron background, the detectors were surrounded by boron-containing polyethylene, and the entire setup was placed in the underground laboratory of Hokkaido University under 10 m of heavy concrete. Because the efficiencies of these detectors to detect neutrons were on the order of 5%, Lipson et al. were able to measure 2.45 MeV neutrons at a count rate of $(19 \pm 2) \times 10^{-3} \text{ n s}^{-1}$ in a 4π solid angle. Srinivasen et al. [20] also used high recoil type plastic scintillator NE102A to monitor their Milton Roy hydrogen generators. In their experiments, the proton recoil counter tracked the BF_3 counters.

Jones et al. [23] used a neutron detector comprised of an outer ring of 16 ^3He -filled proportional counter tubes embedded in a polyethylene moderator and an inner ring of a plastic scintillating neutron detector viewed by a PMT to detect fast neutrons. A stainless steel sample chamber was placed inside the inner ring. Both gas loading and electrolytic loading of Ti foils were done. Neutron emissions were observed for the D_2 and $\text{D}_2\text{SO}_4/\text{D}_2\text{O}$ systems but not for the corresponding H_2 and $\text{H}_2\text{SO}_4/\text{H}_2\text{O}$ systems.

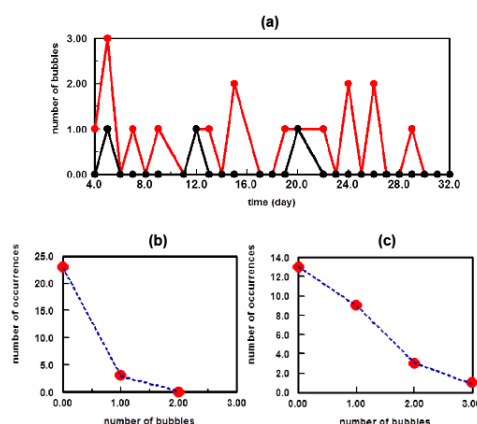


Figure 1. (a) Bubble detector results where red is for the cell and black is the background. Measurements began after the Pd was plated out. Summary of probability analysis done for (b) background (correlation = 0.99993) and (c) cell (correlation = 0.99964). Data points are indicated by (red filled circles) and calculated by (blue dotted line).

Bubble detectors are quasi-real-time neutron detectors. Tiny droplets of superheated liquid are dispersed throughout a clear moderating polymer inside the clear housing of the detector. When a thermalized neutron strikes a droplet and interacts with ${}^6\text{Li}$, the droplet immediately vaporizes, forming a visible gas bubble trapped in the gel. The number of droplets provides a direct measurement of the tissue-equivalent neutron dose. The bubbles in the detector can be compressed and the detector can be reused for up to three months. Shyam and Rout [24] used an array of bubble detectors to detect neutrons created by imploding palladium deuteride X pinches using a low energy capacitor bank. The $\text{PdD}_{0.5}$ X pinches emitted 5×10^4 neutrons per discharge. Bubble detectors were used in a Pd/D co-deposition experiment on Ni screen. The bubble detector results are summarized in Fig. 1. It can be seen that more bubbles were seen for bubble detectors near the cell than were observed for the background (Fig. 1a). Probability analysis was used to analyze the data. The results for the cell and background are summarized in Fig. 1b and c. From the analysis, the average number of neutrons per day for the cell was $69,200 \pm 6600$ and the background was $12,600 \pm 3300$. By paired *t*-test, the probability that the bubble detector results are random is one in a thousand. This indicates high statistical significance between the experiment and background. The neutron emission rate for the cell was estimated to be 0.65 n/s.

2.2. Charged particles

Ionization detectors are commonly used to detect charged particles in real time. Ionization detectors include gaseous ionization detectors and semiconductor detectors. Gaseous ionization detectors use the ionizing effect of radiation upon a gas-filled sensor. If a particle has enough energy to ionize a gas atom or molecule, the resulting electrons and ions cause a current flow which can be measured. The basic design of these detectors is two electrodes separated by air or a special fill gas. Examples of gaseous ionization detectors are ionization chambers, proportional counter, and Geiger–Müller tube. While these detectors are robust and inexpensive, they respond to gamma radiation, X-rays, beta particles, as well as charged particles. No spectral information can be generated and there is no discrimination between radiation types. An example of detectors of this type used in LENR experiments is the Femto-tech tritium gauge used by Claytor et al. [25]. In these experiments, a number of palladium alloys were loaded with either deuterium or hydrogen under low energy plasma bombardment. Tritium production was only observed when deuterium gas was

used. It was observed that most of the alloys did not produce tritium. Only the PdRhCoB, PdCu, PdRh (0.1%) and PdB alloys produced tritium under these experimental conditions.

Surface-barrier detectors are an example of semiconductor nuclear detectors used to detect charged particles in real time. These detectors consist of a piece of semiconductor (Si or Ge) that has been doped with impurity atoms to form a p–n junction. A reverse bias voltage is applied to this junction to create a depletion region near the front of the device in which there are no free charge carriers. When a charged particle enters the detector it loses its energy by the creation of electron–hole pairs in the depletion region. This is similar to ionization in gases. It is these small ionization currents that are detected and measured. To detect charged particles during electrolysis, Taniguchi et al. [26] used electrolysis cells whose bottoms were comprised of thin foil cathodes. The cathodes used were either thin Pd foils or Pd layers deposited on either stainless steel or Cu foils. The backside of these cathodes was placed on top of a conventional silicon surface barrier (SSB) detector. Count rates above background were observed for electrolysis experiments done in D₂O but not for H₂O. Taking into account energy losses, they attributed the species giving rise to the increased count rates to 3.03 MeV protons. Lipson et al. [7] used an SSB detector to detect the emission of 2.5–3.5 MeV protons during exothermic deuterium desorption of Au/Pd/PdO:D heterostructures. These heterostructures were mounted on top of a heater in a vacuum chamber. The SSB detector was positioned above the Au/Pd/PdO:D heterostructure. They also detected the emission of long-range alphas (alphas with energies between 8 and 14 MeV) during exothermic deuterium desorption of Au/Pd/PdO:D heterostructures under a 10^{−1} Pa vacuum [27]. To detect these long range alphas, they used a SSB $\Delta E - E$ counter telescope comprised of a thin ΔE -detector ($h = 20\mu\text{m}$) and thick E-detector ($E = 100\mu\text{m}$). A coincidence timing gate of 20 ns was used. The requirement of coincidence between ΔE and E detectors eliminated electromagnetic noise and enabled identification of the charged particle type.

Jones et al. [28] developed a dual plastic/glass scintillator system to detect charged particles emissions by Ti foils. This charged particle spectrometer incorporated a 76 μm thick plastic scintillator adhered onto a thicker glass scintillator which was glued onto the face of a 12.7 cm diameter PMT. In these experiments, an array of five Ti foils (total surface area 180 cm²) were loaded with deuterium in the gas phase. Afterwards, these TiD_{0.5–1.4} foils were placed on the surface of the detector. Joule heating was used to create non-equilibrium conditions. Using this

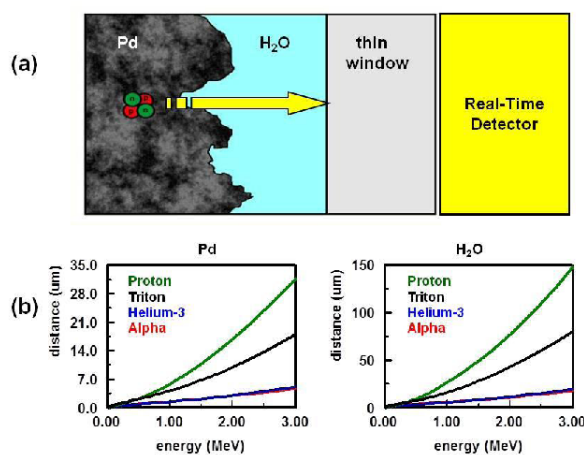


Figure 2. (a) Schematic describing the layers a charged particle has to negotiate before it reaches a real-time electronic detector. After its birth, a charged particle has to exit the metal lattice and cross a thin water layer and a thin window before it arrives at the detector. (b) LET curves calculated for charged particles traversing through palladium and water.

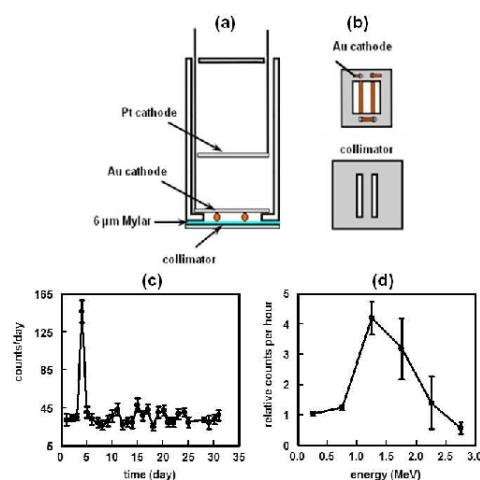


Figure 3. (a) Side view schematic of the cell used in the silicon surface barrier detector experiment. (b) Schematics of the Au-wire cathode and collimator used in the experiment. (c) Silicon barrier counts per day for the 1.0–1.5 MeV energy region. Arrow indicates when the current was turned on. (d) Relative counts per hour (day 4 count/day 3 bkg count) as a function of energy (MeV).

detector, they observed charged particle emissions in excess of 2000 counts per hour. Using an Al degrader between the $\text{TiD}_{0.5-1.4}$ foil and the plastic scintillator, they attributed those emissions to 3 MeV protons.

2.3. Problems with real-time detection methods

Many of the LENR experiments summarized in Table 1 involved electrolysis. Real-time, energetic particle detectors cannot be immersed in the cell. They have to be placed outside the cell. Since real-time detectors are positioned outside the cell, the likelihood of detection decreases by a factor of the square distance from the cathode. Consequently, these detectors have to be placed in close proximity to the cell and, in particular, the cathode. Figure 2a shows a schematic of the placement of a real-time detector next to a thin window that is in close proximity to a Pd cathode. A thin film of solution separates the cathode from the window. The emission of energetic particles from a source, i.e. cathode, occurs isotropically. The presence of the cathode, water film, and thin window will not impact neutrons. However, charged particles will experience energy losses as they traverse through the cathode, water film, and thin window to reach the detector. Linear energy transfer (LET) curves for charged particles traversing through Pd and water, Fig. 2b, were calculated using the SRIM-2003.26 code of Ziegler and Biersack [29]. These curves show that charged particles do not travel far through Pd metal and an aqueous medium.

Electronic particle detectors can be subject to low level electronic noise picked up from the local environment. For example, Jones et al. [30] retracted claims of neutron emissions from Pd/LiOD electrolytic cells when it was found that the large bursts they were seeing with their ^3He detectors were actually the result of high voltage breakdown in the electronics. The retraction was for the ^3He detector only and does not imply a retraction of highly-publicized earlier results and publications using the BYU neutron spectrometer nor the charged-particle spectrometer described above. Those results have not been retracted. Besides electronic noise, these real-time detectors are temperature sensitive. Also with real-time detectors, long acquisition times are typically used to improve the signal to noise ratio. If the rate of energetic particle production is sporadic and/or at a low level, the resultant signal can be averaged away when long acquisition times are used. Another problem with neutron detectors is multiplicity. If multiple neutrons hit the detector

Table 2. Estimated energies of charged particles emitted from the surface of the Pd cathode.

Layer	Proton (MeV)	Triton (MeV)	^3He (MeV)	Alpha (MeV)
Measured by SSB	1.1	1.1	1.1	1.1
6 μm Mylar	0.45	0.55	1.45	1.40
10 μm water	0.53	0.7	1.80	1.80
Total	2.98	2.35	4.35	4.30

at the same time, the discriminator will reject the signal.

As indicated in Table 1, CR-39 detectors used in Pd/D co-deposition experiments showed the presence of energetic charged particles and neutrons [15–18]. To illustrate some of the problems using real-time charged particle detection in electrochemical cells, a Pd/D co-deposition experiment was conducted using a silicon surface barrier detector to detect charged particles in real time. Figure 3a shows a schematic of a cell that was assembled to conduct this measurement. A circular hole was cut into the bottom of the butyrate cell. A 6 μm thick Mylar window was epoxied over the hole using aquarium RTV silicone. Figure 3b shows a schematic of the Au cathode. The Au wires making up the cathode are pressed against the Mylar window. To decrease scattering, a 100 μm thick acrylic collimator, shown in Fig. 3b, was placed on the outside of the cell. The holes cut into the collimator line up with the gold wires. This collimator only allows particles traveling perpendicular to the surface to enter the silicon barrier detector. Once assembled the cell was filled with electrolyte and placed on top of a silicon barrier detector.

Results of the experiments are summarized in Figs. 3c and d. A plot of counts per day for the energy region 1.0–1.5 MeV is shown in Fig. 3c. The arrow indicates when the current was applied to the cell. An increase in the number of counts was observed which immediately dropped down by the next day. This decrease is not surprising. As Pd plates out, the increasing Pd deposit will impede charged particles from reaching the silicon barrier detector. There is also the effect of the Mylar window on the number of observed charged particles. Linear energy transfer (LET) curves indicate that the 6 μm thick Mylar window will cut off <0.45 MeV protons, <0.55 MeV tritons, <1.40 MeV ^3He , and <1.45 MeV alphas. Figure 3d is a plot of the count rate on the fourth day divided by the count rate on the third day vs. energy. It is an attempt to characterize the energy of the charged particles observed for the first day of electrolysis. The plot shows that the majority of the charged particles that reached the detector have energies between 1.0 and 2.0 MeV with a peak maximum at 1.1 MeV. To estimate the energy of the energetic charged particles at their birth, it is assumed that they were born near the surface of the Pd and that they transverse through a 10 μm thick water film and a 6 μm thick Mylar film. LET curves were used to determine the energy losses through the water and the Mylar film. The results of these calculations are summarized in Table 2. Because of the experimental configuration used, it was not possible to ascertain the identity of the charged particles.

3. Advantages and Disadvantages of SSNTD

CR-39 is not a relatively new detector material. As indicated *vide supra*, Cartwright et al [1] were the first to demonstrate that CR-39 could be used to detect nuclear particles in 1978. Since then hundreds of papers in the literature describe the use and development of CR-39 for charged particle detection and neutron dosimetry. Countries involved in this research include Italy [31], Egypt [32,33], India [34], Japan [35], Hungary [36], as well as the United States [1,37]. Landauer uses CR-39 in their Neutrak dosimeter for neutron detection [38]. City University of Hong Kong has a Trackology Research Group headed by Nikezic and Yu [39].

Recently, Durrani [40] wrote a review article discussing the advantages and disadvantages of SSNTDs in detecting energetic particles. Table 3 lists these advantages and disadvantages of SSNTDs as identified by Durrani. SSNTDs do not require a power source nor do they require shielding. They do not generate false signals due to either electronic noise or temperature changes. They are not affected by electromagnetic pulses (EMPs), which is why these detectors

Table 3. Strengths and Weaknesses of SSNTDs [29].

Strengths	Weaknesses
Inexpensive Ruggedness and simplicity	Lack of real-time capability Poor charge and energy discrimination—track size/shape depends upon the charge and mass of the particles as well as the angle of incidence. There is significant overlap in the size distributions of the tracks due to energetic particles
Integrating capability Responds to both charged particles and neutrons Small geometry—trails of damage are nm/ μ m in diameter and length	Variability in SSNTDs—environmental conditions and manufacturing procedures results in problems of precision and reproducibility
Long history and selectivity of track recording—SSNTDs can retain a record of activity for billions of years Existence of thresholds for registration—SSNTDs can register particles only if their charge and LET value are above a threshold	Lack of theoretical understanding—no theoretical work explains how certain properties of materials can predicate or ascertain a viable ability for track formation/retention

are used in the ICF field [3].

It has been shown that the background of CR-39 detectors varies from batch to batch, from foil to foil in the same batch, from one side to another of the same foil and within the same foil surface [41]. Prolonged etching of CR-39 detectors showed that the background track density remains constant once they are fully etched. This indicates that the background is basically due to surface defects. It was also found that the manner in which CR-39 detectors were stored influences the magnitude of the background [42]. When unetched CR-39 detectors were exposed to a neutron source, it was shown that storage at higher temperatures (up to 37°C) resulted in partial or complete removal of tracks [43]. The annealing of damage trails occurs due to diffusion of atomic defects through the crystal lattice or movement of molecular fragments within the polymer. This indicates that, until they are etched, self healing of the detectors will occur with time and that the number of background tracks in the detectors will reach a steady state.

Besides background, there is variability in the response of CR-39 detectors from different vendors to energetic particles. Figure 4a shows the response of CR-39 detectors from TASL [44], Landauer [8], and Fukuvi [8] to different energies of alpha particles. The etching conditions were very similar. It can be seen that the response of Landauer and Fukuvi CR-39 to alpha particles is very similar. However, the alpha tracks obtained using TASL CR-39 are 43% larger than the alpha tracks obtained on either Landauer or Fukuvi CR-39. This is due to the fact that both Landauer and Fukuvi CR-39 have more cross-linking than TASL CR-39. As a result both Landauer and Fukuvi CR-39 are harder than TASL CR-39. The response of Landauer and Fukuvi CR-39 to protons is shown in Fig. 4b. The response to protons overlaps for proton energies greater than 2 MeV but diverges for lower proton energies.

For the electrolysis experiments summarized in Table 1 [10–19], Fukuvi CR-39 was used. Fukuvi brand CR-39 is resistant to chemical damage. This was not true of TASL CR-39. Experiments were conducted using TASL CR-39. An experiment was done in which a Ni screen was placed in contact with a bare TASL CR-39 detector. Electrolysis was then done in a LiCl–H₂O solution for two weeks. Figure 5a shows a photograph of the unetched detector at the end of this experiment. The detector has a frosty appearance except for where the Ni screen was in close contact with it. When this same experiment was done using Fukuvi CR-39, no fogging of the unetched detector was observed. A Pd/D co-deposition experiment was then done on Ag wire in contact with a TASL CR-39 detector. The standard plating/charging protocol was followed [45]. The CR-39 detector was only etched for 2 h. Visual inspection of the

etched detector showed that it had a fogged appearance except for where the cathode had been in close contact with the CR-39. Figure 5b shows a photomicrograph taken at $500\times$ magnification of a cloudy area that was away from the cathode. In the cloudy area, bright, shallow, irregularly shaped features are observed that show no contrast. These features are due to chemical damage of the detector. In the area that had been in contact with the cathode, circular objects are observed that strongly resemble tracks, Fig. 5c. These circular objects are dark on the surface but show bright spots inside when the microscope optics are focused inside the objects. These observations are diagnostic of nuclear generated tracks. A photomicrograph of the interface, Figure 5d, shows the transition from the cloudy area that has been damaged by electrolysis to the area under the cathode. The area damaged by electrolysis shows irregularly shaped features which are distinctly different from the circular shapes observed under the cathode. These experiments demonstrate that not all brands of CR-39 can be used in LENR experiments. The formulation used to fabricate TASL CR-39 detectors makes the detector more sensitive to the detection of energetic particles. However, it also makes TASL detectors more susceptible to chemical damage when used in electrolysis experiments.

One of the most significant advantages of CR-39 for LENR experiments is its integrating capability. Typically emissions occur sporadically or at low fluxes in LENR experiments. For example, Lipson et al. [7], using a NE-213 detector to detect neutrons and a CR-39 detector to detect protons, reported count rates of $(19 \pm 2) \times 10^{-3} \text{ n s}^{-1}$ and $(4 \pm 1) \times 10^{-3} \text{ p s}^{-1}$ in 4π solid angle for their Au/Pd/PdO:H heterostructures. For a CR-39 detector used in a Pd/D co-deposition experiment, Lipson et al. [19] reported count rates of $(0.6 \pm 0.1) \text{ n s}^{-1}$ in 2π solid angle. It would be very difficult to measure such low count rates using real-time detectors. As discussed *vide supra*, one problem has to do with the solid angle of detection. These issues are eliminated when using a SSNTD. In many of the experiments summarized in Table 1 [10–12, 15–19], the CR-39 detectors were placed in direct contact with the cathode thereby nearly eliminating solid angle detection issues. Because CR-39 is a constantly integrating detector, events are permanently stamped in the plastic. While it will not be known when the events occurred, the signal will not be averaged away and the number of events recorded in the plastic becomes statistically significant. Given the low flux rates and sporadic nature of the emissions, real-time detection can be sacrificed in LENR experiments.

4. Speciation of Energetic Particles Using SSNTD

Another advantage of CR-39 is its ability to speciate energetic particles and neutrons. When a charged particle passes through the plastic, it leaves a trail of damage along its track in the form of broken molecular chains and free radicals. The amount of local damage along the track is related to the local rate at which energy is lost by the particle, dE/dx where x is the distance along the track [46]. Generally, given the bulk etch rate, the first $6 \mu\text{m}$ of the surface of the CR-

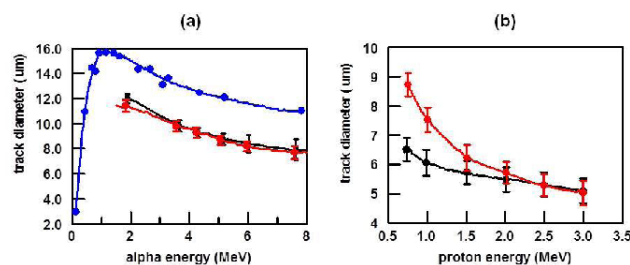


Figure 4. CR-39 calibration curves obtained for (a) alpha particles and (b) protons using TASL (blue), Fukuvi (black) and Landauer (red) CR-39 [8,44]. Fukuvi and Landauer CR-39 detectors were etched in 6 N NaOH solution at 70°C for 7 h. The TASL detector was etched in 7.25 N NaOH solution at 70°C for 7 h.

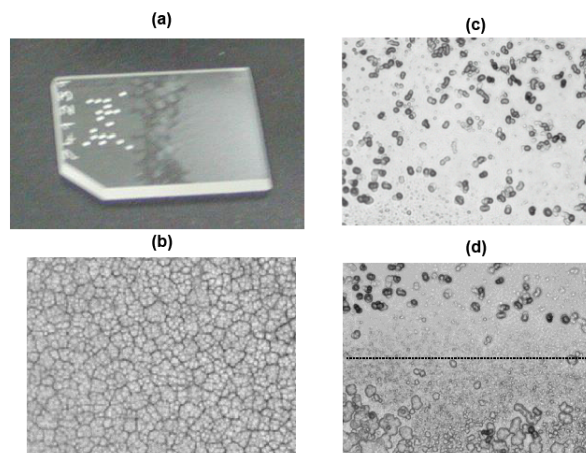


Figure 5. (a) Photograph of a TASL CR-39 detector used in a Ni/H₂O electrolysis experiment. (b–d) Photomicrographs taken at 500X magnification of a TASL CR-39 detector used in a Pd/D co-deposition experiment done on a Ag cathode where (b) was taken in a cloudy area that was not in contact with the cathode, (c) was taken in the area directly under the Ag/Pd cathode, and (d) was taken at the interface (the area above the dotted line was directly underneath the cathode while the area below the dotted line was outside of the cathode).

39 is removed. Any particle, whose LET would stop it within that distance, would not produce a track. This includes particles arriving at oblique angles to the surface. As the particle traverses the CR-39, losing energy, an energetic particle will lose energy along a path dictated by the sine of the entrance angle. Consequently, there is a limit on how oblique the resulting track will be due to LET losses upon entering the CR-39. Furthermore, the track obliqueness provides a means to differentiate between primary charged particles and secondary neutron-induced charged particles. Neutrons interact by either elastic scattering or inelastic interactions with the individual atoms comprising the CR-39. Although these reactions favor forward scattering they are nearly isotropic, resulting in secondary charged particle production over a wide range of angles. Secondary neutron spallation and scattering produces more oblique tracks than primary charged particle.

It turns out that dE/dx is different for different particle types. It is also different for particles of a given type that

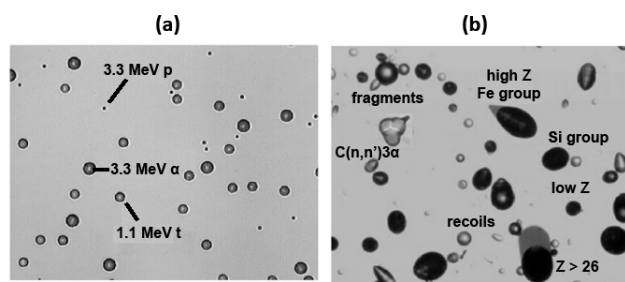


Figure 6. (a) Photomicrograph of CR-39 that was used in an ICF implosion experiment [46]. The detector had been etched for 6 h in 6 M NaOH at 80°C. Republished with permission from the America Institute of Physics. (b) Photomicrograph of a CR-39 detector exposed in the ISS [4]. The detector had been etched for 20 h in 6 M NaOH at 70°C. Republished with permission from Oxford University Press.

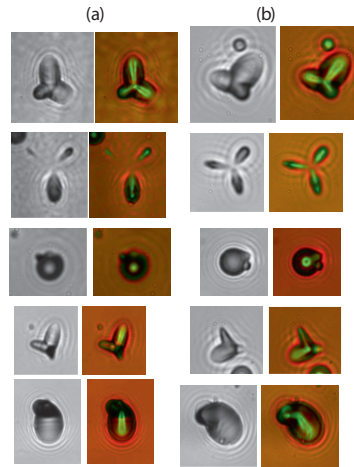


Figure 7. Symmetric triple tracks observed in CR-39 detectors where (a) were generated in Pd/D co-deposition experiments and (b) were generated upon exposure to DT generated neutrons. In both (a) and (b) the left-hand image was obtained with the microscope optics focused on the surface of the CR-39 detector while the right-hand image is an overlay of two photomicrographs taken at different focusing depths (surface of the detector and the bottom of the pits).

have different energies. The diameter of the etched pit provides a measure of dE/dx for the particle. Consequently, diameters can often be used to identify the particle type if the energy is known. Calibration curves, such as those shown in Fig. 4, are used for this purpose. Figure 6a [46] shows tracks obtained as a result of an ICF implosion using D^3He fuel in a thin glass shell. Tracks due to 3.3 MeV protons, 3.3 MeV alphas, and 1.1 MeV tritons are identified. It can be seen that each particle type can be distinguished based on track size. Figure 6b shows tracks obtained on a CR-39 detector inside the International Space Station (ISS) [4]. This detector was part of a stack comprised of three CR-39 sheets. The first and second sheets were separated with 50 μm thick Ti foil. The second and third sheets sandwiched 350 μm Lexan. The stack was wrapped in 30 μm thick Al foil and sealed hermetically in a 40 μm thick polyethylene bag. After etching, the detector shows tracks due to neutron elastic scattering on H, recoil of C and O

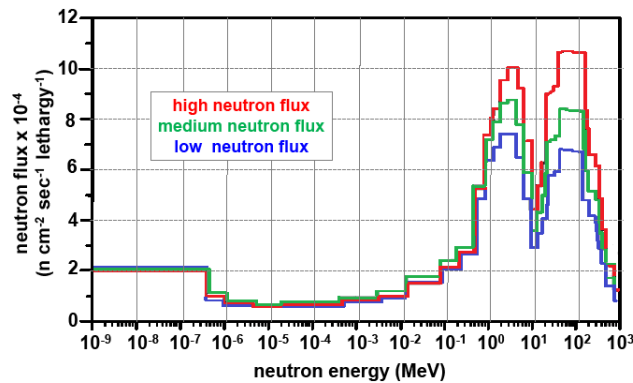


Figure 8. Comparison of neutron energy spectra on three different days as measured by the Bonner ball [48].

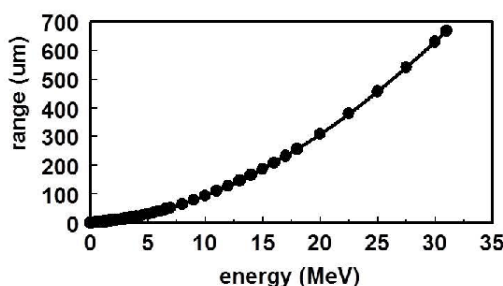


Figure 9. LET curve calculated for alpha particles traversing through CR-39.

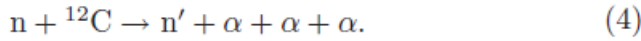
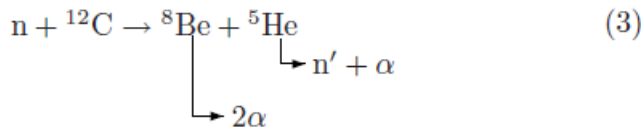
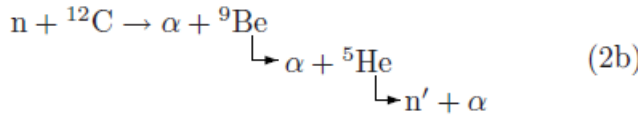
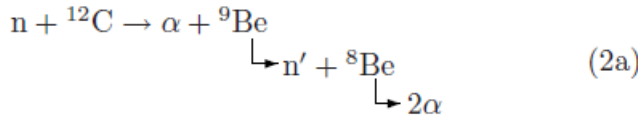
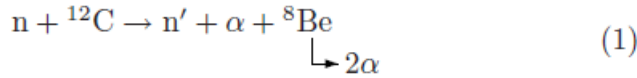
atoms, fragmentation, and neutron-induced charged particle reactions including fission. A triple track is seen that is due to the $C(n,3\alpha)n'$ reaction. Additional methods to speciate the charged particle emissions are discussed below.

4.1. Triple tracks

The most easily identified neutron interaction in CR-39 is the carbon break-up reaction. If the energy of a neutron is greater than 9.6 MeV, the inelastic neutron interaction can cause the carbon atom to shatter into three alpha particles. The residuals of the reaction can be viewed in the CR-39 detector as a three-pronged star, or triple track, where each prong represents each charged particle that occurs in the decay. The presence of these triple tracks is diagnostic of >9.6 MeV neutrons.

Roussetski [8] was the first to report seeing triple tracks in his CR-39 detectors that had been placed in contact with Au/Pd/PdO and PdO/Pd/PdO heterostructures that had been loaded electrochemically with D. Once in contact with CR-39, the sample was heated to 50°C to stimulate the desorption of deuterium. The electrolytic loading and thermo-stimulation steps were repeated several times.

Mosier-Boss et al. [17,18] reported seeing triple tracks in CR-39 detectors used in Pd/D co-deposition experiments. Figure 7 shows representative Pd/D co-deposition generated triple tracks as well as their corresponding DT neutron generated triple tracks. Focusing deeper inside the triple tracks, it can be seen that there are three alpha particle generated tracks breaking away from a center point. These features are diagnostic of the carbon breakup reaction. Comparing both sets of triple tracks, it can be seen that the Pd/D co-deposition triple tracks are indistinguishable from the DT neutron generated tracks. The examples of Pd/D and DT neutron tracks do not have the exact same shape. The $n + {}^{12}\text{C}$ reaction can proceed to the four-body final state through one or more of the following reaction mechanisms [47]:



Processes (1)–(3) are sequential decays going through different excited states of intermediate systems and process (4) is a simultaneous four-body break-up. The observed relative sizes and shapes of the lobes making up the triple tracks in Fig. 7 are the result of these different processes.

No triple tracks have been observed in either control experiments using either CuCl_2 or NiCl_2 in place of the PdCl_2 . Nor have they been observed in blank detectors. This indicates that the triple tracks observed in Pd/D co-deposition experiments are not due to cosmic ray spallation neutrons. This is further supported by the cosmic-ray neutron spectrum measured by Nakamura et al. [48], Fig. 8. These spectra were obtained using three neutron detectors, a ${}^3\text{He}$ -loaded multi-moderator detector (Bonner ball), a NE213 organic scintillator, and a high sensitivity rem (dose equivalent) counter. As can be seen in Fig. 8, the energy spectrum of cosmic-ray-induced spallation neutrons consists of three peaks: thermal, 2 MeV evaporation, and a cascade peak at 100 MeV. The thermal and 2 MeV evaporation neutrons will not cause a carbon atom to shatter as the threshold energy for a neutron to cause a carbon atom to shatter is 9.6 MeV. The 100 MeV cascade neutrons will cause a carbon atom to shatter. Energy in the carbon shattering reaction is conserved, where:

$$E_n = E_{\text{th}} + E_{\alpha 1} + E_{\alpha 2} + E_{\alpha 3} + E_{n'}, \quad (5)$$

where E_n is the energy of the incoming neutron; E_{th} is the threshold energy required to shatter the carbon atom (9.6 MeV); $E_{\alpha 1}$, $E_{\alpha 2}$, and $E_{\alpha 3}$ are the energies of the alpha particles formed when the carbon atom shatters; and $E_{n'}$ is the energy of the outgoing neutron. If $E_{n'} = 0$ MeV, each alpha particle will have an energy of 30.1 MeV. The LET curve for alpha particles in CR-39, Fig. 9, is used to determine how far these particles will travel through the CR-39 detector. According to the LET curve, 30.1 MeV alphas will travel 635 μm in CR-39. Should a 100 MeV neutron cause a carbon atom to shatter, there will not be a discernible triple track because of the long lengths traveled by the alphas. The residuals of the reaction with a 100 MeV neutron will look like three solitary alpha tracks.

As shown in Fig. 8, the 12–17 MeV neutron energies, which overlaps the energy of DT fusion neutrons, occur an order of magnitude less frequently than either evaporation or cascade neutrons. The total measured background spallation neutron flux was $7.5 \times 10^{-3} \text{ n cm}^{-2} \text{ s}^{-1}$, with $< 10^{-4} \text{ n cm}^{-2} \text{ s}^{-1}$ in the DT fusion neutron energy range.

This low neutron flux, coupled with the CR-39 relative neutron detection inefficiency, $< 10^{-6}$ for triple tracks [37], accounts for the complete absence of triple tracks in the background.

4.2. Fission tracks

Figure 6b shows tracks due to high-Z fission fragments. These are examples of fission tracks. As can be seen, the tracks due to these high-Z fission fragments are significantly larger than the tracks due to smaller tritons, protons, and alpha particles. The large size of these tracks make them easily identifiable.

Pd/D co-deposition experiments were conducted using uranium as a witness material to determine the energies of the neutrons emitted during the co-deposition process. ^{235}U is fissioned by thermal and higher energy neutrons while ^{238}U is fissioned by >2 MeV neutrons. The cross section for interaction with fast neutrons is equivalent for ^{235}U and ^{238}U , on the order of < 2 barns (as compared to >500 barns for the thermal fission of ^{235}U).

To demonstrate that native uranium isotopes can be fissioned by neutrons, a uranium wire was placed in contact with a CR-39 detector and was exposed to DT neutrons. Afterwards the detector was etched for 1 h. Figure 10a shows a photomicrograph of the etched detector. The arrow indicates a long cylindrical track amongst the oval/circular shaped alpha/neutron recoil tracks. This long cylindrical track is a fission track.

In the Pd/D co-deposition experiment, a $250\text{ }\mu\text{m}$ diameter Au wire was wrapped around a 1 cm length of uranium wire. This composite cathode was placed in contact with a CR-39 detector and Pd/D were electrochemically deposited onto this composite cathode. Figure 10b shows a photomicrograph of tracks observed in the CR-39 detector used in this experiment. Circular and oval alpha tracks due to the decay of uranium and its daughters are observed. Among these alpha tracks, large cylindrical tracks, like the one indicated by an arrow in Fig. 10b, were observed. As shown by the bright streak in the overlay image, this track is shallow. The large track is approximately $40\text{ }\mu\text{m}$ long and $10\text{ }\mu\text{m}$ wide. It is about five times larger than the surrounding alpha tracks and resembles the high-Z tracks shown in Fig. 6b and the DT neutron induced uranium fission track shown in Fig. 10a. Such large tracks have not been observed in CR-39 detectors exposed to uranium wire that had not been subjected to Pd/D co-deposition.

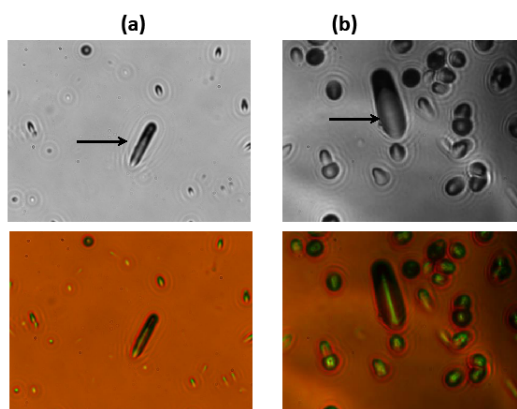


Figure 10. (a) Photomicrographs of a CR-39 detector that had been in contact with uranium wire exposed to DT neutrons. Magnification is $1000\times$. The detector had been etched for 1 h in 6 M NaOH at 60°C . (b) Photomicrographs of a CR-39 detector that had been used in a Pd/D co-deposition experiment conducted on an Au/U cathode. Magnification is $1000\times$. The detector had been etched for 6 h in 6 M NaOH at 60°C . The images on the top were obtained with the optics focused on the surface of the detector. The bottom images are an overlay of two images taken at different focusing depths (surface and the bottom of the tracks). Arrows indicate a large elongated track among the uranium alpha tracks.

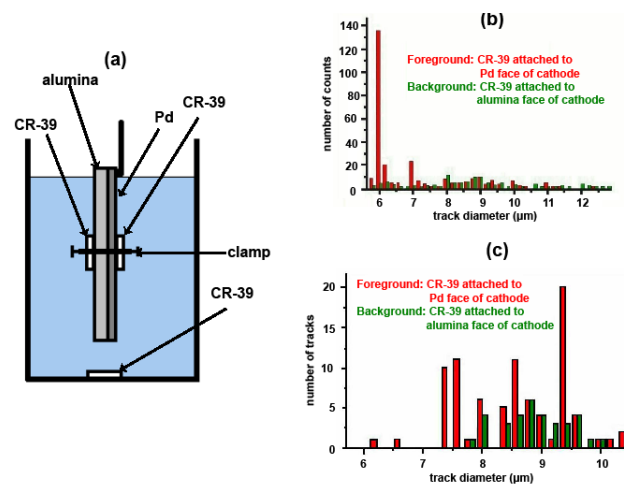


Figure 11. (a) Schematic of the placement of CR-39 detectors used in electrolysis experiments. (b) Number of charged particles vs. track diameter for CR-39 detectors in contact with the thin Pd film cathode and the alumina substrate during electrolysis. (c) Number of charged particles vs. track diameter for CR-39 detectors, shielded with 25 μm Cu film, in contact with the thin Pd film cathode and the alumina substrate during electrolysis.

4.3. The use of shielding films for particle identification

Lipson et al. [11,12,14,49], Karabut et al. [9], and Roussetski et al. [13] have used various foils (11–66 μm thick Al, 25–50 μm thick Cu, and 60 μm thick polyethylene) between the H/D absorbing metal and the CR-39. These shielding foils have known stopping ranges which are used to identify the charged particles.

Figure 11a is a schematic showing the placement of open and shielded CR-39 detectors used in electrolysis experiments [49]. The results using bare and Cu shielded CR-39 detectors are summarized in Fig. 11b and c, respectively. Comparison of track diameters obtained with open and shielded CR-39 allows the identification of charged particles by using the stopping range of the shielding material. A 25 μm Cu film completely absorbs all alpha particles and protons with energies below 9.0 and 2.3 MeV, respectively. For foreground runs (t 2–30 days) with electrolysis of Pd thin film cathodes, the open CR-39 detectors show the appearance of tracks not found in the background detectors in the same electrolysis run. As shown in Fig. 11b, two significant peaks at 6.0 and 7.0 μm are observed. For shielded CR-39 detectors (25 μm Cu film) using the same cathode, the 6 μm peak of the open CR-39 disappears due to the Cu shielding, Fig. 11c. The disappearance of the 6.0 μm peak in the Cu shielded detector indicates that this peak is due to low MeV protons. From calibration data, the proton energy was estimated to be 1.5–1.7 MeV. The 7.0 μm peak in the open CR-39, Fig. 11b, shifts to larger track diameters and splits into three narrow peaks, Fig. 11c. Due to its shift and splitting after crossing the Cu shield, the 7.0 μm peak in Fig. 11b is attributed to α -particles with energies between 11.0 and 16.0 MeV.

4.4. Successive (or sequential) etching for particle identification

Lipson and Roussetski [19] developed a successive etching technique to identify the charged particles and their energies responsible for the tracks in CR-39 detectors. This successive etching method has been used by other groups working with radioactive materials to identify and determine the energies of emitted charged particles [50–53]. In this approach, calibration curves were generated by exposing CR-39 detectors to alpha particles and protons of known energies. Lipson et al. exposed CR-39 detectors to alpha sources with energies in the range of 1.6–7.7 MeV and to monoenergetic

cyclotron alpha-beams in the energy range of 10–30 MeV. Detectors were also calibrated with Van de Graff accelerator producing monoenergetic proton beams with energy ranges of 0.75–3 MeV. Only circular tracks are used to generate calibration curves. These tracks are created by charged particles with trajectories normal to the surface of the detector. There is an inverse relationship between the charged particle energy and the track diameter. The smaller the diameter, the higher the energy. There is also a cutoff in energy that will result in a track. Figure 12a and b show alpha and proton calibration curves, respectively, after 7, 14, 21, and 28 h of etching. As can be seen from these calibration curves, alpha particles with energies less than 6 MeV and protons with energies less than 1 MeV can be identified after a 7 h etch time. However, longer etching times are required to unambiguously identify alphas and protons energies greater than 6 MeV and 1 MeV, respectively.

SRI conducted several Pd/D co-deposition experiments that used CR-39 detectors. The experiments were conducted in the presence of a magnetic field. Two experiments were done with the detector inside the cell. In these experiments a 60 μm thick polyethylene film separated the Ag cathode from the detector. These detectors, identified

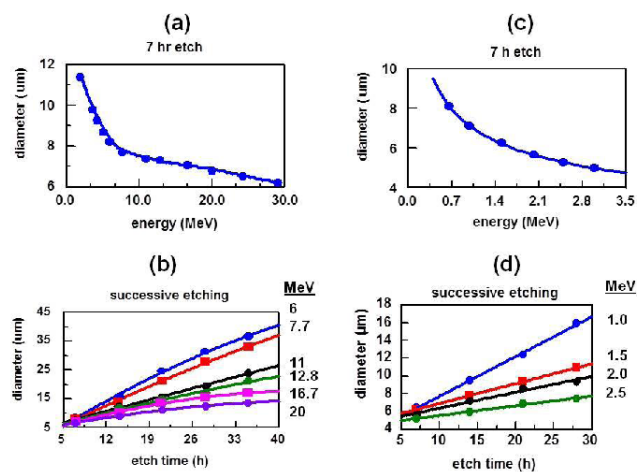


Figure 12. Calibration curves generated for energetic alpha and proton particles. (a) Alpha track size as a function of energy (7 h etch). (b) Track diameter vs. etching time for six different alpha energies. Alpha particle energies are indicated. (c) Proton track size as a function of energy (7 h etch). (d) Track diameter vs. etching time for four different proton energies. Proton energies are indicated.

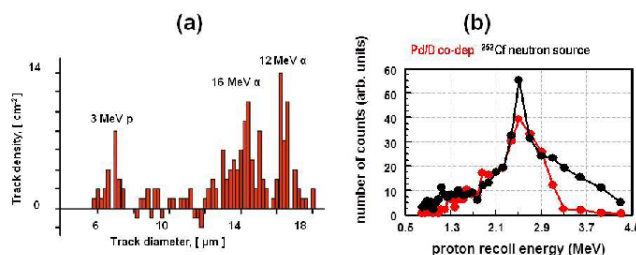


Figure 13. Results obtained for the sequential etching. (a) The front side spectrum of nuclear tracks in detector 10-5 after subtracting the neutron induced proton recoil spectrum from its back side (etch time is 21 h). (b) Reconstruction of the proton recoil spectra for detector 10-7 and a detector exposed to ²⁵²Cf neutrons (etch time 14 h).

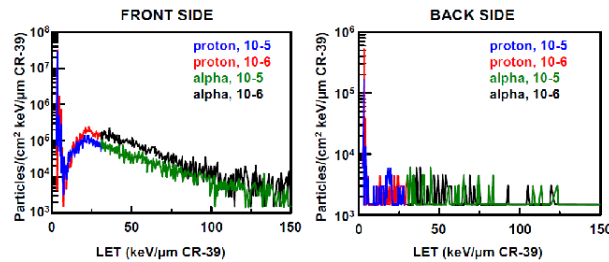


Figure 14. LET spectra of differential fluence calculated for the front and back surfaces of detectors 10-5 and 10-6. The front surface was the side closest to the cathode.

as 10-5 and 10-6, underwent successive etching analysis by Lipson and Roussetski. Using this process, they identified 3 MeV protons, 16 MeV alphas, and 12 MeV alphas in the CR-39 detectors used in heavy water experiments, Fig. 13a. No tracks above background were observed in the light water experiments. In another SRI experiment, the CR-39 detector was placed outside the cell. A 6 μm thick Mylar film was placed between the detector and the Ag cathode. The detector used in this experiment also underwent successive etching analysis by Lipson and Roussetski. In their analysis, they identified proton recoil tracks due to 2.45 MeV (DD) neutrons, Fig. 13b.

4.5. LET spectrum analysis for particle identification

The CR-39 detectors used in the SRI immersion experiments, detectors 10-5 and 10-6, were scanned using an automated scanning track analysis system to obtain quantitative information on the pits produced in the CR-39. The scanner has a high quality microscope optical system operating at a magnification high enough to discriminate between tracks and background. The images obtained were analyzed by the proprietary software that made 15 characteristic measurements of each feature located in the image. These measurements were used to reliably discriminate between etched tracks and background features present on and in the plastic detector.

Zhou, of NASA-Johnson Space Center, took the scanned data of detectors 10-5 and 10-6 and analyzed them using a LET spectrum method [54–59]. In this analysis, Zhou used the scanned values of the major and minor axes of the tracks to differentiate the charged particle species and energy. Applying the LET spectrum method, differential/integral fluence, Fig. 14, and the energy distributions of the charged particles, Fig. 15, were determined. For protons, a the major peak is observed at 11.5 – 12 MeV for the front CR-39 surfaces and 9.75 MeV for the back CR-39 surfaces.

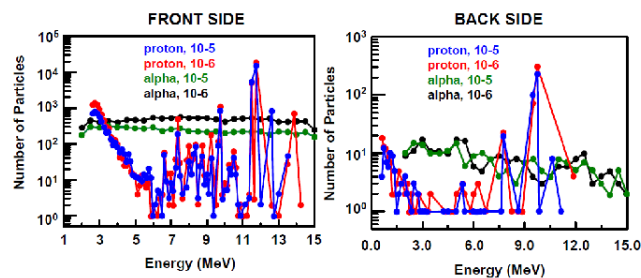


Figure 15. Energy distribution of particles calculated for the front and back surfaces of detectors 10-5 and 10-6. The front surface was the side closest to the cathode.

The distribution of a particles is nearly uniform because they are mainly secondary particles.

5. Conclusions

Compared to electronic, real-time detectors, solid state nuclear track detectors, such as CR-39, are ideal for use in LENR experiments. The advantages of CR-39 over real-time, electronic detectors are:

- (1) CR-39 detectors do not require power and can be placed in close proximity to the cathode. This eliminates the solid angle detection losses.
- (2) CR-39 detectors can be used in both electrolysis and gas loading experiments.
- (3) CR-39 detectors are not affected by low level electronic noise from the local environment and do not require shielding. Nor do they respond to temperature changes.
- (4) CR-39 is an example of a constantly integrating detector. When an event occurs it is permanently stamped in the plastic. Nothing gets averaged away. This is important for reactions that occur sporadically in bursts or at low flux levels, which is often true of LENR experiments.
- (5) The size and shape of the tracks in CR-39 detectors can be used to identify the energetic particles that caused them.
- (6) CR-39 detectors are robust and inexpensive.
- (7) CR-39 detectors retain their record of nuclear activity for decades and can be repeatedly re-examined.
- (8) Real-time electronic detectors require expensive and complicated electronic modules that are required for both timing and background discrimination, even if shielding is present. Unlike CR-39, electronic, real-time detectors tend to discriminate against multiple simultaneous events. This results in an undercounting of the nuclear products.

Given all these advantages over electronic, real-time detectors, solid state nuclear track detectors, such as CR-39, are the detector of choice in LENR experiments.

Acknowledgements

This work was funded by the Defense Threat Reduction Agency (DTRA), and JWK Corporation. The authors would like to thank Dr. Gary Phillips, nuclear physicist, retired from the Naval Research Laboratory, US Navy, Radiation Effects Branch for valuable discussions on CR-39. They would also like to thank Dr. Roger Boss for doing the probability analysis of the bubble detectors. The authors would also like to thank Mr. Mark Morey, Dr. Jim Tinsley, and Mr. Paul Hurley of National Security Technologies, LLC, Special Technologies Laboratory in Santa Barbara, CA for exposing CR-39 detectors to DT neutrons. Finally, the authors would like to thank Dr. Frank Gordon, retired Head of Research and Applied Sciences Dept. SSC-Pacific, for all the support he had provided in this field of research.

References

- [1] B.G. Cartwright, E.K. Shirk and P.B. Price, A nuclear-track recording polymer of unique sensitivity and resolution, *Nucl. Instrum. Meth.* **153** (1978) 457–460.
- [2] D. Nikezic and K.N. Yu, Formation and growth of tracks in nuclear track materials, *Mater. Sci. Eng. R* **46** (2004) 51–123.
- [3] J.A. Frenje, C.K. Li, F.H. Séguin, D.G. Hicks, S. Kurebayashi, R. D. Petrasso, S. Roberts, V. Yu. Glebov, D.D. Meyerhofer, T.C. Sangster, J.M. Soures, C. Stoeckl, C. Chiritescu, G.J. Schmid and R.A. Lerche, Absolute measurements of neutron yields from DD and DT implosions at the OMEGA laser facility using CR-39 track detectors, *Rev. Sci. Instrum.* **73** (2002) 2597–2606.

- [4] J.K. Pálfalvi, Y. Akatov, J. Szabó, L. Sajó-Bohus and I. Eördögh, Evaluation of solid state nuclear track detector stacks exposed on the international space station, *Radiat. Prot. Dosimetry* **110** (2004) 393–397.
- [5] X.-Z. Li, D.-W. Mo, L. Zhang, S.-C. Wang, T.-S. Kang, S.J. Liu and J. Wang, Anomalous nuclear phenomena and solid state track detector, *Nucl. Tracks and Rad. Meas.* **22** (1993) 599–604.
- [6] S. Jin, F. Zhan and Y. Liu, Deuterium absorbability and anomalous nuclear effect of YBCO high temperature superconductor, *Proc. Fourth Int. Conf. on Cold Fusion*, Vol. 3, Nuclear Measurements Papers, Lahaina, Maui, Hawaii, Dec. 6–9, 1993, T.O. Passell (Ed.), Electric Power Research Institute, Palo Alto, CA, 1994, pp. 4.1–4.3.
- [7] A. Lipson, F. Lyakhov, A. Roussetski, T. Akimoto, N. Asami, R. Shimada, S. Miyashita and A. Takahashi, Evidence for low-intensity D–D reaction as a result of exothermic deuterium desorption from Au/Pd/PdO:D heterostructure, *Fusion Sci. Technol.* **38** (2000) 238–252.
- [8] A.S. Roussetski, Application of CR-39 plastic track detector for detection of DD and DT-reaction products in cold fusion experiments, *Proc. 8th Int. Conf. on Cold Fusion*, May 21–26, 2000, Lerici (La Spezia), Italy, Italian Physical Society, Bologna, Italy.
- [9] A.G. Lipson, A.B. Karabut and A.S. Roussetsky, Anomalous enhancement of DD-reaction, alpha emission and X-ray generation in the high current pulsing deuterium glow-discharge with Ti-cathode at the voltages ranging from 0.8 to 2.5 kV, *Proc. 9th Int. Conf. on Cold Fusion*, 2002, Beijing, China.
- [10] R.A. Oriani and F.C. Fisher, Generation of nuclear tracks during electrolysis, *Jpn. J. Appl. Phys.* **41** (2002) 6180–6182.
- [11] A.G. Lipson, A.S. Roussetski, G.H. Miley and C.H. Castano, In-situ charged particles and X-ray detection in Pd thin film cathodes during electrolysis in Li₂SO₄/H₂O, in *Condensed Matter Nuclear Science: Proceedings of the 9th International Conference on Cold Fusion*, Beijing, China, May 19–24, 2002; X.Z. Li (Ed.), Tsinghua Univ. Press, Beijing, 2002, pp. 218–223.
- [12] A.G. Lipson, A.S. Roussetski, G.H. Miley and E.I. Saunin, Phenomenon of an energetic charged particle emission from hydrogen/deuterium loaded metals, In *Condensed Matter Nuclear Science: Proceedings of the 10th International Conference on Cold Fusion*, Cambridge, MA, Aug. 24–29, 2003, P.L. Hagelstein and S.R. Chubb (Eds.), World Scientific, Singapore, 2006, pp. 539–558.
- [13] A.S. Roussetski, A.G. Lipson and V.P. Andeanov, Nuclear emissions from titanium hydride/deuteride induced by powerful picoseconds laser beam, In *Condensed Matter Nuclear Science: Proceedings of the 10th International Conference on Cold Fusion*, Cambridge, MA, Aug. 24–29, 2003, P.L. Hagelstein and S.R. Chubb (Eds.), World Scientific, Singapore, 2006, 559–566.
- [14] A. Lipson, I. Chernov, A. Roussetski, Y. Cherdantsev, A. Tsivadze, B. Lyakhov, E. Saunin and M. Melich, Hot deuteron generation and charged particle emissions on excitation of deuterium subsystem in metal deuterides, *Low-Energy Nuclear Reactions Sourcebook Volume 2*, J. Marwan and S. Krivit (Eds.), American Chemical Society, Washington, DC, 2009, 95–117.
- [15] P.A. Mosier-Boss, S. Szpak, F. Gordon and L. Forsley, Use of CR-39 in Pd/D Co-deposition experiments, *Eur. Phys. J. Appl. Phys.* **40** (2007) 293–303.
- [16] P.A. Mosier-Boss, S. Szpak, F. Gordon and L. Forsley, Characterization of tracks in CR-39 detectors obtained as a result of Pd/D Co-deposition, *Eur. Phys. J. Appl. Phys.* **46** (2009) 309001 1–12.
- [17] P.A. Mosier-Boss, S. Szpak, F. Gordon and L. Forsley, Triple tracks in CR-39 as the result of Pd–D Co-deposition: evidence of energetic neutrons, *Naturwissenschaften* **96** (2009) 135–142.
- [18] P.A. Mosier-Boss, J.Y. Dea, L.P.G. Forsley, M.S. Morey, J.R. Tinsley, J.P. Hurley and F.E. Gordon, Comparison of Pd/D co-deposition and DT neutron generated triple tracks observed in CR-39 detectors, *Eur. Phys. J. Appl. Phys.* **51** (2010) 20901–1–10.
- [19] A.G. Lipson, A.S. Roussetski, E.I. Saunin, F. Tanzella, B. Earle and M. McKubre, Analysis of the CR-39 detectors from SRI’s SPAWAR/Galileo type electrolysis experiments # 7 and # 5. Signature of possible neutron emission, *Proceedings of 8th International Workshop on Anomalies in Hydrogen/Deuterium Loaded Metals*, J. Rothwell and P. Mobberley (Eds), International Society for Condensed Matter Nuclear Science, 2008, 182–203.
- [20] P.K. Iyengar and M. Srinivasan, *BARC Studies In Cold Fusion*, BARC-1500. Government of India, Atomic Energy Commission: Bombay (1989).
- [21] A. De Ninno, et al., Emission of neutrons as a consequence of titanium-deuterium interaction. *Nuovo Cimento Soc. Ital. Fis.*

- A, 101 (1989) 841.
- [22] A. De Ninno, A. Frattolillo, G. Lollobattista, L. Martinis, M. Martone, L. Mori, S. Podda and F. Scaramuzzi, Evidence of emission of neutrons from a titanium-deuterium system, *Europhys. Lett.*, 9 (1989) 221–224.
 - [23] E. Jones, F.W. Keeney, A.C. Johnson, D.B. Buehler, F.E. Cecil, G. Hubler, P.L. Hagelstein, J.E. Ellsworth and M.R. Scott, Neutron emissions from metal deuterides, In *Condensed Matter Nuclear Science: Proceedings of the 10th International Conference on Cold Fusion*, Cambridge, MA, Aug. 24–29, 2003, P.L. Hagelstein and S.R. Chubb (Eds.), World Scientific, Singapore, 2006, 525–533.
 - [24] A. Shyam and R.K. Rout, Observation of neutrons from palladium deuteride X pinches using a simple low energy capacitor bank, *IEEE Transactions on plasma science* 27 (1999) 1210–1213.
 - [25] T.N. Claytor, M.J. Schwab, D.J. Thoma, D.F. Teter and D.G. Tuggle, Tritium production from palladium alloys, *The 7th International Conference on Cold Fusion*, 1998. Vancouver, Canada; ENECO, Inc., Salt Lake City, UT, p. 88.
 - [26] R. Taniguchi, T. Yamamoto and S. Irie, Detection of charged particles emitted by electrolytically induced cold nuclear fusion, *Jpn. J. Appl. Phys.* 28 (1989) L2021–L2023.
 - [27] A.G. Lipson, B.F. Lyakhov, A.S. Roussetsky and N. Asami, Evidence for DD-reaction and a long-range alpha emission in Au/Pd/PdO:D heterostructures as a result of exothermic deuterium desorption, *Proc. 8th Int. Conf. on Cold Fusion*, May 21–26, 2000, Lerici (La Spezia), Italy, Italian Physical Society, Bologna, Italy.
 - [28] S.E. Jones, F.W. Keeney, A.C. Johnson, D.B. Buehler, F.E. Cecil, G. Hubler, P.L. Hagelstein, J.E. Ellsworth and M.R. Scott, Charged-particle emissions from metal deuterides, In *Condensed Matter Nuclear Science: Proceedings of the 10th International Conference on Cold Fusion*, Cambridge, MA, Aug. 24–29, 2003, P.L. Hagelstein and S.R. Chubb (Eds.), World Scientific, Singapore, 2006, 509–523.
 - [29] J.F. Ziegler, J.P. Biersack, *The Stopping and Range of Ions in Solids*, Pergamon Press, New York (1985).
 - [30] S.E. Jones, D.E. Jones, D.S. Shelton, S.F. Taylor, Search for neutron, gamma and x-ray emissions From Pd/LiOD electrolytic cells: a null result, *Trans. Fus. Technol.* 8 (1994) 143.
 - [31] E. Vilela, E. Fantuzzi, G. Giacomelli, M. Giorgini, B. Morelli, L. Patrizii, P. Serra and V. Togo, Optimization of CR-39 for fast neutron dosimetry applications, *Rad. Meas.* 31 (1999) 437–442.
 - [32] A.R. El-Sersy, N.E. Khaled and S.A. Eman, Determination of CR-39 detection efficiency for fast neutron registration and the absolute neutron dosimetry, *Nucl. Instr. and Meth. in Phys. Res. B* 215 (2004) 443–448.
 - [33] A.R. El-Sersy, Study of absolute fast neutron dosimetry using CR-39 track detectors, *Nucl. Instr. and Meth. in Phys. Res. A* 618 (2010) 234–238.
 - [34] V. Kumar, R.G. Sonkawade and A.S. Dhaliwal, Optimization of CR-39 as neutron dosimeter, *Ind. J. of Pure and Appl. Phys.* 48 (2010) 466–469.
 - [35] T. Tsuruta, T. Niwa and Y. Fukumoto, Experimental, study of CR-39 etched track detector for fast neutron dosimetry, *J. Nucl. Sci. and Technol.* 29 (1992) 1108–1115.
 - [36] J.K. Pálfalvi, J. Szabó, Yu. Akatov, L. Sajó-Bohus and I. Eördögh, Cosmic ray studies on the ISS using SSNTD, BRADOS projects, 2001–2003, *Radiat. Meas.* 40 (2005) 428–432.
 - [37] G.W. Phillips, J.E. Spann, J.S. Bogard, T. VoDinh, D. Emfietzoglou, R.T. Devine and M. Moscovitch, Neutron spectrometry using CR-39 track etch detectors, *Radiat. Prot. Dosim.* 120 (2006) 457–460.
 - [38] http://www.landauerinc.com/uploadedFiles/Healthcare_and_Education/Products/Dosimeters/Neutrak%20Specifications.pdf
 - [39] http://www.cityu.edu.hk/ap/nru/nrures_t.htm
 - [40] S.A. Durrani, Nuclear Tracks today: strengths, weaknesses, challenges, *Rad. Measurements* 43 (2008) S26–S33.
 - [41] R. Mishra, C. Orlando, L. Tommasino, S. Tonnarini and R. Trevisi, A better understanding of the background of CR-39 detectors, *Radiat. Meas.* 40 (2005) 325–328.
 - [42] N. Ishigure and O. Matsuka, Evaluation of background in CR-39 detector for α -particle detection, *Hoken Butsuri* 22 (1987) 287–293.
 - [43] N.A. Al-Liabi, The effects of storage on CR-39, *Isotopenpraxis* 27 (1991) 56–57.
 - [44] C. Brun, M. Fromm, M. Jouffroy, P. Meyer, J.E. Groetz, F. Abel, A. Chambaudet, B. Dörschel, D. Hermsdorf, R. Bretschneider, K. Kadner and H. Kühne, Intercomparative study of the detection characteristics of the CR-39 SSNTD for light ions: present status of the besancon-dresden approaches, *Radiat. Meas.* 31 (1999) 89–98.
 - [45] <http://newenergytimes.com/v2/projects/tgp/Welcom.html>

- [46] F.H. Séguin, J.A. Frenje, C.K. Li, D.G. Hicks, S. Kurebayashi, J.R. Rygg, B.-E. Schwartz, R.D. Petrasso, S. Roberts, J.M. Soures, D.D. Meyerhofer, T.C. Sangster, J.P. Knauer, C. Sorce, V. Yu. Glebov, C. Stoeckl, T.W. Phillips, R.J. Leeper, K. Fletcher and S. Padalino, Spectrometry of charged particles from inertial-confinement-fusion plasmas, *Rev. Sci. Instrum.* 74 (2003) 975–995.
- [47] B. Antolkovic and Z. Dolenec, The neutron-induced $^{12}\text{C}(n,n')^3\text{a}$ reaction at 14.4 MeV in a kinematically complete experiment, *Nucl. Phys. A* 237 (1975) 235–252.
- [48] T. Nakamura, T. Nunomiya, S. Abe, K. Terunuma and H. Suzuki, Sequential measurements of cosmic-ray neutron spectrum and dose rate at sea level in Sendai, Japan, *J. Nucl. Sci. and Technol.* 42 (2005) 843–853.
- [49] A.G. Lipson, G.H. Miley, A.S. Roussetski and E.I. Saunin, Phenomenon of an energetic charged particle emission from hydrogen/deuterium loaded metals, In *Condensed Matter Nuclear Science: Proceedings of the 10th International Conference on Cold Fusion*, Cambridge, MA, Aug. 24–29, 2003, P.L. Hagelstein and S.R. Chubb (Eds.), World Scientific, Singapore, 2006, 539–558.
- [50] A.K. Pandey, R.C. Sharma, P.C. Kalsi, R.H. Iyer, Measurement of alpha to fission branching ratios of heavy actinides by sequential etching of alpha and fission tracks in CR-39, *Nucl. Instrum. and Meth. in Phys. Res. B*, 82 (1993) 151–155.
- [51] D. Paul, D. Ghose, R.C. Sastri, An SSNTD study of spontaneous fission fragments from the soil-gas samples of Bakreswar thermal springs, *Rad. Meas.*, 33 (2001) 167–169.
- [52] M. Luszik-Bhadra, F. d'Errico, L. Lusini, B. Wiegel, Microdosimetric investigations in a proton therapy beam with sequentially etched CR-39 track detectors, *Rad. Prot. Dosim.*, 66 (1996) 353–358.
- [53] M. Fromm, F. Membrey, A. El Rahamany, A. Chambaudet, Principle of light ions micromapping and dosimetry using a CR-39 polymeric detector: modelized and experimental uncertainties, *Nucl. Tracks and Rad. Meas.*, 21 (1993) 357–365.
- [54] D. O'Sullivan, D. Zhou, W. Heinrich, S. Roesler, J. Donnelly, R. Keegan, E. Flood and L. Tommasino, Cosmic rays and dosimetry at aviation altitudes, *Radiat. Meas.*, 31 (1999) 579–584.
- [55] D. O'Sullivan, D. Zhou, E. Semones, W. Heinrich and E. Flood, Dose equivalent, absorbed dose and charge spectrum investigations in low earth orbit, *Adv. Space Res.*, 34 (2004) 1420–1423.
- [56] D. Zhou, E. Semones, R. Gaza, S. Johnson, N. Zapp and M. Weyland, Radiation measured ISS-expedition 12 with different dosimeters, *Nucl. Instr. Meth.*, A580 (2007) 1283–1289.
- [57] D. Zhou, E. Semones, R. Gaza, S. Johnson, N. Zapp, M. Weyland, R. Rutledge and T. Lin, Radiation measured with different dosimeters during STS-121 space mission, *Acta Astron.*, 64 (2009) 437–447.
- [58] D. Zhou, E. Semones, R. Gaza, S. Johnson, N. Zapp, K. Lee and T. George, Radiation measured during ISS-expedition 13 with different dosimeters, *Adv. Space Res.*, 43 (2009) 1212–1219.
- [59] D. Zhou, E. Semones, D. O'Sullivan, N. Zapp, M. Weyland, G. Reitz, T. Berger and E.R. Benton, Radiation measured for MATROSHKA-1 experiment with passive dosimeters, *Acta Astron.*, 66 (2010) 301–308.



Research Article

Transient Vacancy Phase States in Palladium after High Dose-rate Electron Beam Irradiation

Mitchell Swartz *

JET Energy Inc., Wellesley Hills, MA, USA

Peter L. Hagelstein

Massachusetts Institute of Technology, Cambridge, MA, USA

Abstract

A high voltage electron irradiator was used to generate high vacancy content VP metal samples. High Frenkel defects (FD) content (vacancy phase) metal samples of Pd and Ni were generated by a single treatment with a high voltage electron irradiator (2.5 MV electrons, 2500 Gray/s dose rate, single portal, 1.50–3.0 megaGray midplane dose) at room temperature. These irradiation-synthesized, vacancy-phase (ISVP) metals were examined for their room-temperature annealing rate using four-terminal conductivity measurements. We show that high dose rate supervoltage irradiated palladium and nickel can achieve saturation densities of defects at the level of a few tenths percent and that level can be followed with the appearance of lattice quakes repairing the damage. The most heavily irradiated samples developed incremental electrical resistivities of $\sim 4 \mu\Omega\text{-cm}$, with rapid recovery consistent with room-temperature annealing. The early labile vacancy phase state of ISVP metals has a half-life ~ 2.5 h. Lattice quakes are observed when electrical transduction spectroscopy is used to monitor the lattice healing and vacancy recombination. The irradiation produced an effective increase in the cross-sectional area of the palladium wires (99.98% pure) of $\sim 2.5\%$ at 3 megaGray delivered, consistent with the literature.

© 2014 ISCMNS. All rights reserved. ISSN 2227-3123

Keywords: CF materials, Electrode Irradiation, Fukai states, Superabundant vacancies, Vacancy phase metals

1. Introduction – Frenkel Defects and Lattice Vacancies

1.1. Frenkel defects

A Frenkel defect (FD) (each a paired entity) is a lattice “hole” AND its counter-defect which is simultaneously produced when an atom jumps from its normal position to an interstitial site, such as secondary to bombardment from a high energy incident neutron, electron, or other particle [1]. Frenkel defects must be distinguished from Schottky defects where atoms move to the grain boundaries, and surfaces, leaving the vacancies far behind.

*E-mail: mica@theworld.com

Why are Frenkel defects (FD) important to cold fusion and lattice-assisted nuclear reactions (LANR)? FD are important to excess enthalpy reactions (CF or LANR) because they create empty lattice sites which are possibly nuclear active sites for the desired reactions. In addition, they can be stabilized by hydrogen atoms in the metal lattice, and – on some occasions – the FD themselves can become further ordered, and that too may also play a role in CF/LANR. For example, requisite deuterons, or their clusters, could enter the sites [2–5], including by Anderson focusing [5].

Furthermore, FD aggregation may be a *second sine qua non* for the success of excess enthalpy reactions in hydrogen (and deuteron) loaded metals – after high loading. As is now known, full loading of metals such as palladium with deuterons is the first *sine qua non* [6–8] but insufficient for the reactions which generate excess enthalpy; there is also required a time period of weeks [9]. One hypothesis suggested at ICCF-10 is that FD are diffusing into the metal lattice, and that diffusion is the reason for the long wait before the appearance of the desired excess enthalpy reactions. One relationship to CF/LANR is that up to several (perhaps 6) deuterons (10) can be associated with each FD, and they selectively enter the defects during deuteron flow producing critically required effects before the desired reactions appear [5]. Figure 1 shows the FD (vacancy) density, and electrical resistivity ($\mu\Omega\text{-cm}$).

These values are plotted in two dimensions both as a function of time and delivered dose. Shown are the FD Density and ρ for theoretically “pure” palladium, what was actually measured in the control specimen, and what was observed for irradiated Pd specimens (ISVP) to which 1.5 and 3.0 megaGray dose were delivered.

Paired FD (vacancies) in pure metals are well known, but are transient and recombine rapidly, driven by the 1.5 eV released per combining defect pair. And so, FD are present in pure metals only at very low concentrations –

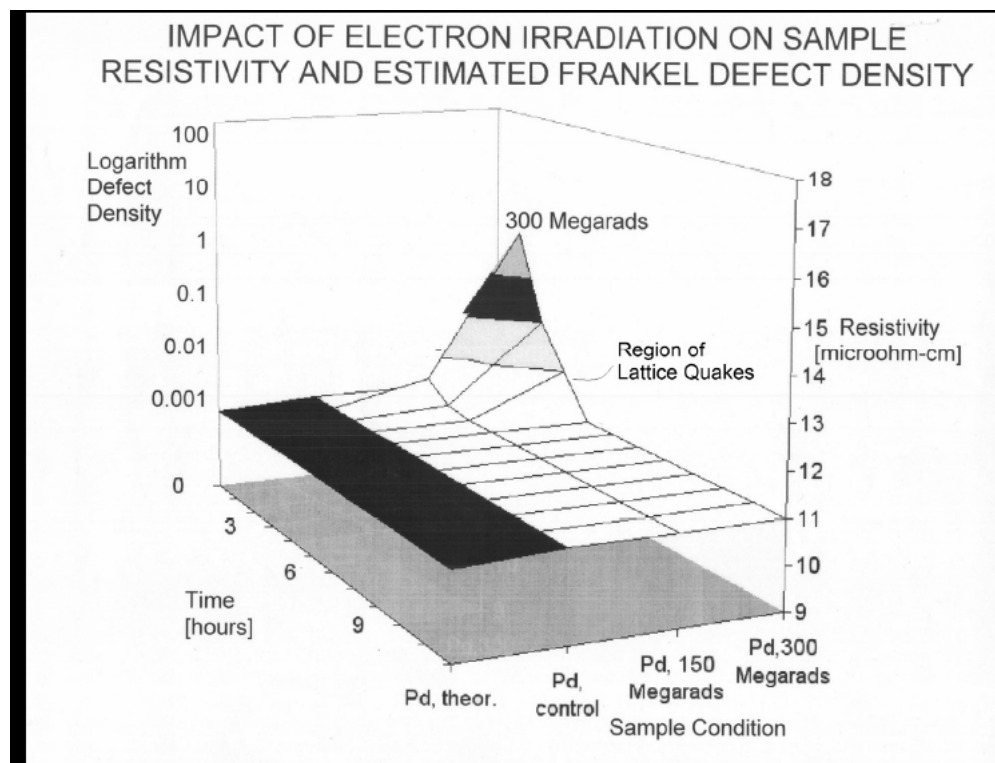


Figure 1. Frenkel Defect (vacancy) density, and electrical resistivity ($\mu\Omega\text{-cm}$).

Table 1. Some properties of irradiation-induced FD.

Enthalpy of formation	0.32 eV	Fukai
Number of hydrogen trapped in a vacancy	6 (for Pd)	Fukai
Diffusivity (cm ² /s)	10 ⁸	
Theoretical max possible concentration	7.7%	Fecht (Fuk)
Peak achievable vacancies in Pd	18 at.%	Fuk
Remnant vacancies after annealing	1/3	
Specific incremental resistivities of some metals ρ_F ($\mu\Omega$ -cm) per at. %		
Cu	1.3, 2.0	von Hippel, Ehrhart and Schlagheck
Al	3.9	Ehrhart and Schlagheck
Ag	1.5	von Hippel
Au	1.5	von Hippel
Ni	7.1	Bender and Ehrhart
Pd	900 ¹⁰⁰	

unless some procedure has specifically been used to generate them and if means are also provided to halt thermally driven recombination of such vacancies [11]. When formed, the Frenkel pair defects (often termed ‘vacancies’ or discomposition in the literature) are characterized by diffusivities and the induced specific electrical resistivities listed in Table 1.

Palladium hydrides have been long studied [12–16]. When FD defects are produced in large quantities in select Group VIII metals such as when hydrogen atoms (well known from the hydrides of such metals) stabilize them, the defects can, on occasion, form ordered clusters [17–20]. These were first noted in 1994, during X-ray diffraction studies, when Fukai [17,18] discovered that palladium lattices filled with hydrogen could undergo a irreversible lattice contraction at high temperatures into an ordered state, and one with characteristic features of vacancy formation. What was most interesting was that this new observed phase of matter had concentrations of vacancies (up to circa 30%) which were many orders of magnitude greater than had ever been seen previously. These ordered states of hydrides are, therefore, called super abundant vacancies (SAV) or Fukai states. Surprisingly, these HTHP FD have vacancies which are stable following outgassing of the hydrogen, and on occasion can be observed to form ordered clusters. Such high FD/vacancy state metals are referred to as vacancy phase (VP) materials. These include ordered vacancy phases and new types of lower density hydrided “pure” metals and alloys.

1.2. Vacancy phase metals

The generation of FD, and possible attainment of high levels of VP metals is reasonably well understood theoretically. In hydrogen loaded palladium, FD defects can exist a bit longer, stabilized by the electronic structure of the loaded PdH. Their existence is still limited by the vacancy diffusion rate and the very low production rate of vacancies. Hydrogen atoms and the FD stabilize each other by a few tenths of an eV per neighboring hydrogen. In NiH, a metal vacancy is energetically favored by ~ 0.5 eV; in PdH by a few tenths of an eV. These numbers should be compared to the ~ 1.5 eV formation energy required for FD (vacancy) creation in the pure metal. As a result of the stabilization, thermodynamics predicts that the number of hydrided metal lattice vacancies, which can exist in loaded NiH and PdH, can be limited by the vacancy diffusion rate and the production rate of vacancies [5]. The dynamics of such ordered cluster formation is complicated; and that includes because interstitials which can impede the clustering formation, and because other isotopes of hydrogen (H vs. D) can impede the loading.

Increased quantities of FD in metals can be generated by near-melting temperatures, by high temperature-high pressure systems [21] and by electron [5,17,18, 21–25] or neutron irradiation, and torsion [20]. The first (and easiest) method takes the metal just below the melting point to generate vacancies which are then frozen into position by

lowering the temperature. This procedure attains a maximum vacancy concentration of 0.1%. The FD production rate can be increased when metals are irradiated by a flux of high energy electrons. Metals irradiated with neutrons or supervoltage (>1.5 MV) electrons at high doses, and high dose rates, achieve a saturation density of defects that are a few tenths of a percent, and involving many modes of annealing. There is also much interest in the high temperature high pressure (HTHP) vacancy phase (VP) synthesis because of the observation of $\sim 25\%$ metal FD in NiH and 18% in PdH developed by the anvil-presses on six sides of the samples [17].

Both the FD, the rarer clusters, and SAV which can form from them, are observable through their Huang anomalous scattering [26–29], and relatively strong small-angle X-ray scattering, respectively. Huang scattering [26] is the development of relatively wide angle diffuse scattering produced by the vacancies upon the very sharp diffraction peaks which characterize x-ray diffraction images of “pure” perfect crystals.

Previously, we briefly reported the presence of transient vacancy phase states [30] and the performance of vacancy phase nickel cathodes in ordinary water [31]. This paper reports further investigations which were made on electron-irradiation-induced metal lattice dislocations and vacancies in palladium. We use two units of irradiation here. The first is the dose delivered to the material, which is Gray (where 100 rads is one Gray). The second is the normalized fluence (flux) of electrons (number of electrons/cm²) which actually generates that delivered dose.

2. Experimental: Materials and Methods

Palladium samples (wire, annealed post cold-drawn, lot “Z” (IMRA), Johnson Matthey (99.98%, nominal 1.0 mm diameter, 1 cm length, generally characterized with the 311 metal crystalline axis being perpendicular to the long axis of the wires) were used. To correct for geometric factors, the physical size of the wires were measured using a Sylvac caliper (Fowler Type Ultracal-III, Newton MA; spatial resolution 0.01 mm, accuracy 30 μ m, precision 10 μ m). The sample wires were measured, before and sequentially after irradiation, for diametric changes at 0, 45 and 90 degree angles along their entire length in the setup configuration. Thereafter, diametric measurements and four-terminal conductance measurements were used with the geometric sample factors to derive the semiquantitative electrical conductivity of the samples.

Dual Angle X-ray spectroscopic examination was performed on some of the palladium wire samples to determine the impact of loading pre-irradiation Spectroscopic curves were generated using a Cu anode, 300 mA, 60 kVp; 1/2 degree scatter slit, 1/2 degree divergence slit, Molybdenum vertical collimators, 0.15 mm receiving slit, dose rate ~ 10 kiloGray per second, with a scan rate 0.25 degrees/min at 0.02 degree increments for fine structure determination.

To generate high vacancy content metal samples, a high voltage electron irradiator was used to produce damage for all experiments, except the controls. A van de Graaff was adjusted to deliver 2.5 MV electrons [32] at ultrahigh dose rate at the MIT High Voltage Research Laboratory (~ 2500 Gray/s dose rate) with a single portal over 20 min to 1.5–3 megaGray midplane dose with the samples located approximately 7 cm from the horn. All samples were located within that peak cross-section of the incident beam. The irradiated wires were arranged on filter paper (Whatman #1, 9.0 cm) and irradiated perpendicular to their long axis. No rearrangement was used during irradiation, but half the samples were removed midway through the irradiation procedure. The wires were handled by their penultimate terminal segments, <1.5 mm). They were contained in polypropylene or polyethylene; and kept at room temperature, except during irradiation.

The presence of vacancies was qualitatively estimated through the changes observed by electrical resistivity measurements performed before and after irradiation. A significant increase in the resistivity was caused by the substantial defect production after the single dose irradiation, and thereafter the resistivity and sample area were examined, metachronously. (In contrast to synchronous, metachronous means later, after the event.)

The electrical conductivity was monitored by a four-terminal measurement (Keithly 225 current source, 610C electrometer). In control experiments determined that when sample input power exceeds 20 nW (~ 3 nW for gold),

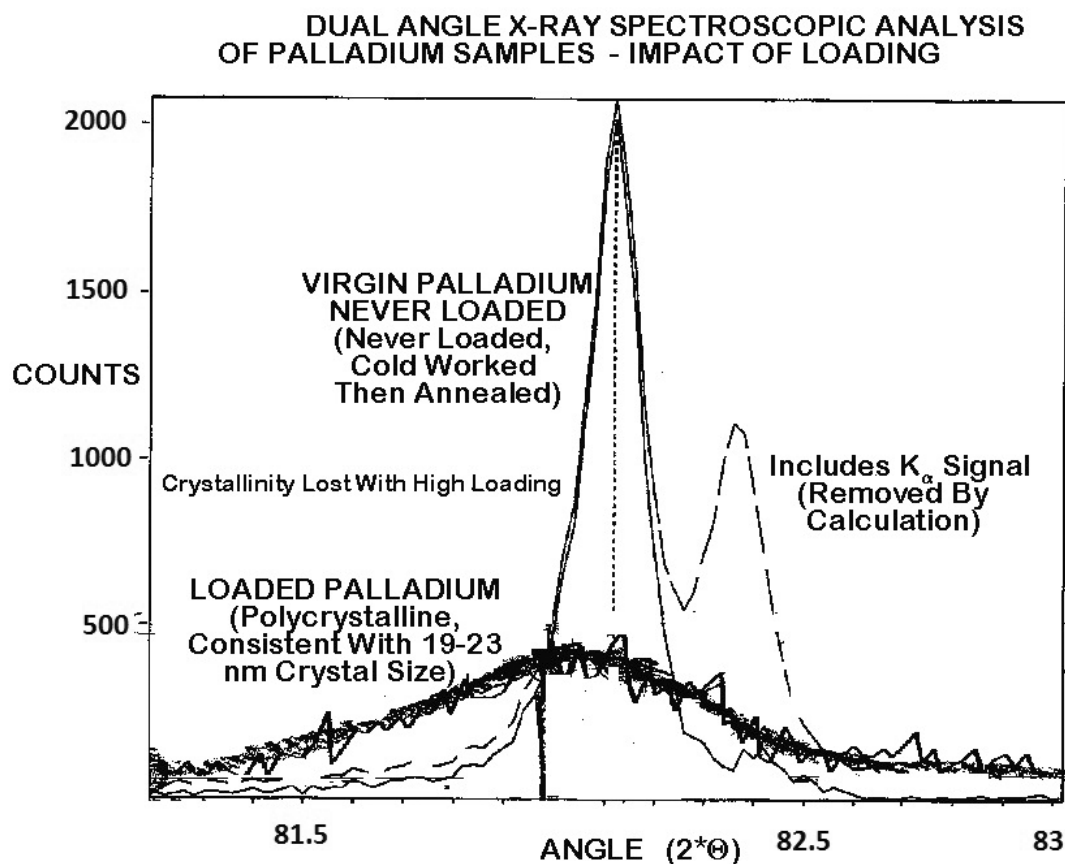


Figure 2. Dual angle X-ray spectroscopic examination of the of palladium wire.

there resulted a degree of electrical dissipation sufficient to generate stable electrical conduction measurements using this system. All measurements thereafter exceeded that minimum power dissipation.

3. Results

Figure 2 shows three X-ray spectroscopic curves for two palladium samples. They are a “virgin” palladium wire (prior to both loading with hydrogen and prior to irradiation), and a palladium wire after loading with hydrogen. The virgin control wire had been annealed and cold worked. The thin solid curves are for the virgin wire. The thin dashed curve is the raw data which includes both of the $K_{\alpha 1}$ and $K_{\alpha 2}$ peaks which are characteristic of the horizontal rocking system. These are corrected in the thin solid curves. The thicker and broader curve is the output of a hydrided (loaded to 0.95) palladium wire.

One result of this measurement was the corroboration that these palladium wires tended to have their crystallographic 311 vector perpendicular from the long axis of the palladium wire. Another result is that loading severely changed the lattice structure. All curves in Fig. 5 demonstrate the 311 characteristic peak (plotted as $2^*\theta$). Relatively,

this is especially true for the virgin palladium wire compared to the loaded wire. The virgin wires have much greater magnitude of the 311 peak.

Three X-ray spectroscopic curves are shown (300 mA, 60 kVp) as discussed in the text.

Figure 3 shows the diameter of palladium wires three days following a single irradiation dose. The size of the wire in millimeters is shown as a function of given dose. The results of eight (8) wires are shown. The range of thicknesses of palladium wires are shown three days after electron beam irradiation. The limits show the range of measurements (two standard deviations). Two given irradiation doses (1.5 and 3 megaGray) are shown, along with the controls (that is unirradiated or “virgin”) palladium wire.

The palladium samples (nominally “1.0 mm”) were ~ 1.01 mm diameter, and their diameter increased with remnant structure damage for days following a single irradiation dose (Fig. 3). Their girth increased for those most highly irradiated samples to 1.02 mm. The produced effective increase in the cross-sectional area of the palladium wire (99.98% pure) was 0.75% at 1.5 megaGray, and was ~ 2 –2.5% at 3 megaGray delivered dose (standard deviation ~ 10 –20 μm).

The results of eight (8) different wires are shown. The range of thickness of palladium wires are shown three days after the single electron beam irradiation of all samples (nominally “1.0 mm”).

By the use of area measurement here with the measured electrical resistance, a semi-quantitative correction for the irradiated wire electrical resistivities were derived (Figs. 1 and 2). Figure 4 shows the palladium wire electrical

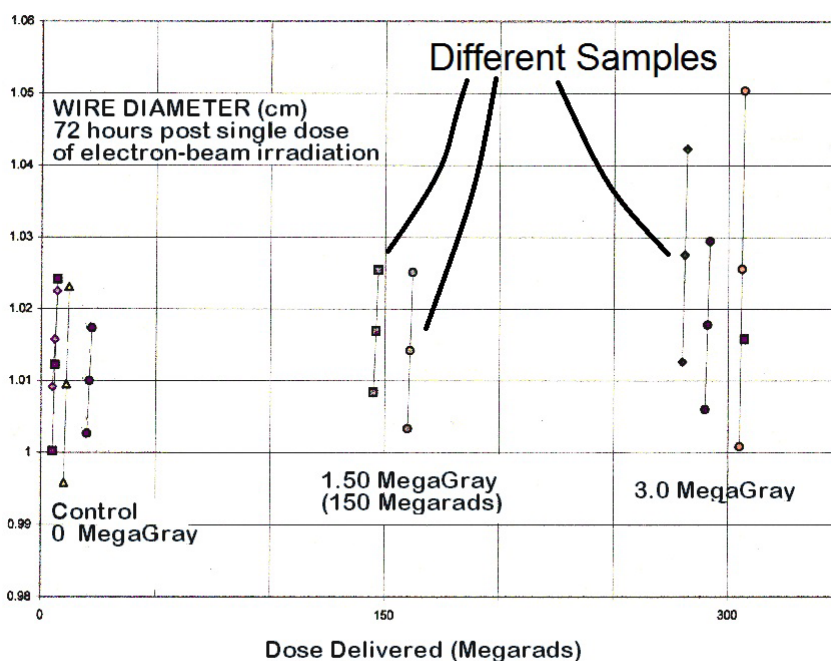


Figure 3. Palladium wire diameter three days after electron-beam irradiation-created vacancy states.

resistivity after its single-dose electron beam irradiation. This curve shows the electrical resistivity of a palladium wire sample (99.99%) over time. At $t = 0$, the single dose electron beam irradiation occurred. The palladium sample received 3.0 megaGray midplane dose over twenty minutes. The electrical resistivity is compared with the theoretical expected resistivity of “pure” palladium.

The most heavily irradiated samples developed increased resistivities of as much as $4 \mu\Omega\text{-cm}$. This fell off with a half-life of approximately 2–3 h, until by 6 h after irradiation the resistivity was approximately $11.5 \mu\Omega\text{-cm}$ (Fig. 4). There appear to be two distinct falloff regions of electrical resistivity, with final drift back toward the normal resistivity of virgin samples. Following the rapid falloff region shown in Fig. 1 with the half-life of 2.5 h is a region of slower resistivity falloff in the range of $2.4 \times 10^{-5} \mu\Omega\text{-cm/s}$ (over circa a range of 6–9 h). This shows the post-irradiation, loss of Fukai state material over 20 min. The electrical resistivity of the virgin (unirradiated) Pd samples were approximately 1.01% greater than theoretically expected (expected $10.8 \mu\Omega\text{-cm}$, measured 10.909). This resistivity of the samples postirradiation was time-dependent consistent with room-temperature annealing as shown in Figs. 1, 4 and 5.

The upper curve shows the electrical resistivity of a palladium wire sample (99.99%) over time before, and after

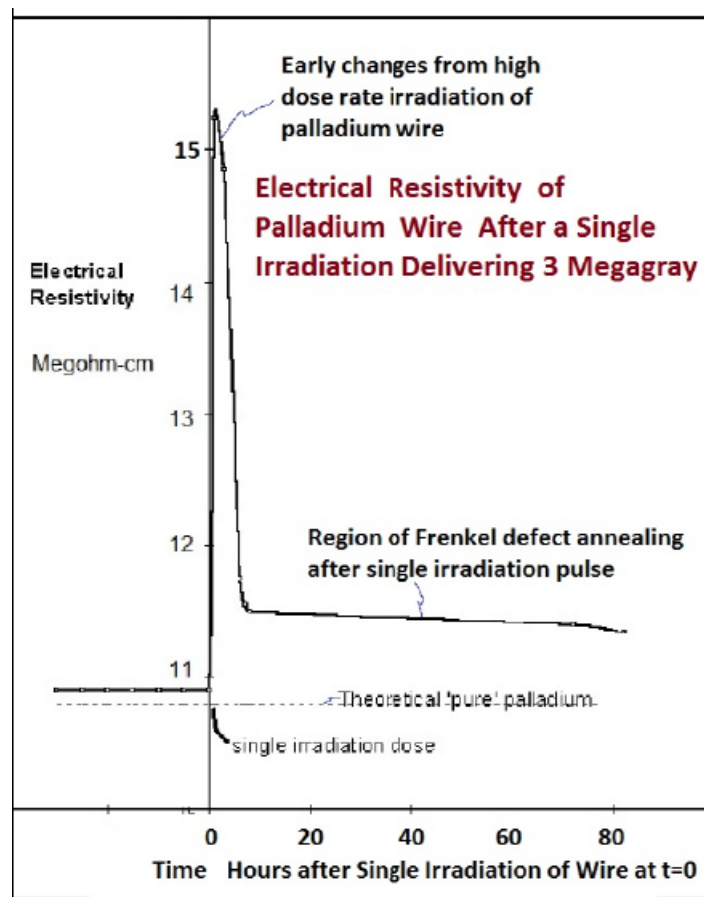


Figure 4. Palladium wire electrical resistivity post electron beam irradiation.

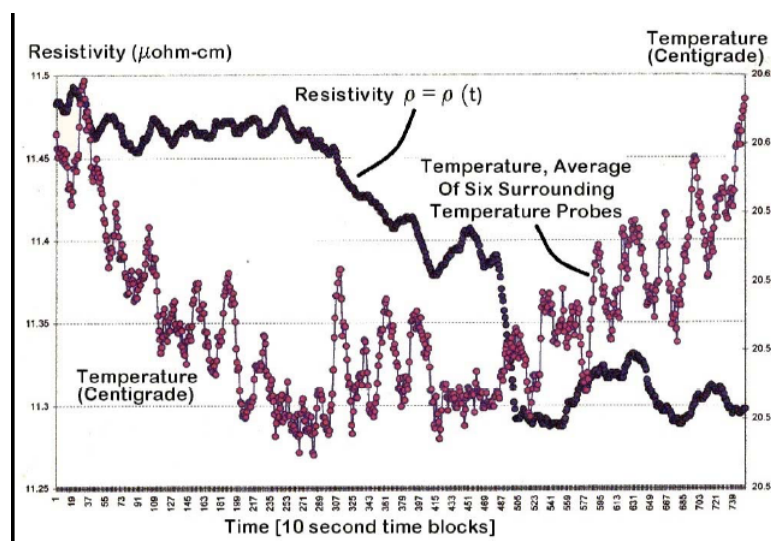


Figure 5. Fine structure of palladium sample resistivity as a function of time, following electron beam irradiation.

irradiation at $t = 0$. The palladium sample received 3.0 megaGray midplane dose over twenty minutes. The electrical resistivity is compared with the theoretical expected resistivity of “pure” palladium, which is the lower dashed curve.

Figure 5 shows the fine structure of a palladium sample’s electrical resistivity following its electron beam irradiation. Of special interest are the lattice –quakes. In Fig. 5, two curves are shown. The upper, thicker, curve is the electrical resistivity of the sample over time (in 10 s time blocks) and demonstrates the fine-structure changes which occur during room-temperature annealing. The palladium wire sample received 3.0 megaGray. The second curve (solid dots) shows the average temperature of six thermocouple probes used to examine the immediate environment around the sample.

The upper, thick, curve is the electrical resistivity of the sample over time, in 10 s time blocks. The fine-structure changes are room-temperature annealing. The second lower curve (solid dots) shows the average temperature of six thermocouple probes used to examine the immediate environment around the sample.

4. Discussion and Interpretation

There exists major, yet significantly recoverable, effects wrought upon palladium wire samples following high dose-rate electron beam irradiation yielding large numbers of FD. High FD content (vacancy phase) metal samples were generated by a single treatment with a high voltage electron irradiator (2.5 MV electrons, 2500 Gray/s dose rate, single portal, 1.5–3.0 megaGray mid-plane dose) at room temperature, initially, and they were transient.

Irradiation produced an effective increase in the cross-sectional area of the palladium wires (99.98% pure) of 0.75% at 1.5 megaGray, and as much as 2–2.5% at 3.0 megaGray delivered dose, consistent with the literature. This finding of volumetric expansion of the irradiated wires is consistent with the literature because it is well known that irradiation of metals causes lattice site breakdown and that the creation of defects so wrought increases the volume (and in this case area).

The most heavily irradiated samples developed incremental resistivities of $\sim 4 \mu\Omega\text{-cm}$ (virgin unirradiated sample resistivities and theoretical resistivities of 10.9 and 10.8 $\mu\Omega\text{-cm}$). This electrical resistivity of the samples, post-

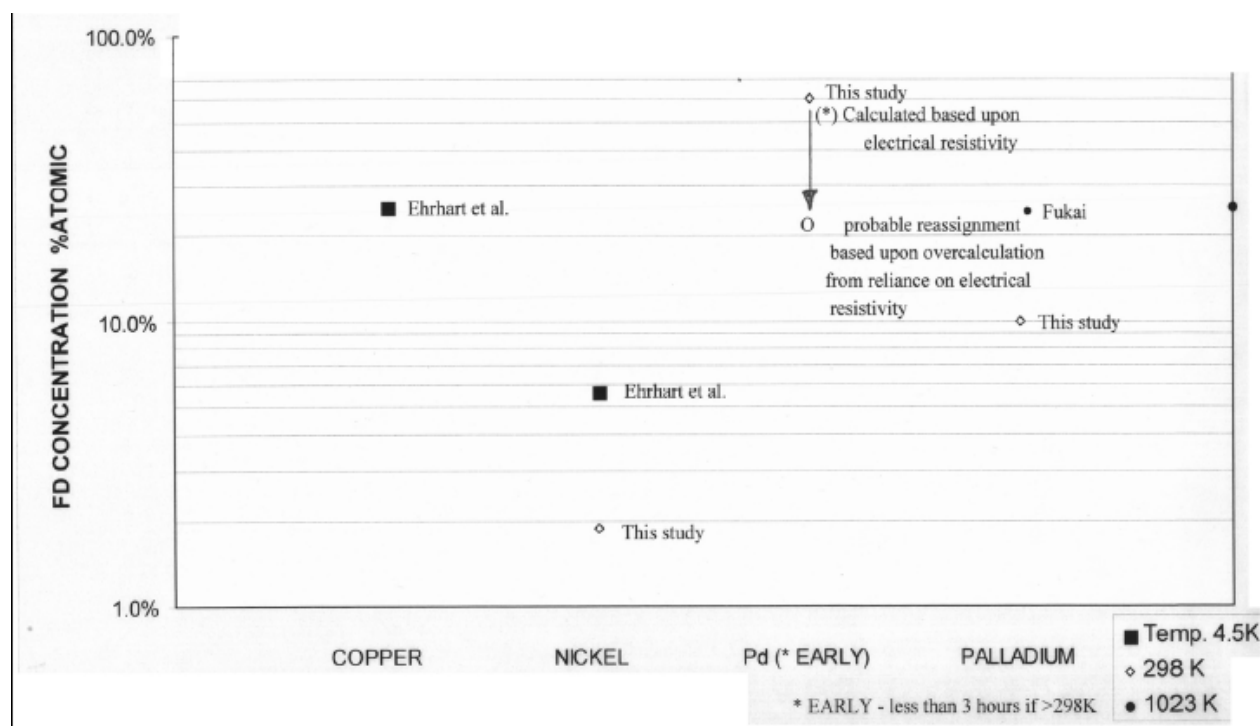


Figure 6. Induced incremental derived FD concentrations in palladium and other metals.

irradiation, was time-dependent, consistent with room-temperature annealing. In palladium, post 3 megaGray, after the rapid early falloff (half-life ~ 2.5 h) there is a region of fewer induced FD and a much slower resistivity falloff ($\sim 2.4 \times 10^{-5} \mu\Omega\text{-cm/s}$).

In palladium, we have separated the annealing of irradiation-induced vacancies into two phases of FD recombination and loss. The first has the possible appearance of a level of vacancies similar to those described by Fukai [17,18]. The latter short-lived phase occurs within hours and are levels consistent with the other electron irradiation reports [16, 21–25].

Lattice quakes are observed in the second region. The fine structure of the electrical resistivity (Fig. 5) shows that in intermediate time region, most observable at circa 7–9 h after the irradiation, there can be seen these complex dynamic structural changes.

Figure 6 plots from several experiments the induced incremental derived FD concentrations in palladium, and other metals, as both obtained by electron irradiation here, compared to the high temperature-high pressure (HTHP) system.

These are the incremental induced derived FD concentrations, for metals, obtained by electron irradiation. Here, results are compared to the high temperature-high pressure (HTHP) systems.

In these palladium samples, post high dose irradiation, based on the electrical resistivity changes, the calculated FD concentration (% atomic FD) within the first 3 h post-irradiation was in the range of ~ 30 – 45% . We believe that this is an over-calculation based upon reliance on electrical resistivity; and that the more likely range obtained was ~ 20 – 30% , similar to that reported by Fukai for palladium and by Ehrhart for copper.

In the longer term, the calculated FD concentration was in the range of 8–10%. The FD formation rate as function

of the electron irradiation flux is estimated at 10–60% atomic FD/coulombs/cm² within the first 3 h post-irradiation. In the longer metachronous post-irradiation period, this decreased to 7–10% atomic FD/coulombs/cm². These levels are greater by more than orders of magnitude than those observed for copper and nickel [25].

By contrast, in nickel, electron bombardment by 3 MeV leads to vacancy concentrations of 0.0003–0.0007 for $1\text{--}2 \times 10^{18}$ electrons/cm², with a defect saturation of about 0.0018. These nickel control experiments produced short-lived defects, fewer in number than those left frozen in at 4.5 K.

5. Conclusion and Summary

In summary, electron irradiation offers opportunity for larger levels of defects than that achieved by other methods. FDs, and ordered vacancy phase (VP) solids loaded with FDs, may be important because they offer new materials with novel properties arising because of stabilizing hydrogen atoms offering a few tenths of an eV per neighboring hydrogen.

From a materials point of view, one important impact of these findings is that by electron-irradiating Group VIII metals, there may be opportunity for obtaining larger concentrations of FD than achieved by other methods. Competing kinematics, and other metallurgical issues, make producing large amounts of such defects (vacancy phase metals) quite difficult. However, metals loaded with hydrogen, such as deuterium in palladium, can change all that.

Another implication is also that electrical transduction spectroscopy, normally used to monitor hydride loading in the Group VIII metals, can also examine the lattice healing and vacancy recombination, through these lattice-quakes.

Another impact of this work is that, looking forward, wire diameter should be considered during electron beam irradiation or hydrogen loading so as to further supplement and correct Archimedic estimations and X-ray spectroscopic deduction of the loading. Specifically, correction for geometric factors to determine the electrical resistivity will improve loading determinations based on the variation of resistance for the b phase palladium following loading with deuterons [33]. Electrical resistivity, rather than electrical resistance, may be more important because it is indicative of material composition by removal of the geometric factors. Although X-ray spectroscopy can be used to evaluate lattice spacing, samples should be physically followed thereafter to correct for their changing geometric size.

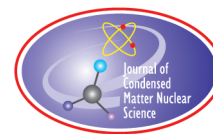
Acknowledgment

The authors acknowledge and thank JET Energy, Inc. for support of this work, and to Gayle Verner and Dr. Alex Frank for their very helpful comments. The authors are also grateful to J. Adario at MIT who performed x-ray spectroscopy, Kenneth Wright of MIT HVRL for meticulous engineering of the irradiation, Michael McKubre and Fran Tanzella for loading the Pd sample, and the Department of Electrical Engineering and DARPA for support at MIT.

References

- [1] A. von Hippel, Molecular Science and Molecular Engineering, MIT Press, Cambridge, USA, 1959.
- [2] G. Miley, X. Yang and H. Hora, Ultra-high density deuteron-cluster electrode for low-energy nuclear reactions, *J. Condensed Matter Nucl. Sci.* **4** (2011) 256–268.
- [3] P. Tripodi, N. Armanet, V. Asarisi, A. Avveduto, A. Marmigi, J.D. Vinko, J. Biberian, The effect of hydrogenation/dehydrogenation cycles on palladium physical properties, *Phys. Lett. A* **373** (2009) 3101–3108.
- [4] P. Tripodi, N. Armanet, V. Asarisi, A. Avveduto, A. Marmigi, J. Biberian, J.D. Vinko, The effect of hydrogen stoichiometry on palladium strain and resistivity, *Phys. Lett. A* **373** (2009) 4301–4306.
- [5] M. Swartz, Catastrophic active medium hypothesis of cold fusion, *Proc. Fourth International Conference on Cold Fusion*, Vol. 4, sponsored by EPRI and the Off. Naval Research, 1994.

- [6] A. Takahashi and N. Yabuuchi, Study on 4D/TSC condensation motion by non-linear Langevin Equation, American Chemical Society LENRSB1, 57–83, 2008; A Takahashi, Physics of Cold Fusion by TSC Theory, *J. Physical Science and Application* **3**(3) (2013) 191–198.
- [7] M. McKubre, F. Tanzella, P. Hagelstein, K. Mullican and M. Trevithick, The need for triggering in cold fusion reactions, *Proc. ICCF-10*, Cambridge, MA, 2003.
- [8] M. Swartz, Survey of the observed excess energy and emissions in lattice assisted nuclear reactions, *J. Scientific Exploration* **23**(4) (2009) 419–436.
- [9] M.R. Swartz, Phonons in nuclear reactions in solids, *Fusion Technol.* **31** (1997) 228–236.
- [10] M.R. Swartz and G. Verner, Excess heat from low electrical conductivity heavy water spiral-wound Pd/D₂O/Pt and Pd/D₂O-PdCl₂/Pt Devices, *ICCF-10*, Cambridge, MA, 2003.
- [11] P. Hagelstein and M. Swartz, Optics and Quantum Electronics, *MIT RLE Progress Report* **139** (1) (1997) 1–13.
- [12] B. Baranowski, *Plat. Met. Rev.* **16** (1972) 10.
- [13] A.W. Szafranski, *Phys. Status Solidi (A)* **19** (1973) 459.
- [14] F.A. Lewis, *The Palladium Hydrogen System*, Academic Press, London, 1967.
- [15] A.W. Szafranski and B. Baranowski, *Phys. Status Solidi (A)* **9** (1972) 435.
- [16] B. Baranowski and R. Wisniewski, *Phys. Status Solidi* **35** (1969) 593.
- [17] Fukai and N. Okuma, Formation of superabundant vacancies in Pd hydride under high hydrogen pressures, *Phys. Rev. Lett.* **73** (1994) 1640.
- [18] Fukai, Formation of superabundant vacancies in metal hydrides at high temperatures, *J. Alloys & Compounds* **231** (1995) 35–40.
- [19] Zhang and C.A. Alavi, First principles study of superabundant vacancy formation in metal hydrides, *J. Am. Chem. Soc.* **127** (2005) 9868–9817.
- [20] M. Krystian, D. Setman et al., Formation of superabundant vacancies in nano PdH generated by high pressure torsion, *Scripta Materialia* **62** (2010) 49–52.
- [21] P. Ehrhart and U. Schlagheck, Investigation of Frenkel defects in electron irradiated copper by Huang scattering of X-rays, *J. Phys. F: Metal Phys.* **4** (1974) 1575–1587.
- [22] P. Ehrhart, Diffuse X-ray scattering studies of neutron- and electron-irradiated Ni, Cu and dilute alloys, *Philosophical Mag. A* **60** **3** (1989) 283–306.
- [23] P. Ehrhart and W. Schilling, Investigation of interstitials in electron irradiated aluminum by diffuse X-ray scattering experiments, *Phys. Rev B* **8**(6) (1973) 2604–2621.
- [24] O. Bender and P. Ehrhart, Self-interstitial atoms, vacancies, and their agglomerates in electron-irradiated nickel investigated by diffuse scattering of X-rays, *J. Phys. F: Metal Phys.* **13** (1983) 911928.
- [25] P. Ehrhart, Investigation of radiation damage by X-ray diffraction, *J. Nuclear Materials* **216** (1994) 170–198.
- [26] K. Huang, X-ray reflexions from dilute solid solutions, *Proc. Roy. Soc. A* **190** (1947) 102–117.
- [27] R.I. Barabash, J.S. Chung and M.F. Thorpe, Lattice and continuum theories of Huang scattering, *J. Phys.: Condens. Matter* **11** (1999) 3075–3090.
- [28] P.R. Dederichs, The theory of diffuse X-ray scattering and its application to the study of point defects and their clusters, *J. Phys. F: Metal Phys.* **3** (1973) 471–496.
- [29] P. Ehrhart and H. Trinkaus, Diffuse scattering from dislocation loops, *Phys. Rev. B* **25** (2) (1982) 834.
- [30] M. Swartz, P.L. Hagelstein, G. Verner and K. Wright, Possible transient vacancy phase states, Abstract *ICCF-7 in The Seventh Int. Conference on Cold Fusion*, Vancouver, Canada, 1998.
- [31] M. Swartz, P.L. Hagelstein, G. Verner and K. Wright, Vacancy phase nickel cathodes, Abstract *ICCF-8, in 8th International Conference on Cold Fusion*, Lerici (La Spezia), Italy: Italian Physical Society, Bologna, Italy, 2000.
- [32] N. duV. Tapley, *Clinical Applications of Electron Beam*, Wiley, NY, 1976.
- [33] S. Crouch-Baker, M.C.H. McKubre and F.L. Tanzella, Variation of Resistance with Composition in the b-Phase of the H–Pd System at 298 K, *Zeitschrift für Physikalische Chemie, Bd.* **204**(S)(1998) 247–254.



Research Article

On the Mechanism of Tritium Production in Electrochemical Cells

Stanislaw Szpak^{*,†} and Frank Gordon^{‡,§}

SPAWAR Center San Diego, CA, USA

Abstract

An electron capture reaction $e^- + d^+ \rightarrow 2n$ followed by deuteron to triton transmutation, the $n + d^+ \rightarrow t^+$ reaction, is judged to be the prime reaction in polarized Pd/D–D₂O system. Supporting evidence for the proposed mechanism is interpreted and discussed in terms arising from the content and meaning of chemical and nuclear reactions occurring in condensed matter.

© 2014 ISCMNS. All rights reserved. ISSN 2227-3123

Keywords: Co-deposition, Polarized Pd/D–D₂O system, Tritium production

1. Introduction

The substitution of cathodes prepared by the Pd+D co-deposition for massive palladium when applied correctly assured a 100% reproducibility in excess power generation. It was expected that they will reproducibly produce tritium as well. Indeed, this was the case. Samples of electrolyte from ten (10) cells were sent to Stanford Research Institute (Dr McKubre) and to University of Utah (Prof. Pons) for analysis. All showed marked increase in tritium concentration. In what follows, we examine the arguments leading to the proposed model of tritium production. These arguments are based on evidence resulting from the work done in the laboratory at the SPAWAR Center. The purpose of this communication is not to review the published literature, but to emphasize the connection between the event, e.g. $e^- + d^+ \rightarrow 2n$ reaction and the removal and transport of tritium from the reaction space to the environment in which they occur. To avoid misunderstanding, we define the content and meaning of the background material using terminology common in reporting results of chemical research.

2. Background Material

Fleischmann et al. [1], noted that nuclear reactions in a host lattice are affected by coherent processes and that *there are appropriate thermodynamic conditions for the formation of large clusters of hydrogen nuclei or of regions of the*

*Current address: 3498 Conrad Ave, San Diego, CA 02117, USA.

[†]Retired.

[‡]E-mail: fgordon@san.rr.com

[§]Retired.

lattice containing ordered arrays of hydrogen nuclei at high H/Pd ratios, resulting in the formation of clusters of deuterons dispersed in palladium lattice that would lead to the formation of ordered domains having high D/Pd ratios. These quotes augmented by, and derived from the thermodynamic structure of electrochemistry[2], guided the order in which the material is presented.

2.1. Chemical reaction

A chemical reaction is usually described by $aA + bB = cC + Q$, where $Q > 0$ denotes an exothermic and $Q < 0$ an endothermic reaction. This representation of a chemical reaction indicates that a mole of A react with b mole of B to yield c mole of C and d mole of D. Characteristic features of any equation, whether chemical or not, are its form and content. Here as written, only the initial and final states are not specified, i.e. the system consists of unbounded particles in the sense that there is a continuous range of possible energies. Thermodynamic considerations specify conditions for the reaction to occur.

2.2. Electron capture: a chemical reaction

In the Landau and Lifshitz treatise [3] one reads *It is not difficult to write down the thermodynamic conditions which govern the “chemical equilibrium” of the nuclear reaction, which may be symbolically written as $A_Z + e^- \rightarrow A_{Z-1} + \nu$ where A_Z denotes nucleus of atomic weight A and charge Z, e^- an electron and ν a neutrino. The neutrinos are not retained by matter and leave the body*, i.e. this nuclear reaction may be represented by equations which correspond exactly to those employed in chemical reactions.

2.3. Reaction space

Chemical reactions and/or processes do not occur in ideal conditions. Here, the reaction space, a three-dimensional entity, its location, structure and dynamics, and time when the reaction takes place, are discussed.

2.3.1. Location

One procedure to locate the reaction space for nuclear events is to electrolyze heavy water and record emission of particles. This can be done by placing a co-deposited Pd + D film on the CR-39 chip [4]. If the Pd + D film is co-deposited onto an open metallic substrate, e.g. a screen or a single wire and if the emission of particles occurs, then they are detected only along the electrode edge, as illustrated in Fig. 1. Evidently, the nuclear reaction is located very close to the contact surface. The bright line along the peripheries of a single eyelet is an overlap of hundreds of impingement tracks.

2.4. The interphase: its structure

The interphase is an element of the cathode structure where the concepts and definitions must be clearly presented and it is here, where the complex interplay involving kinetic and thermodynamic considerations must be considered.

2.4.1. Its structure

When the system is in equilibrium, its structure can be defined in terms of physical properties. When the system is not in equilibrium, then it is often convenient to discuss its structure in terms of occurring processes [2]. Moreover, in a

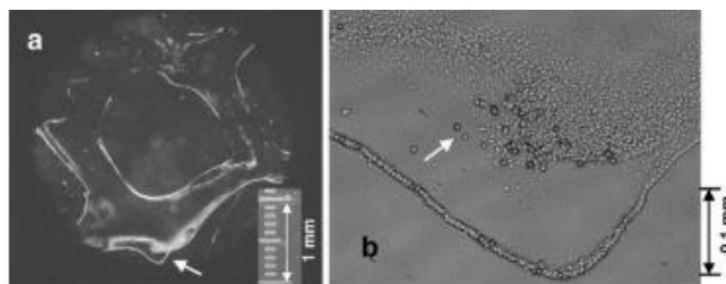


Figure 1. Emission of charged particles from a polarized Pd + D film. (a) Single eyelet, bright line consists of hundreds of impingement tracks along the edges of the screen. (b) Expanded section indicated by an arrow.

number of situations, the interphase represents a region consisting of a number of thin layers that are homogeneous and where, to assure their homogeneity, an average value of a particular variable is taken. The imposition of homogeneity on each layer results in its non-autonomous character which arises from the interaction of molecules in adjacent layers [5]. Consequently, changes in any part cause changes throughout the whole region. An abrupt change in any of the process variables will produce a relaxation spectrum with gradients associated with this variable.

2.4.2. Its dynamics

Random distribution of gas bubbles results in local changes in the charge transfer current density which, in turn, produces changes within the interphase and insures formation of localized gradients. Moreover, any motion of hydrogen within the interphase generates stresses that, in turn, produce dislocation and other types of interaction sites. How deep into the interphase they occur depends on the relaxation time of dominant processes. That it is to say, within the interphase exists a state of dynamic equilibrium which governs the distribution of hydrogen interacting with the palladium lattice which means that some interaction sites are formed, others disappear thus releasing the interacting protons and making them available for the electron capture reaction.

3. A Brief History

Shortly after the discovery of nuclear reaction in a test tube, referred to as *cold fusion*, the tendency was to explain everything including tritium production, as the result of deuteron fusion reactions. Here we present a different mechanism from that due to $d^+ + d^+$ fusion reaction (namely where the excited helium decays into t^+ and p^+) i.e. that arising from electron capture being the first step leading to tritium production which leads to a different interpretation of the observed behavior.

With the discovery of transmutation it was natural to consider a reaction path involving an electron capture by a deuteron. In September 2006, we suggested that the reaction $e^- + d^+ \rightarrow n_2 \rightarrow 2n$, plays significant role in the initiation of the F-P effect [4]^a In this paper we suggested a set of nuclear reactions, where the reactants within the reaction volume are: D^+ , and neutrons generated by the electron capture and where the reaction products are: excess enthalpy, γ -radiation and tritium, the latter being : $n + d^+ \rightarrow {}^3_1H^+ + \nu$, an analog of $e^- + p^+ \rightarrow n$.

^aIn June 2007, we submitted a manuscript "On the evidence for and origin of nuclear activities in polarized Pd/D–D₂O system" to Zeitschrift fuer physikalische Chemie. This paper was send for review on 14 June 2007 to Mr Martin Radke who advised us to check the review status with the Editor-in-Chief, Prof. Dr Baumgaertel. Our attempts to contact Prof. Baumgaertel were not successful.

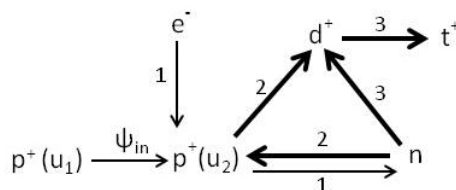


Figure 2. Flow diagram showing reactions and processes in polarized Pd/H–H₂O system exposed to an external magnetic field. ψ_m which reduces the interaction energy with $u_2 < u_1$. Arrow 1 – produces neutrons, arrow 2 – transmutes $p^+ \rightarrow d^+$, arrow 3 transmutes deuteron to triton.

3.1. Electron capture

The reluctance to accept the $e^- + d^+ \rightarrow 2n$ followed by $n + d^+ \rightarrow t^+$ reaction path for tritium production in the Pd/D–D₂O system was due to the difficulty in how to separate the electron capture reaction from other nuclear events. This difficulty could be removed if we could demonstrate the $e^- + p^+ \rightarrow n$ reaction. To test this premise, we considered an analog, viz. the polarized Pd/H–H₂O system and the $e^- + p^+ \rightarrow n$ reaction. For an electron capture reaction to occur, the proton interaction energy, $u(r)$, must satisfy the condition $\mu(n) - \mu[p^+ + u(r, \phi)] > 0$. Now, it should be possible to produce conditions that would allow the $e^- + p^+ \rightarrow n$ reaction to proceed. Indeed such conditions can be created by placing an operating cell in an external magnetostatic field (0.06T). Through the analysis for the hydrogen isotopes content in cathodes we showed the presence of all hydrogen isotopes in various ratios [6]. This can lead to only one conclusion: $e^- + p^+ \rightarrow n$ reaction did occur and started the transmutation $n + p^+ \rightarrow d^+$ and $n + d^+ \rightarrow t^+$. This set of events is illustrated in Fig. 2.

Evidently the exposure of an operating cell to an external magnetic field reduced the energy u_2 to a value so that the electron capture mechanism can start and that the forces of the proton/lattice interaction are of electronic nature [6].

4. The $n + d^+ \rightarrow t^+$ Reaction

Since all deuterons, located in the reaction volume, interact with the Pd lattice defects to a various degree, consequently their chemical potential is of the form $\mu(d^+)_l = \mu(d^+) + u(r, \phi)$. In this representation, the $u(r, \phi)$ function indicates that a part of the interacting site is incorporated into the deuteron itself, i.e. it represents the degree of overlap which,

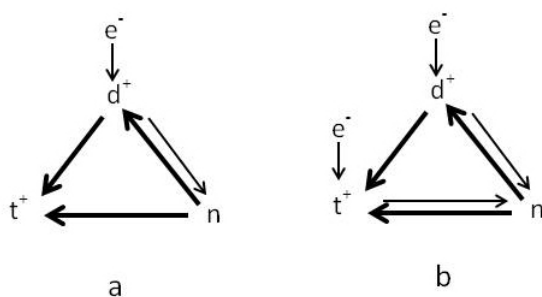


Figure 3. Reaction path generating tritium in polarized Pd/D–D₂O system. (a) Electron capture by deuteron, (b) electron capture by deuteron and triton. (3a) primary reaction, (3b) likely for for high concentration of triton is present in the reaction space.

in turn, determines whether or not the electron capture by deuteron can occur. To force the system into its nuclear active state, the quantity $\mu(n) - \mu[d^+ + u(r, \phi)]$ must be positive.

4.1. Reaction path

The path for the $n + d^+ \rightarrow t^+$ reaction is shown in Fig. 3. The starting point is the electron capture by a deuteron, $e^- + d^+ \rightarrow 2n$, a reaction that can be described by the rules of chemical kinetics. The generated neutrons interact with a deuteron to produce a triton, $n + d^+ \rightarrow t^+$, or they can react with triton to produce helium $n + t^+ \rightarrow {}^4\text{He} + e^-$. This reaction path is illustrated in Fig. 3a.

Because the value of $u(r\phi)$ function for deuteron and triton is approximately the same, it is possible that an electron can also be captured by triton yielding three neutrons, $e^- + t^+ \rightarrow 3n$. This situation, illustrated in Fig. 3b, is likely to occur when concentrations of deuterons and tritons are approximately the same. The proposed reaction path is an example of coupling of chemical processes with those governed by nuclear physics. The chemical processes take place within the confines of the interphase and change its structure which, in turn, affects their response.

5. Tritium Production and Recovery

Tracing of the tritium production and recovery of tritium in polarized Pd/D–D₂O system is illustrated in Fig. 4. It provides two sets of information. The first set shows that the interphase contains three characteristic segments, viz. reaction space and transport zone on the solid side, λ_2 and desorption of tritium from the contact surface on the solution side, λ_1 . If viewed at a given time, t_0 , then it represents the structure of the interphase by identifying the processes and assigning relevant driving forces (chemical potentials). The second set provides information on the relationship between tritium and the environment as it moves across the transport zone, crosses the contact surface and enters the λ_1 segment of the interphase.

Since the processes of production and recovery of tritium are located within the interphase, their behavior depends on and reflects the conditions arising from its dynamic equilibrium. In discussing the processes of interest are (i) the state of two variables namely electrons and deuterons while the recovery involves events occurring in the transport zone and (ii) their response to conditions imposed by the operating cell.

5.1. Tritium production

A cursory examination of Fig. 3 implies that the rate of tritium production is governed by deuteron and neutron concentrations as well as the rate constants for $n + d^+ \rightarrow t^+$ and $n + t^+ \rightarrow {}^4\text{He} + e^-$ reactions. But, the rate of neutron production depends on the rate of electron capture, i.e. on the $e_*^- + d_*^+ \rightarrow 2n$ reaction where binding energies must be specified (cf. Section 2.1). These, expressed in terms of chemical potentials, are (i) for an electron is of the form $\mu(e_*^-) = \mu(e^-) + e^-\phi$ and (ii) for deuteron of the form $\mu(df_*^+) = \mu[d^+ + u(r, \phi)]$. In addition, the electron trajectory must be such that it will collide with a deuteron.

5.2. Tritium recovery

The process of tritium recovery can be described in two ways (i) tracing its motion from the reaction space to the collection space and (ii) describing changes in the generated triton as it travels through the interphase. In the first case the generated triton, t^+ , transmutes to tritium, ${}^3\text{H}$, which enters the void, ${}^3\text{H}_v$. Since transport of tritium occurs during deuterium evolution, the state of dynamic equilibrium which governs the distribution of lattice defects/voids exists and determines the transport mode. In particular, due to localized forces associated with the dynamic equilibrium, the

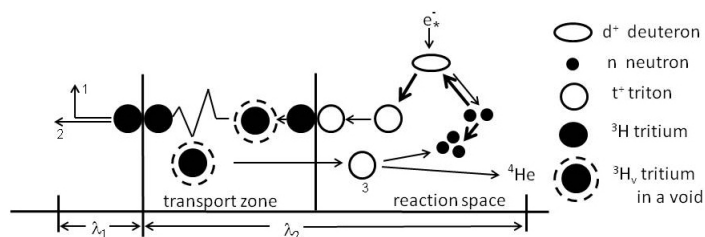


Figure 4. Schematic representation of tritium removal. Path I, line 1 to gas phase, line 2 to liquid phase. Path II, line 3 return to reaction space.

tritium transport occurs via a zig-zag path, proceeds toward the contact surface and enters the absorption layer followed by crossing the contact surface or returning to the reaction space. The empirical evidence suggests that there exists a correlation between the kinetics of deuterium evolution and the structure of the interphase which means that voids capable of retaining tritium, ^3H , are formed. This establishes the link between the kinetics of deuterium evolution and transport of tritium.

The second path is to examine possible reactions involving triton that has returned to the reaction space. The rate of tritium production is controlled by concentration of neutrons which, in turn, is controlled by the electron capture reactions ($e^- + d^+ \rightarrow 2n$ and $e^- + t^+ \rightarrow 3n$). In addition to the $n + d^+ \rightarrow t^+$ reaction, other reactions consume available neutrons. One set of possible reactions: a nucleus X having mass A transmutes to one of mass number $(A + 1)$ expressed by equation $n + {}^A X \rightarrow {}^{A+1} X$, e.g. $n + d^+ \rightarrow t^+$; $n + t^+ \rightarrow {}^4\text{He}$; etc. There are yet other possible reactions that consume neutrons.

The processes illustrated in Fig. 4. show clearly the difference between tritium which is detected and that which is generated. This difference arises from and is affected by the coherent processes occurring within the transport zone and reaction space. It is this coherence that leads to the observed sporadic production of tritium.

6. Conclusions

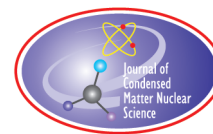
The proposed model and the presented empirical evidence leads to the following conclusions.

- (1) Nuclear reaction in condensed matter require establishment of a nuclear active state.
- (2) Direct evidence (cf. [6]): The electron capture by a proton starts the set of nuclear reactions via neutron production. Because the binding energy of d^+ is less than for the p^+ specie, there is no need to apply an external magnetic field for the electron capture reaction to occur because the Pd/D–D₂O system is all ready in its nuclear active state where the reaction steps are identical.
- (3) It is necessary to differentiate between what is produced and what is measured. The usually reported rate of tritium generation refers to tritium transported across the interphase region only (transport zone, cf. Fig. 4). If the term sporadic production implies that there are periods of no production, then the proposed mechanism is questionable. But this model accounts well for periods of increased tritium production.

References

- [1] M. Fleischmann, S. Pons and G. Preparata, *Il Nuovo Cimento* **107 A** (1994) 143.
- [2] P. van Rysselberghe, in *Modern Aspects of Electrochemistry*, Vol. IV, Plenum Press, 1966.
- [3] L.D. Landau and E.M. Lifshitz, *Statistical Physics*, Vol. 5, Part 1, Pergamon, Oxford, pp. 318–319.
- [4] S. Szpak, P.A. Mosier-Boss and F.E. Gordon, *Naturwissenschaften* **94** (2007) 511.

- [5] R. Defay and I. Prigogine, *Surface Tension and Absorption*, Longmans, London, 1966.
- [6] S. Szpak and J. Dea, *J. Condensed Matter Nucl. Sci.* **9** (2012) 21.



Research Article

The Pd + D Co-Deposition: Process, Product, Performance

Stanislaw Szpak^{*,†}

SPAWAR Center San Diego, CA, USA

Abstract

The preparation of electrodes by a co-deposition is discussed in detail. The electrode reactions are identified, the structural features of the deposit are described and the relevant experimental evidence is assembled.

© 2014 ISCMNS. All rights reserved. ISSN 2227-3123

Keywords: Co-deposition

1. Introduction

Recently, I learned that Letts and Hagelstein [1] modified the Szpak protocol to assure a 100% reproducibility in excess heat production. Upon repeated reading, I concluded that I should respond because not all pertinent and available information was used. In their paper, there is the sentence ... *an issue in the Szpak experiment is reflected in the literature in the relative absence of replications showing excess heat due to insufficient loading and poor adhesion.* But, in a publication [2], we discussed the deuterium uptake in detail and have shown that the deuterium loading exceeds 100%. In this communication I present a very different discussion of the Pd + D co-deposition process.

My involvement in the research of the F–P effect dates back to May 1989 when I proposed a variant of the usually employed massive electrodes, viz working electrodes prepared by the Pd + D co-deposition, a process in which the Pd^{2+} and D^+ ions are electrodeposited onto a substrate which does not absorb deuterium, e.g. Cu, Au, Pt, etc. One obvious reason was to eliminate the charging time. The other, more interesting, was to study the processes that initiate nuclear activity in the polarized Pd/D–D₂O system.

In 1989, not much was known about the Pd + D co-deposition. The development and evaluation of an experimental procedure is not instantaneous. It requires the determination of conditions that maximize its usefulness. In the SPAWAR laboratory we carried out collateral research involving (i) deuterium absorption during co-deposition [2] as well as the electrochemical charging of solid palladium [3,4], (ii) response to change in cathodic over-potential during co-deposition and on solid palladium [5]. We examined the thermal behavior of cells using cathodes prepared by co-deposition using a model which differs from that presented in [1].

^{*}Current address: 3498 Conrad Ave, San Diego, CA 02117, USA. E-mail: stan.szpak@gmail.com

[†]Retired.

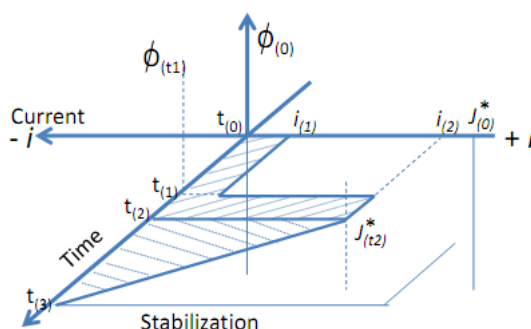


Figure 1. Schematic representation of the co-deposition process.

2. Process

2.1. Kinetics of electrode reactions

2.2. The art of Pd + D co-deposition

In practice, the cell current is much smaller than the diffusion limiting current, $I_1 < j_{\text{lim}}$. Note that in Fig. 1, j^* denotes the limiting current. This is done to assure an adherent Pd deposit. With the passage of time, the Pd^{2+} ions are depleted, the electrode potential, driven by the cell current, becomes more negative. At $t = t_1$ the cell current is increased to I_2 , i.e. to a value very close to the limiting current. This is done to assure a long co-deposition period. When the applied current, I_2 , by reducing the concentration of Pd^{2+} ions, becomes the diffusion limiting current (for that concentration) the electrode potential is driven into the region of heavy water instability and at $t = t_2$, the reduction of D^+ ions commences and the co-deposition begins. If the co-deposition is galvanostatically controlled and if the cell current exceeds the diffusion limiting current, then, at constant volume and surface area, the Pd^{2+} ions concentration decreases linearly with time. The co-deposition is completed at $t = t_3$.

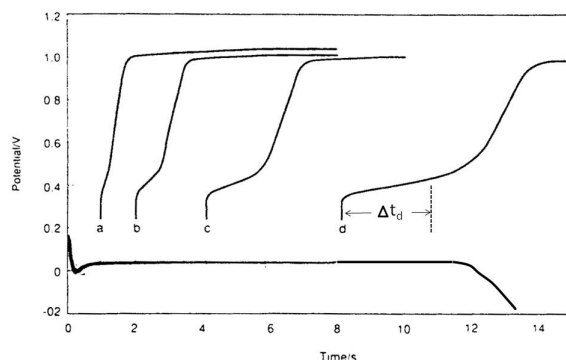


Figure 2. Deuterium up-take during co-deposition. $j_c = -5 \text{ mA cm}^{-2}$ and $j_a = 5 \text{ mA cm}^{-2}$, with cell current reversal at 1, 2, 4 and 8 s.

2.3. Corollary

- (1) The Pd + D co-deposition process does not specify (i) the electrolyte concentration except to say that (a) the reduction of Pd^{2+} ions is diffusion controlled^a, (b) ratio D/Pd reduction determines morphology of the deposit and (c) substrate preparation prior to co-deposition is a crucial component of the process.
- (2) Deuterium up-take during co-deposition at constant cell current can be determined from the cathodic and anodic potential/time relationships shown in Fig. 2. The line parallel to the time axis represents potential/time during the co-deposition of the Pd/D film whose composition at a given time depends on how much charge was consumed by Pd^{2+} ions, $Q_{C,1}$ and how much for hydrogen generation, $Q_{C,2}$ which for the atomic ratio D/Pd = 1 is 2. Upon switching from cathodic to anodic current, the potential/time curve identifies the following processes: changes in the double layer, desorption and oxidation of deuterium and oxygen evolution.

The atomic ratio D/Pd in is obtained from the ratio $\Delta t_n / \Delta t$ where the subscript $n = a, b, c, d$, identifies the potential/time curve and Δt is the time needed to obtain the atomic ratio D/Pd = 1 at the time of current reversal. The deuterium up-take, expressed as a D/Pd atomic ratio, taken at 1, 2, 4 and 8 seconds of charging are 0.95, 1.07, 1.1 and 1.3.

- (3) In the co-deposited Pd/D film the D/Pd = 1.0 atomic ratio is obtained immediately in agreement with and support of thermal data, cf. Fig. 6.

3. Product

The product quality is judged by its performance which, in turn, imposes demands on its construction and/or function. Here, the Pd/D cathodes serve as a seat for heat generation that is nuclear in origin. In practice, one has to answer the following: (i) what is its stability at high cell currents as well as when subjected to highly energetic nuclear reactions, (ii) what is the optimum thickness of the deposit to assure maximum excess heat. The research done in the SPAWAR laboratory indicates that to answer it is necessary to consider (i) the structure of the deposit and its stability, (ii) the interphasse and (iii) the act of absorption.

^aThe composition 0.03 M PdCl_2 , 0.3 M LiCl in D_2O was found to be satisfactory.

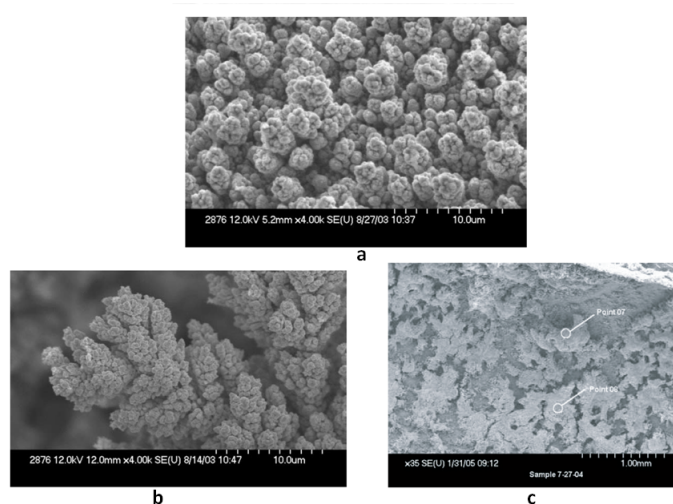


Figure 3. SEM of co-deposited Pd/D film. (a) After completion of co-deposition, (b) exposed to an external electric field, and (c) exposed to magnetic field.

3.1. Structure: Effect of external fields

The structure of the co-deposited Pd/D film from a solution containing PdCl_4^{2-} is shown in Fig. 3. In particular, Fig. 3a is the SEM of the deposit after completion of co-deposition. Its structure did not change when used as a cathode at current densities up to 400 mA cm^{-2} . When the cell was placed in an external electric and magnetic field, its structure has changed as shown in Fig. 3b for an electric field and in Fig. 3c in the magnetic field.

- (1) Figure 3b is the SEM of the Pd/D cathode shortly after placing the cell in an external electric field which results in swelling and alignment with the field. The initial porous cauliflower-like structure has changed to a columnar arrangement of globules.
- (2) The placement of an operating cell in magnetic field changed the globules into pancake-like entities that appear to be firmly affixed to the substrate.

3.2. The interphase

The interphase, $\lambda = \lambda_1 + \lambda_2(\tau)$, is a region separating two homogeneous phases. When the system is in equilibrium, its structure can be defined in terms of physical properties. When the system is not in equilibrium, it is often convenient to discuss its structure in terms of occurring processes, i.e. the interphase can be viewed as an assembly of a set of homogeneous layers whose structure is determined by the operating processes and their relaxation times. To assure their homogeneity, an average value of a particular variable is taken [8]. The imposition of homogeneity of each layer results in its non-autonomous character which arises from the interaction of molecules in adjacent layers. Consequently, changes in any part cause changes throughout the whole region.

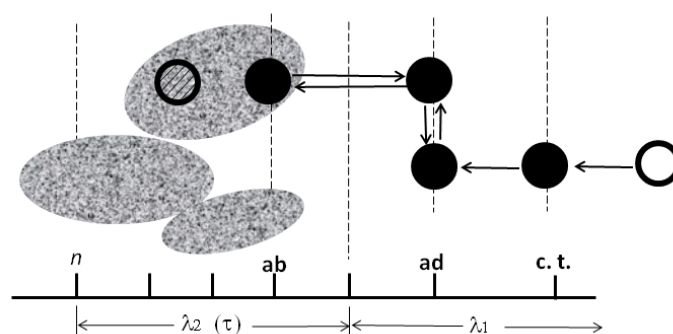


Figure 4. Deuterium crossing the interphase region. (open circle) D^+ ion, (black circle) deuterium atom, (shaded circle) deuteron, ct–charge transfer layer, ab–absorption layer, shaded areas– domains.

3.3. Crossing the interphase

Transport of deuterium across the interphase is due to coupling processes at the contact surface followed by transport into the electrode interior, with the concentration of deuterium being larger in the $\lambda_2(\tau)$ segment of the interphase [4]. The solvated D^+ ions are driven toward the negative electrode at the rate determined by the cell current. The electro-deposited deuterium is removed from the contact surface by gas evolution and by absorption. The adsorbed/absorbed deuterium is distributed as follows: (i) The subsurface, D_s is formed just below the topmost layer of Pd atoms and provides the link between the chemisorbed surface atoms, D_a , and the dissolved in metal, D_m , (ii) two energetically different D_a exist, (iii) with chemisorption there is associated surface reconstruction, but only D_s is responsible for its maintenance, (iv) there is an energy barrier separating D_a and D_s which affects transport in both directions. Chemisorbed D_s is responsible for surface reconstruction while absorbed D_s maintain state of reconstruction [9].

3.4. Corollary

- (1) Any solid undergoes shape change when the internal forces exceed the elastic limits. In general, three types of forces can be identified as acting during the deformation of a solid. These are (i) internal forces, i.e. forces that obey Newton's law, (ii) applied external forces and (iii) capillary forces (forces that act between the internal and surface molecules, or between solid boundary and the molecules of surrounding liquid). By definition, when the surface forces are not uniformly distributed, they act as external forces. If, in fact, the latter are involved in producing shape changes, Fig. 3, then their action can be magnified by an external electrostatic and/or magnetostatic fields. The relationship between surface forces and the bulk response is given by the Gauss theorem which states that forces acting on any finite body can be reduced to forces applied to the surface and vice versa. It follows that the shape change at constant volume is the result of motion due to forces acting on the surface. Consequently, the deformation is determined by the distribution of surface forces while the rate of deformation, by their magnitude.
- (2) The structure of the interphase controls its performance via (a) generation of lattice defects through activities in the λ_1 segment, (e.g. gas bubbling and the associated charge transfer current density), (b) porosity which affects the distribution of the primary charge transfer current density and which determines the useful thickness of the Pd/D deposit.

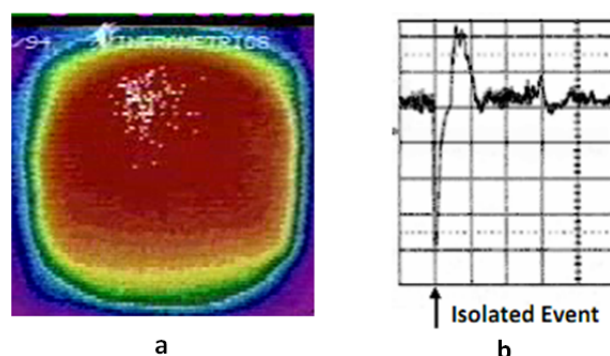


Figure 5. Thermal and mechanical effects. (a) Hot spots and (b) piezoelectric sensor response to a hot spot.

4. Performance

The large quantities of excess enthalpy generation in the Pd/D–D₂O system raised questions: (i) Is the excess enthalpy generation reproducible? (ii) Is the heat source uniform throughout the whole electrode volume or distributed? Experience shows that, if correctly applied, electrodes prepared by the Pd + D co-deposition provide answers: yes to (i) and the discussion based on experimental evidence to (ii).

To confirm the existence of the F–P effect one needs only to establish an excess enthalpy production by calorimetry. But calorimetry, being an integrating procedure, cannot do much more. There are other tools that can add to a better understanding the nature of the polarized Pd/D–D₂O system. One such tool is the infrared (IR) imaging of the surface of an active electrode [10]. The other, prompted by the first, is the use of a pressure sensitive substrate, onto which the Pd/D films are co-deposited, to demonstrate mechanical changes that do occur when an instantaneous and high intensity exothermic reaction takes place [11]. This communication includes a brief discussion of the thermal behavior immediately after beginning of a run.

4.1. Infrared imaging and pressure and temperature wave

Figure. 5a shows the IR image of the cathode and Fig. 5b the associate pressure and temperature waves. The IR imaging shows discrete reaction sites randomly distributed in time and space. The short lived hot spots resemble mini-explosions which, in turn, generate pressure and temperature waves recorded by the piezoelectric sensor. As the solution temperature raises, the hot spots become brighter and an amplified sensor response.

4.2. Initial thermal behavior

The co-deposition starts with endothermic absorption of deuterium. However, within seconds, the endothermic absorption is balanced by an exothermic nuclear reaction, Fig.6, point a. The balance involving endothermic and exothermic process ends at point b.

4.3. Corollary

- (1) Existence of domains containing clusters of deuterons or of regions of ordered deuterons dispersed in the Pd lattice that lead to the formation of ordered domains having high D/Pd atomic ratio.

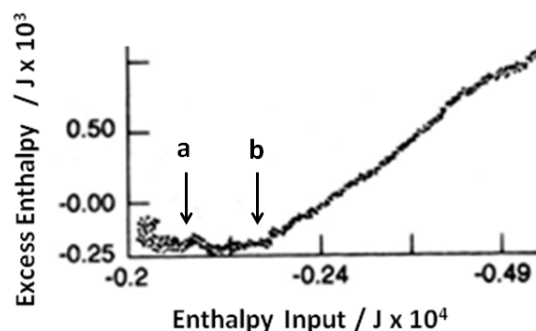


Figure 6. Initial thermal behavior: endothermic absorption – $0 < Q < A$, endothermic absorption balanced by exothermic reaction – $a < Q < b$, exothermic reaction dominates $Q > a$.

- (2) The heat source arises from fast chain of nuclear reactions or from a kind of cluster collapse.
- (3) The size of the cluster or the rate constant of the chain reaction are temperature dependent

5. Conclusion

The Pd + D co-deposition produces not only effective cathodes but also provides an insight into the conditions that give rise to, and are associated with, the nuclear events that occur within the confines of the Pd lattice. A complete description must include (i) the processes and/or reactions involved, (ii) product and its function and (iii) the performance that determines its effectiveness. In concluding remarks I will address the (i) kinetic aspects very near the starting of co-deposition and (ii) the similarities and differences between the co-deposition described in this communication and that in [1].

5.1. Kinetic aspects at the start of co-deposition

Within seconds after starting co-deposition a series of events takes place. The first set is the accumulation of absorbed deuterium around the lattice defects, cf. Section 2.1, forming ordered clusters of deuterons dispersed in the Pd lattice. Their size can be estimated by examining the hot spots, cf. Fig. 4a. Using this approach Chubb [12] suggested 10^4 – 10^9 events occurring within a volume having a diameter of 100 Å.

The question, what is happening during the time separating complete saturation and onset of nuclear reaction, needed an answer. Fleischmann et al. [13] suggested that... *there are appropriate thermodynamic conditions for the formation of large clusters....* This statement can be extended to include self-organization which implies that there exists a volume element within the system having dimensions much larger than the characteristic molecular dimensions but smaller than the total volume of the system [14]. Within this volume fluctuations behave coherently thus modifying its microscopic behavior. At far from equilibrium, new structures, involving coherent behavior are formed and can be maintained only through a sufficient flow of energy [15]

Thermodynamic arguments imply that energy flow external to the clusters may affect their behavior. Indeed, as the solution temperature rises from 30 to 80°C, the hot spots are brighter and the mini-explosions stronger [11]. Since within this temperature range nuclear reaction rates are not affected, it means that either rate constant of the chain reaction increased or the cluster became larger. As a general proposition – a complex interplay of kinetic and thermodynamic quantities create conditions that allow the nuclear event to occur

5.2. The Letts–Hagelstein (L–H) protocol – a variant of co-deposition

The comparison of the co-deposition described in [1] and that presented in this communication can be best accomplished by the discussion of (i) process, (ii) product and (iii) performance.

(i) Process. Difference in (a) electrolyte composition, viz added H^+ ions, less $PdCl_2$, (b) in processing, e.g. co-deposition at 600 mA cm^{-2} results in very different kinetics of co-deposition. **(ii) Product.** The L–H protocol specifies the structure of the cathode, i.e. it requires the deposition of gold film prior to Pd + D co-deposition. **(iii) Performance.** Reproducible production of excess enthalpy.

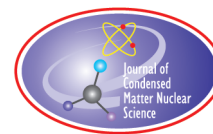
If to *modify* means to introduce minor changes in either electrode preparation or cell operation, then based on information presented in [1] the L–H protocol is a new procedure rather than modification of another one. It does not matter how to call it. What matters is that cells using cathodes prepared by the L–H protocol can be operated at much higher current densities.

Acknowledgment

The experimental protocol developed in the SRAWAR laboratory yielded immediate and reproducible results in support of the Fleischmann–Pons claims. The results (excess enthalpy and tritium production) were presented to Dr Gordon who concluded that we have a new tool to investigate the nature of nuclear events occurring in the Pd/D–D₂O system. With his support, I and my Colleagues, were able to study, in addition to thermal behavior, electromagnetic radiation, transmutation and particle emission. This work could not have been done without the help and support of Dr Frank E Gordon, at that time a member of the US Navy Senior Executive Service.

References

- [1] D. Letts and P. Hagelstein, *J. Condensed Matter Nuc. Sci.* **6** (2012) 44.
- [2] S. Szpak, P.A. Mosier-Boss and J.J. Smith, *J. Electroanal. Chem.* **379** (1994) 121.
- [3] S. Szpak, C.J. Gabriel, J.J. Smith and R.J. Nowak, *J. Electroanal. Chem.* **309** (1991) 273.
- [4] S. Szpak, P.A. Mosier-Boss, S.R. Scharber and J.J. Smith, *J. Electroanal. Chem.* **380** (1995) 1.
- [5] S. Szpak, P.A. Mosier-Boss, S.R.E. Scharber and J.J. Smith, *J. Electroanal. Chem.* **337** (1992) 147.
- [6] H. Naohara, S. Ye and K. Uosaki, *J. Phys. Chem. B* **102** (1998) 4366.
- [7] T. Ohmori, K. Sohamaki, K. Hashimoto and A. Fujishima, *Chem. Lett.* 1991, p. 93, The Chemical Society of Japan.
- [8] R. Defay and I. Prigogine, *Surface Tension and Absorption*, Longmans, London, 1966.
- [9] J. Behm, *J. Chem. Phys.* **78** (1983) 7486.
- [10] P.A. Mosier-Boss, *Il Nuovo Cimento* **112** (1999) 517.
- [11] S. Szpak and F. Gordon, *J. Condensed Matter Nucl. Sci.* **12** (2013) 143.
- [12] S.R.E. Chubb, Private communication, 1994.
- [13] M. Fleischmann, S. Pons and F. Preparata, *Il Nuovo Cimento* **187A** (1994) 143.
- [14] G. Nicolis, *Self-organization in Non-equilibrium Systems*, Wiley, Toronto, 1976.
- [15] P. Glansdorff and I. Prigogine, *Thermodynamic Theory of Structure, Stability and Fluctuations*, Wiley Inter Science, London, 1971.



Research Article

Cathode to Electrolyte Transfer of Energy Generated in the Fleischmann–Pons Experiment

S. Szpak and F. Gordon*

3498 Conrad Ave., San Diego, Ca 92117, USA

Abstract

In our recent paper [1] we asked: why an exothermic system with the positive feedback, such as the Fleischmann–Pons experiment, does not suffer thermal run-a-way. In seeking an answer we selected two items (i) formation of hot spots and (ii) system's response following a fast nuclear event, that seem to point to a simple model of cathode to electrolyte energy transfer.

© 2014 ISCMNS. All rights reserved. ISSN 2227-3123

Keywords: Cold fusion, Electrolysis, Hot spots

1. Development of the Model

Reactions and processes associated with the selected items are discussed in [1]. Here, a brief description of relevant conclusions derived from (a) hot spots and (b) system' response forms the basis for the proposed model of heat transfer path.

2. Cathode to Solution Heat Transfer Path

Prior to the mini-explosion the system is in its pre-nuclear active state. A large number of deuterons and electrons is contained within a volume having radius of a few hundreds Angstroms, symbolically illustrated in Fig. 1 c₁. At a certain time the fast nuclear reaction, resembling a mini-explosion, occurs, point A, causing local lattice destruction followed by forcing the hot reaction products into the solution, Fig. 1 c₂.

3. Comments

Experience shows that the polarized Pd/D–D₂O system typically maintains a temperature difference of a few degrees C above the solution. This is unexpected behavior for a positive feedback system unless (i) the heat is generated at

*E-mail: fgordon@san.rr.com

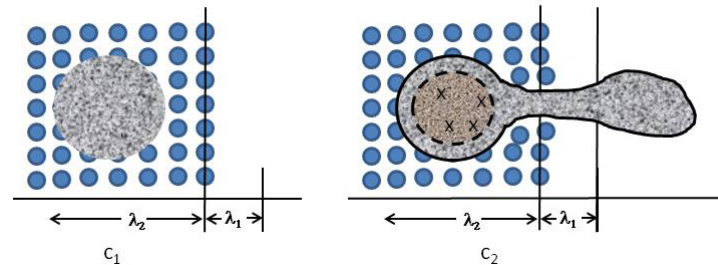


Figure 1.

surface or (ii) very close to the surface and hot reaction products can penetrate the interphase. There is no evidence for (i) and limited information for (ii).

A domain, containing large number of reactants (deuterons and electrons), in its pre-nuclear active state is shown symbolically in Fig. 1 c_1 where it undergoes fast nuclear reaction (reaction time: a few nanoseconds). One possible explanation is that the reactions produce a very fast increase in pressure (e.g. a mini explosion) that “opens up” a pathway for the reaction product (probably helium) to escape before substantial damage of the lattice occurs due to the heat of reaction. The explosive event causes (i) an increase in volume, (ii) lattice expansion/destruction at the interphase and (iii) transfer of hot reaction products to the solution phase, Fig. 1 c_2 . That it is to say that practically all energy generated is transferred to the solution. The heat stored at periphery of the expanded reaction volume is insignificant.

The system returns to its normal state within a fraction of a second ($\Delta t = 0.6$ s, Figs. 1 and 2 (b_1 and C_2)). The endothermic heat of deuterium absorption off-sets the residual heat stored in the periphery so that the cathode temperature remains constant.

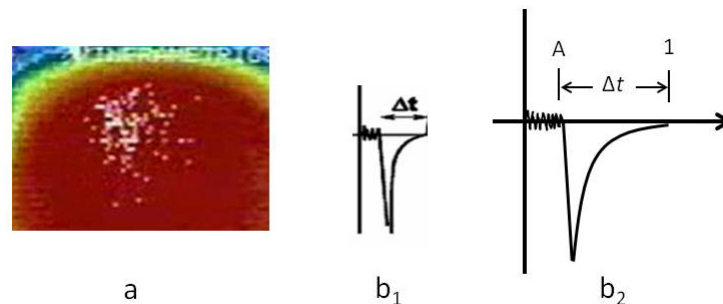
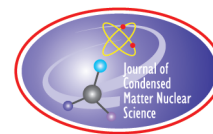


Figure 2. (a) The infra-red imaging of the cathode, prepared by co-deposition, of an operating cell reveals the presence of randomly distributed in time and space hot spots. These discrete heat sources are located in the close proximity to the contact surface, Fig. a. Information derived from hot spots is as follows: (i) formation of domains having the volume corresponding to the radius of a few hundred Angstroms, in which 10^9 fast reactions occur [2], (ii) the energy released is on the order of 0.1 kJ/g and must have been occurred on at time scale of less than 10 ns [3]. (b) System's response to the nuclear reaction recorded by a piezo-electric sensor, b_1 is that due to explosion. An extended view, Fig. b_2 , shows: point 1 - system at rest. Point A - explosion, time period Δt system relaxes to its initial state. .

References

- [1] S. Szpak and F. Gordon, *J. Cond. Mat. Nucl. Sci.* **12** (2013) 148–162.
- [2] S.R. Chubb, Private communication, 1984.
- [3] L. Wood, Private communication, 17 October 2000.



Research Article

Sonofusion: Ultrasound-Activated He Production in Circulating D₂O

Roger S. Stringham*

PO Box 1230, Kilauea, HI 96754, USA

Abstract

Experiments over the last 25 years have demonstrated *sonofusion*: the formation of He by ultrasound incident on D₂O. The observed effect is described. Neither the characteristic gamma nor the neutron typically seen in the formation from two deuterons of ⁴He and ³He, respectively, is observed. The experimental arrangement is specified. A proposed model, based on cavitation-produced z-pinch jets in target-foil implants, is outlined. It involves formation in the implants of a BE condensate that provides the source of the deuterons and whose recoil ensures energy-momentum conservation. The model accounts for all experimental results. It also provides a guide for future work on sonofusion.

© 2014 ISCMNS. All rights reserved. ISSN 2227-3123

Keywords: Alpha, Bremsstrahlung, Gamma, Heatk, Sonoluminescence

1. Introduction

A summary is presented of over 25 years of the author's experimental results on the formation of ⁴He initiated by a high-frequency acoustic wave incident on circulating D₂O in the presence of an exposed Pd, Ti or other lattice. ⁴He analysis was also carried out in part by others [1–3], as summarized in the Appendix.

The observed effect is described in Section 2. The emitted heat correlates with the energy released in the counted number of 2D events. The process – termed *sonofusion* – produces, for each observed ⁴He atom, excess heat slightly greater than the binding energy B (2D, ⁴He). Most applications of calorimetry to fusion have been based on electrochemistry [4–7], not on ultrasound. In both the ultrasound-generated and electrochemically generated calorimetry-based measurements, both ⁴He and ³He production were observed. Neither the characteristic 23.8 Mev gamma nor the 2.45 Mev neutron typically seen in $2^2\text{H} \rightarrow ^4\text{He} + \gamma$ and $2^2\text{H} \rightarrow ^3\text{He} + \text{n}$, respectively, has been observed in the ultrasound or electrochemical systems [3,8,9]. No gammas were found during sonofusion experiments when measured with GM and BF₃ detectors [8,9] and no ³He was found in Pd target foil runs [3]. There was T detected via MS of a growing presence of ³He over time from gases collected from Ti target foil runs [3].

The circulating D₂O system, comprising six major subsystems, is specified in Section 3.

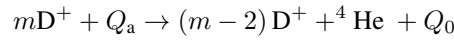
A theoretical model for sonofusion is outlined in Section 4. It accounts for the process as a whole, including the absent gamma and neutron. The model is based on diverse experimental results [3,10,11]. It comprises the formation,

*E-mail: firstgate@earthlink.net

by acoustic-driven cavitation, of bubbles that form a plasma containing deuterons and electrons. The plasma is compressed by a pinching magnetic field (Z-pinch), causing a sequence of picosecond sub-nanometer events consequent to implantation of D^+ ions in the lattice. The fusion occurs in a BE condensate formed in the lattice implantation. The single events are shown in a $1 \mu m^2$ FE SEM photo [12]. Sonofusion differs from *bubble fusion*, which relies on neutrons producing fusion events *within the confines* of a cavitation bubble [13]. The model should provide a guide for future work, both experimental and theoretical, on sonofusion.

2. Observed Effect

An ultrasound pulse of energy Q_a , incident on a room-temperature system of circulating liquid D_2O , has been observed to produce 4He and energy in the form of calorimetrically measured heat, Q_0 ,



the number, m , of deuterons in the interacting cluster can range from about 100 to 2. The *excess* heat, Q_x , produced by the reaction is then

$$Q_x = Q_0 - Q_a$$

The numerical values of (Q_a, Q_0, Q_x) given below will be those (delivered, measured, calculated) in one second [11].

The frequency of the acoustic wave is about 1 MHz; the pulse is on for about 120 s, then off for about 120 s. The temperature of the system reaches 90% of its steady-state value of about $15^\circ C$ higher than the start temperature within about 60 s.

A single *cycle* of the ultrasound wave was found to produce about 10^7 events (an event is the production of a single 4He atom [12]), observed spectra of sonoluminescent and bremsstrahlung photons, and measured heat in the amount $Q_0 = 58$ J for an acoustic energy $Q_a = 15$ J, so that $Q_x = 43$ J. This translates into 10^{13} events/s and determined excess heat per event of $q_x = 4.3 \times 10^{-12}$ J = 26.9 MeV. The energy of an event is independent of the size of the number m of deuterons in the cluster. It is about 3 MeV higher than the binding energy of 4He in terms of deuterons (the D_2O disassociation energy of 15.5 eV is neglected), which is related to the listed binding energies based on nucleons:

$$B(2D; ^4He) = B(2p, 2n; ^4He) - 2B(p, n; D) = 28.3 - 2 \times 2.22 = 23.9 \text{ MeV}.$$

The helium atoms were detected and counted by a mass spectrograph by B. Oliver [3,14]

3. Circulating D_2O System

The circulating D_2O system comprises six major subsystems, as shown in Fig. 1. The subsystems are next listed in the sequence in which D_2O circulates through them.

(1) A *bubbler* containing argon-saturated D_2O , with argon gas above the saturated liquid. The initial concentration of 4He in the Ar, prior to circulation through the system, was measured in a mass spectrograph (see (7), below) at less than 2 ppm. The bubbler maintains constant pressure throughout the system; after the fluid has passed through the system, it also transfers any bubbles that have been formed from the liquid into the argon gas, separates the argon gas from the liquid D_2O , and collects about half the total 4He produced; see (4) below. Calorimetric flow was determined through heat measurements in a system that used 1.6 MHz resonators. In another system, using a Mark I 20 kHz resonator, the amount of 4He in the gases over the circulating D_2O was measured to be 551 ± 1 ppm.

(2) An *FMI pump*, which pumps the circulating Ar/ D_2O fluid and establishes a constant D_2O mass-flow rate.

(3) A *filter*, which eliminates any small particles.

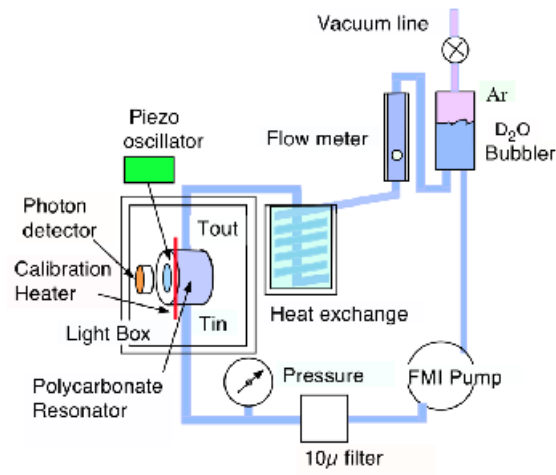


Figure 1. Typical D₂O Flow System.

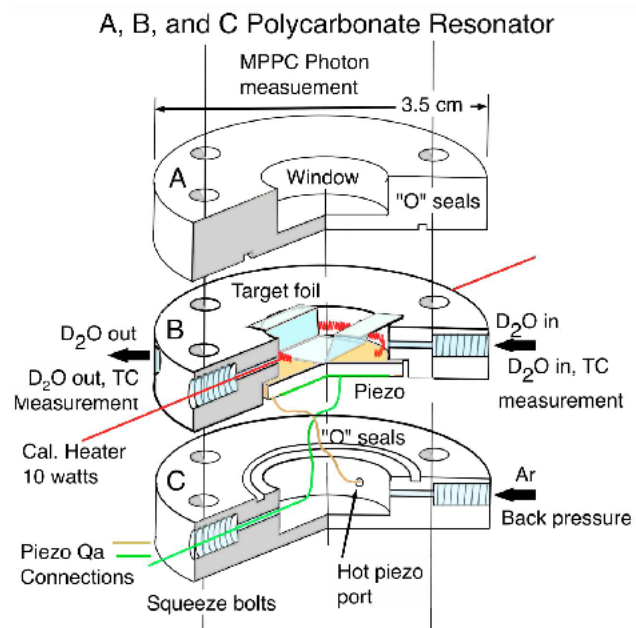


Figure 2. Typical resonator; see (4).

(4) A *light box* that contains a foil (target lattice), typically Pd, Ti or another material; a MHz piezo resonator; and thermocouples that measure the change in the D_2O temperature, $\Delta T = T_{out} - T_{in}$. The resonator produces a calibrated ultrasound pulse of magnitude Q_a , with a 120 s on/off mode; Q_a can be adjusted to deliver from 0 to 15J in 1 s. A typical resonator is shown in Fig. 2. The MHz ultrasound pulse creates cavitation bubbles in the circulating D_2O . The number of deuterons in a bubble is estimated reliably using the ideal-gas law for the collected portion of the total 4He produced and the measured pressure and temperature. Each bubble grows and gains mass in the negative pressure of the acoustic input; at a maximum radius it collapses adiabatically to a final radius with a million-fold increase in energy density. 10^6 bubbles, each producing 10^3 photons, are counted by a multipixel photon counter (MPPC). The measured photon emission, shown in Fig. 3, includes two types of photon radiation: sonoluminescent and bremsstrahlung. The observed spectrum shows a single sharp peak of about 100 ns duration for each cycle [15].

(5) A *heat exchanger*, a heat sink that brings the temperature back to its initial base value.

(6) A *flow meter* that measures the flow rate, which together with ΔT determines the heat output Q_0 . The excess heat produced by the reaction is determined from the delivered Q_a and mass-flow calorimetrically measured Q_0 by Eq. (2).

(7) A mass spectrograph (MS, not shown in Fig. 1) that measures the helium atoms in ppm concentration in the argon gas. A measured aliquot – known volume of gas at measured pressure and temperature – was transferred into the MS and compared to a known ppm standard. The number N of experimentally produced alphas was determined from $pV = NkT$.

4. Theoretical Model

The author has proposed a theoretical model to account for his 25-year collection of experimental results – with differing resonator sizes, frequencies, and acoustic inputs. The model involves a multi-stage process for the fusion of two deuterons into an alpha particle [9-2,14,15]. The discussion is carried through for 4He , but it applies to $T \rightarrow ^3He$ as well [10].

(A) The ultrasound pulse ionizes some of the D_2O and, in the first stage of a compression process, creates a population of transient cavitation bubbles with a wide spectrum of sizes. Bubbles whose size is in resonance with the

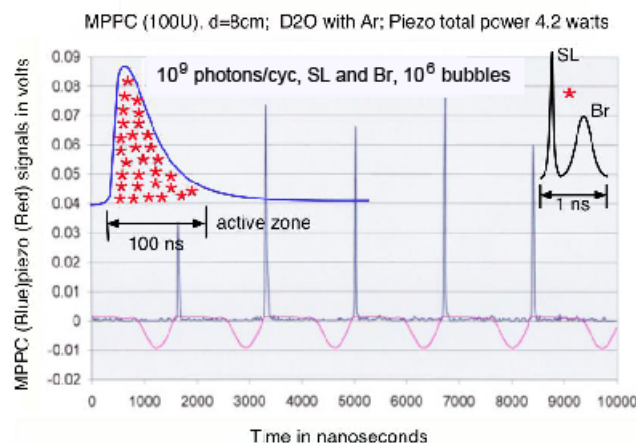


Figure 3. Measured photon spectrum, showing a single sharp peak of about 100 ns duration for each cycle. There is no activity in the region between peaks. Upper right shows the expected photon emission, which was not resolved experimentally, from one out of 10^6 bubbles/cycle.

acoustic wavelength grow in size and gain energy isothermally by picking up additional mass – deuterons and sheath electrons – from the D_2O and Ar [14], then collapse adiabatically in a few nanoseconds. The collapsing bubbles emit the observed sonoluminescent and bremsstrahlung photons. This sequence of events occurs on a time scale which is a tiny fraction of the time of a single ultrasound cycle, and millions of bubbles per cycle satisfy the resonance criterion for such pressure-driven growth in mass followed by its adiabatic collapse/emission. The supersonic collapse of sonoluminescent bubbles and photon emission on such a short time scale is itself a known phenomenon [16]. The collapsing bubbles also form a neutral plasma jet containing deuterons and sheath electrons.

(B) The jet is compressed further by a pinching magnetic field, produced by the jet's sheath electrons (Z-pinch), along the axis of the jet's motion [17].

(C) The compressed jet becomes implanted in the target foil, itself a two-stage process. The deuterons implant in the lattice inside the electron cloud. The free electrons accelerate towards and compress the less mobile deuterons. The oxygen and argon ions remain free of the lattice because O^- and Ar^+ are about 10^4 larger than the D^+ , but the geometry of the jet is such that it is sufficiently close to the target foil for them to combine with the lattice material. The oxygen has been detected in the systems as thin oxide films, which were measured by EDS methods [10].

(D) To account for the absence of both a neutron and a gamma in the fusion process, the model postulates the formation, in the implanted deuteron cluster and electrons, of a system comprising two concentric components: a transient BE condensate M of deuterons and possibly another of Cooper pairs of electrons, with the latter on the outside. The number of deuterons in M can vary from 100 to 2. In the limiting case of 2, sonofusion corresponds to muon fusion. The Lawson criterion, L_c , for fusion to occur can therefore be approximated by that for muon fusion, for which it is $L_c > 10^{16}$ s/cm³. In its simplest form the Lawson parameter is given by $L_c = n_D t_E$, where n_D is the deuteron density and t_E is the deuteron contact time. For sonofusion we have $t_E \sim 10^{-14}$ s, so the deuteron density has to satisfy $n_D > 10^{30}$ cm³. At present there is no independent determination of n_D . The physical makeup of the two connected charged components results in two special conditions: (1) the M deuterons, with the condensate property of behaving as a single state in momentum space, will compress to astrophysical densities of picoseconds duration, with particle separation less than an Angstrom, whereas a group of individual charged particles, fermions or bosons, would resist this compression to the M center [18]; and (2) permittivities of the two charged components across their interface that have a ratio of 1000 due to the large difference in deuteron and electron mobilities. These two conditions work in tandem, along with the electric fields of the free-electron cloud surrounding M, to compress M.

(E) With increasing compression, the density becomes high enough for the M condensate to break up into a debris M' of D^+ ions, containing two fewer D^+ ions than the condensate M, and an alpha,



Recoil is taken up by the D^+ ions in M'.

The fusion releases heat in the amount $B(2D; {}^4He)$ via bremsstrahlung; see Fig. 3.

(F) The heat released by the fusion of the deuterons vaporizes the region of the foil in which they are implanted, leaving a hemispherical heat footprint in the range of the binding energy and size of 50 nm and craters shown in Fig. 4. The transition (4a), with an initial temperature of 10^7 K, initiates a heat pulse in the lattice from a lattice depth of about 25 nm. The locations on the foil where the fusion events occur are termed *ejecta sites*. The site expands by 25 nm to the lattice surface as a radial heat pulse, ejecting 10^4 Pd lattice atoms; an FE SEM photo of surveyed sites [12] is shown in Fig. 4.

The temperature of the event is on the order of 10^4 – 10^5 K at the surface. A portion of the heat pulse is released into the D_2O from ejecta sites. The remaining heat is released into the lattice, where it continues to expand hemispherically outward through the lattice, reaching its outer edge at 90 nm. As the heated portion of the lattice reaches the melting point of the target foil, 1825 K for Pd, it forms a melt zone – a footprint – that removes most old sites remaining from

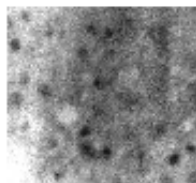


Figure 4. SEM photo of a Pd target foil, 1 mm square, showing ejecta sites with single DD fusion events for an acoustic pulse in the MHz range.

previous cycles. The sum of the heat released into the D_2O and the lattice is 20 ± 10 MeV, consistent with the 23.8 MeV of the alpha-producing event.

(G) While still in the foil, the alpha picks up two electrons from the plasma to form 4He .

(H) The helium atoms are ejected into, and carried along and distributed with, the flow of the circulating D_2O and argon gas.

5. Conclusion

I conclude that the experimental results show the occurrence of the fusion process ($2D$, 4He), producing $(43 \pm 3) \times 10^{-13}$ J of energy per event. (A similar treatment for the T measurements and its decay to 3He is understood [10].) Theoretical analysis suggests that this process is enabled by the compression of deuterons and electrons squeezed to astrophysical densities of about 1ps duration. The compression is produced by the combination of a high-frequency acoustic pulse and a magnetically contained plasma comprised of the compressed deuterons and electrons to form BE condensates that terminate in the single-event fusion process and heat release. Corresponding results and analysis apply to T measurements and its decay into 3He [10].

Acknowledgements

This paper was a joint effort by Richard Spitzer who upon gaining some knowledge of sonofusion decided to write an explanation of my work in his words with my help.

Appendix

The author has many scanning-electron-microscope photos of target foils in various stages of heat-produced damage, and many videos and DVDs showing the temporal experimental progression and the actual melting or disintegration of the target foils discussed in refs. [8–12,14,15]. The extent of target-foil damage depends on the foil thickness and element composition, and resonant frequency and amplitude of Q_a .

Thomas used an adapted low-mass, KEV MS to measure 4He in the presence of Ar and D_2 in the gas from the resonator during two weeks of testing in 1991–1992 at SRI [1]. The sampled gas at vacuum conditions was pre-treated by passing it from the bubbler to an evacuated 25 ml glass bulb, as shown in [7]; then through 60 g of heated CuO powder, removing hydrogen. The pre-treated gases were passed through an LN trap, removing the Ar and D_2O , and into the MS for analysis. Thomas found 4He at a 2-sigma level.

Davidson analyzed gas samples for 4He in 1992 at the Amarillo facility [2]. As in the SRI method, the sampled gases from the resonator were pre-treated by being passed through a heated granular CuO bed and collected in evacuated 25 ml glass bulbs. Gas standards from the Ar supply (gas prior to interacting with the acoustic pulse) and from the resonator (post interaction with the acoustic pulse) were shipped to Amarillo for analysis. There were fewer than 2

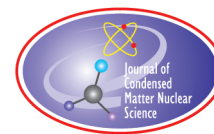
ppm of ^4He in the Ar supply, well below the 5 ppm generally accepted for helium in background air. Davidson found ^4He at 20 ppm in the sampled gases from the resonator. This represents a partial pressure of the total ^4He present. No complementary calorimetry measurements were made.

In May and June, 1994, T. Claytor, D. Tuggle, R. Stringham, and R. George at Los Alamos National Laboratory (LANL) prepared seven gas samples in 50 ml stainless-steel sampling cylinders for analysis: three samples from target-foils runs and four standards. At 20 kHz, no gammas were observed using Geiger-Muller counters during sonofusion runs. The sample gases were not pre-treated. The target-foil experiments were performed using the M2 20 kHz resonator described in Section 3. The gas samples were then shipped to B. Oliver for the He analysis at the Rocketdyne facility [3]. The foil gases were cleaned in a 12-inch long $\frac{1}{4}$ -inch diameter charcoal-packed “U” tube column, before injection into the MS chamber. This absorbed the hydrogen and froze out the Ar and D_2O vapors. Oliver used three successive aliquot injections, determining the ^4He present in each aliquot by the technique described in Section 3. The three measurements showed consistent results, 552 ± 1 ppm. These measurements were complemented by a calorimetric measurement of 65 W for the 19 h run, matching the counted number of alphas, 552 ± 1 ppm. The ^4He results were reported in “Helium Analysis of Target Metals”, B.M. Oliver, 1994.

References

- [1] D. Thomas, Retired, Senior Mass Spectroscopist, Analysis Dept., Physical Science Division, Stanford Research International, 333 Ravenswood, Menlo Park, CA, USA, from 1991–1992. This data is in my possession.
- [2] T. Davidson, and Staff, ^4He analysis, Helium Field Operations, U.S. Department of Interior, U.S. Bureau of Mines, 801 S. Fillmore, Amarillo TX, USA, see USBM report RI 9010, from 1993 to 1994. Some data was presented orally at ICCF 5.
- [3] B.M. Oliver, DOE, Helium 3 and 4 MS analysis, Rocketdyne International, Canoga Park, CA., from 1994 to 1995. Oliver is now at DOE, Battle, Hanford, WA.
- [4] M.H. Miles and B.F. Bush, Search for anomalous effects involving excess power and helium during D_2O electrolysis using palladium cathodes, *ICCF-3 Proc., Frontiers of Cold Fusion*. H. Ikegami (Ed.), Nagoya, Japan, 1992, pp. 189–200.
- [5] A. DeNinno, A. Frattolillo, A. Rizzo, F. Scaramuzzi and C. Alessandrini, A new method aimed at detecting small amounts of helium, in *A Gaseous Mixture, in ICCF-8 Proc.*, F. Scaramuzzi (Ed.), Lerici, (La Spezia), Italy, 2000, pp. 29–36.
- [6] M.C.H. McKubre, F.L. Tanzella, P. Tripodi, D. Di Gioacchino and V. Violante, Finite element modeling of the transient calorimetric behavior of the MATRIX experimental apparatus: ^4He and excess of power production correlation through numerical results, in *ICCF8 Proc.*, F. Scaramuzzi (Ed.), Lerici, (La Spezia), Italy, 2000, pp. 23–27.
- [7] J. W. Brian Clarke, Brian M. Oliver, Michael C.H. McKubre, Francis L. Tanzella and Paolo Tripodi, Search for ^3He and ^4He in arata-style palladium cathodes II: evidence for tritium production, *Fusion Sci. Technol.* **40** (2) (2001) 152–167.
- [8] During two weeks of testing the M1 sonofusion device at LANL in 1993–1994 we looked for product ash in the sonofusion device with the help of Tom Claytor and Dale Tuggle of the LANL Tritium Lab; other LANL personnel assisted in looking for T, ^4He , gamma, beta, neutron and other possible radiative products using BF_3 , NaI, Ge, and Geiger-Muller detectors.
- [9] R.S. Stringham, Cavitation and fusion, in *ICCF 10 Proc.* (Ed.) Hagelstein and Chubb, USA, CMNS, 2003, pp. 233–246.
- [10] R.S. Stringham, Sonofusion produces tritium that decays to helium three, *CMNS Proc. 15*, Rome Italy, V. Violante and F. Sarto (Eds.), 2009, pp. 57–64.
- [11] R.S. Stringham, Low mass 1.6 MHz sonofusion reactor, *Proc. ICCF-11*, Marseille, France, J.P. Biberian (Ed.), (2004), pp. 238–252.
- [12] R.S. Stringham, When bubble cavitation becomes sonofusion, *J. Cond. Matter Nucl. Sci.* **6** (2012) 1–12. <http://www.google.com/search?client=safari&rls=en&q=When+Bubble+Cavitation+Becomes+Sonofusion&ie=UTF-8&oe=UTF-8>
- [13] A review of Rusi Taleyarkhen work and Bubble Fusion R.F. Service, *Science* **311**, 17 Mar. 2006.
- [14] R. Stringham, *ACS Publications Low-Energy Nuclear Reactions Sourcebook*, Vol. 2, Jan Marwan and Steve Krivit (Eds.).
- [15] R.S. Stringham, Model for electromagnetic pulsed BEC experiments, *JCMNS vol.8, Proc. ICCF 16*, Chennai, India, M. Srinivasan and J.-P. Biberian (Eds.), 2011, pp. 75–90.

- [16] A. Bass, S. Ruuth, C. Camara, B. Merriman and S. Putterman, S. molecular dynamics of extreme mass segregation in a rapidly collapsing bubble, *Phy. Rev. Lett.* **101** (2008) p. 234301.
- [17] R.S. Stringham, The cavitation micro accelerator , *ICCF-8 Proc.*, F. Scaramuzzi ed. Lerici, (LaSpezia), Italy, 2000, pp. 299–304.
- [18] N.M. Lawandy, Interaction of charged particles on surfaces, *Appl. Phy. Lett.* **95** (2009) 234101-1-3.



Research Article

Low-energy Nuclear Reactions Driven by Discrete Breathers

V.I. Dubinko*

NSC Kharkov Institute of Physics and Technology, Kharkov 61108, Ukraine

Abstract

A new mechanism of LENR in solids is proposed, which is based on the large amplitude anharmonic lattice vibrations, a.k.a. intrinsic localized modes or “discrete breathers” (DBs). In particular, so called gap DBs, which can arise in diatomic crystals such as metal hydrides, are argued to be the LENR catalyzers. The large mass difference between H or D and the metal atoms provides a gap in phonon spectrum, in which DBs can be excited in the H/D sub-lattice resulting in extreme dynamic closing of adjacent H/D atoms ($\sim 0.01 \text{ \AA}$) required for the tunneling through the nuclear Coulomb barrier. DBs have been shown to arise either by thermal activation at elevated temperatures or by knocking atoms out of equilibrium positions under non-equilibrium gas loading conditions, employed under radiolysis or plasma deposition methods. The DB statistics in both cases are analyzed, and an attempt is made to quantify part of the vibrational problem in terms of electrochemical current or ion flux, connecting them with external excitation of DBs that act as *nano-colliders of deuterons*, triggering LENR. Resulting analytical expressions (under a selected set of material parameters) describe quantitatively the observed exponential dependence on temperature and linear dependence on the electric (or ion) current. Possible ways of engineering the nuclear active environment based on the present concept are discussed.

© 2014 ISCMNS. All rights reserved. ISSN 2227-3123

Keywords: Anharmonic lattice vibrations, Discrete breathers, Nuclear fusion, Quantum tunneling

1. Introduction

Copious experimental data on low-energy nuclear reactions assisted by the crystalline environment [1–3] leave little doubt about the reality of LENR, but a comprehensive theory of this phenomenon remains a subject of debate [2–4]. Some of the proposed models try to modify conventional nuclear physics by introducing various types of transient quasi-particles and structures such as the Hydrino, Hydron, Hydrex, etc. that were expected to lower the Coulomb barrier. Other, less radical, models point out at the possibility of screening of the Coulomb barrier by atomic electrons. Comprehensive reviews can be found in refs [2–4]. However, none of these models can explain even qualitatively all salient conditions required for LENR, which have been summarized by McKubre et al. [2] as follows.

LENR observed in heavy water electrolysis at palladium cathodes requires the simultaneous attainment of four conditions: (i) high loading of D within the Pd lattice; (ii) an initiation time at least ten times larger than the D diffusion time constant; (iii) a threshold electrochemical surface current or current density that is not correlated to the

*E-mail: vdubinko@mail.ru

bulk D loading; (iv) deuterium flux plays an important role in determining the excess heat power density. The first two requirements can be understood as thermodynamic preconditioning needed to bring D atoms within Pd lattice as close as possible. But the most “mysterious” requirements, from the point of view of current models, are *triggering mechanisms* (iii) and (iv), which do not depend on the *loading mechanisms* (i) and (ii). One can cite the conclusion by McKubre et al. on this issue: [2] “It is not at all clear how effectively the electron charge transfer reaction or the adsorption/desorption reaction couple energy into modes of lattice vibration appropriate to stimulate D + D interaction.”

The present paper is aimed, first of all, at answering this question. Its main argument is that in crystals with sufficient anharmonicity, a special kind of lattice vibration, namely, *discrete breathers* (DBs), a.k.a. intrinsic localized modes, can be excited either thermally or by external triggering, in which the amplitude of atomic oscillations greatly exceeds that of harmonic oscillations (phonons) [5–15]. Due to the crystal anharmonicity, the frequency of atomic oscillations increases or decreases with increasing amplitude so that the DB frequency lies outside the phonon frequency band, which explains the weak DB coupling with phonons and, consequently, their *robustness* even at elevated temperatures. DBs have been successfully observed experimentally in various physical systems [8] and materials ranging from metals to diatomic insulators [9], and they have been proposed recently as *catalyzers for various chemical reactions* in solids [16–18]. This field of research is mainly new, and it lies at the conjunction of nonlinear physics with material science. The main message of the present paper is that DBs present a viable *catalyzing mechanism for the nuclear reactions* in solids as well, due to the possibility of extreme dynamic close approaching of adjacent atoms, which is required for tunneling through the Coulomb barrier.

This paper is organized as follows. In the next section, a short review of the DB properties in metals and diatomic crystals is presented based on results of molecular dynamic (MD) simulations, using realistic many-body interatomic potentials. In Section 3, a rate theory of DB excitation under thermal heating and under non-equilibrium gas loading conditions (radiolysis or plasma deposition) is developed, and the average rate of D–D “collisions” in DBs is evaluated. In Section 4, tunneling through the Coulomb barrier with an account of electron screening is discussed, and the tunneling coefficient is presented as a function of the barrier width. This is the only section where conventional *nuclear physics* is employed. It is shown to be just one link in the chain of mechanisms required for the realization of LENR. In Section 5, combining the tunneling coefficient with the rate of D–D “collisions” in DBs, the LENR energy production rate is evaluated as a function of temperature, ion (electric) current and material parameters, and compared with experimental data. The results are discussed in Section 6 and summarized in Section 7.

2. Discrete Breathers in Metals and Diatomic Crystals

Discrete breathers are spatially localized large-amplitude vibrational modes in lattices that exhibit strong anharmonicity [5–8]. They have been identified as exact solutions to a number of model nonlinear systems possessing translational symmetry. [8] They have been successfully observed experimentally in various physical systems [8,9]. Presently the interest of researchers has shifted to the study of the role of DBs in solid state physics and their impact on the physical properties of materials [9,16–20].

The evidence for the existence of DB was provided by direct atomistic simulations, e.g. molecular dynamics (MD). Until recently, this was restricted mainly to one and two-dimensional networks of coupled nonlinear oscillators employing oversimplified pairwise interatomic potentials [6–8]. Studies of the DBs in three-dimensional systems by means of MD simulations using realistic interatomic potentials include ionic crystals with NaCl structure [10], graphene [12], carbon nanotubes [13] and metals [14,15,20].

2.1. Metals

For a long time, it has been assumed that the softening of atomic bonds with increasing vibrational amplitude is a general property of crystals, which means that the oscillation frequency decreases with increasing amplitude. There-

fore DBs with frequencies above the top phonon frequency were unexpected. However, in 2011, Haas et al. [14] have provided a new insight into this problem by demonstrating that the anharmonicity of metals appears to be very different from that of insulators. The point is that the essential contribution to the *screening* of the atomic interactions in metals comes from *free electrons* at the Fermi surface. As a consequence, the ion–ion attractive force may acquire a nonmonotonic dependence on the atomic distance and may be enhanced resulting in an amplification of even anharmonicities for the resulting two-body potentials. This effect can counteract the underlying softening associated with the bare potentials with a moderate increase of vibrational amplitudes to permit the existence of DBs above the top of the phonon spectrum. MD simulations of lattice excitation in fcc nickel as well as in bcc niobium and iron using realistic many-body interatomic potentials have proven that stable high-frequency DBs do exist in these metals [14,15]. Notably, the excitation energy of DBs can be relatively small (fractions of eV) as compared to the formation energy of a stable Frenkel pair in those metals (several eV). Moreover, it has been shown that DBs in Fe (and most likely in other transition metals) are highly mobile, hence can efficiently transfer a concentrated vibrational energy over large distances along close-packed crystallographic directions [15,20]. Recently, a theoretical background has been proposed to ascribe the interaction of moving DBs (a.k.a ‘quodons’ – quasi-particles propagating along close-packed crystallographic directions^a) with defects in metals to explain the anomalously accelerated chemical reactions in metals subjected to irradiation. Irradiation may cause continuous generation of DBs inside materials due to *external lattice excitation*, thus ‘pumping’ a material with DB gas [18,19].

In order to understand better the structure and properties of standing and moving DBs, consider the ways they are externally excited in Fe by MD simulations [20]. The key feature of the procedure is the initial displacement of the two adjacent atoms from their equilibrium position along the close $\langle 111 \rangle$ direction, which should oscillate in the *anti-phase mode* with respect to each other, thus forming a stable DB, as shown in Fig. 1 (a). The initial offset displacement d_0 determines the DB amplitude and oscillation frequency and, ultimately, its lifetime. DBs can be excited in a narrow frequency band $(1 \div 1.4) \times 10^{13} \text{ s}^{-1}$ just above the Debye frequency of bcc Fe, and DB frequency grows with increasing amplitude as expected from the “hard” type anharmonicity of the considered vibrational mode. Application of a displacement larger than 0.45 \AA generates a chain of *focusons*, while a displacement smaller than 0.27 \AA does not provide enough potential energy for the two oscillators to initiate a stable DB and the atomic oscillations decay quickly by losing its energy to *phonons*. The most stable DBs can survive up to 400 oscillations, as shown in Fig. 1 (b), and ultimately decay in a stepwise quantum nature by generating bursts of phonons, as has been predicted by Hizhnyakov as early as in 1996 [22].

The movement of a DB can be induced by translational kinetic energy E_{tr} given to the two central DB atoms in the same direction along the x -axis. Their velocities range from about 300 to 2000 m/s while travel distances range from several dozens to several hundreds of atomic spaces, depending on the d_0 and E_{tr} [20]. Figure 2 (a) shows a DB approaching the atoms with index 3415 and 3416. The two atoms pulsate in the *anti-phase mode* for about 1ps (~ 10 oscillations) and then oscillations cease but they are resumed at the subsequent atoms along the x -axis. In this way, the DB moves at a speed of 2.14 km/s, i.e. about the half speed of sound in bcc Fe. The translational kinetic energy of the DB is about 0.54 eV, which is shared among two core atoms, giving 0.27 eV per atom. This is very close to the initial kinetic energy $E_{\text{tr}} = 0.3 \text{ eV}$ transmitted to the atoms to initiate the DB movement. The deviation of the potential energy of the atoms from the ground state during the passage of the DB is presented in Fig.2b. The amplitude of the energy deviation can reach almost 1 eV. In an oversimplified ‘thermodynamic’ analogy, a moving DB can be viewed as an atom-size spot heated up to 10^4 K propagating through the crystal at sub-sonic speed.

^aIt should be noted that Russell and Eilbeck [21] have presented experimental evidence for the existence of quodons that propagate at great distances in atomic-chain directions in crystals of muscovite, an insulating solid with a layered crystal structure. Specifically, when a crystal of muscovite was bombarded with alpha-particles at a given point at 300 K, atoms were ejected from remote points on another face of the crystal, lying in atomic chain directions at more than 10^7 unit cell distances from the site of bombardment.

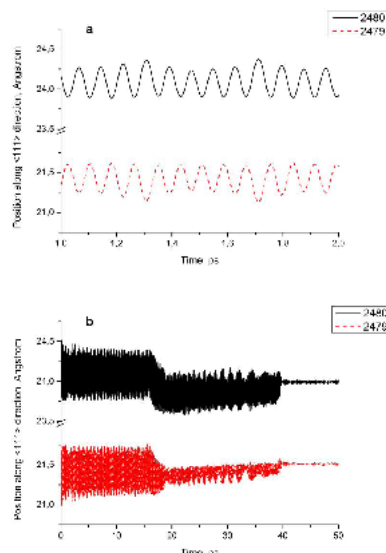


Figure 1. Oscillation of x coordinate of two neighboring atoms, 2480 and 2479 in a [111] row in Fe in a “standing” DB excited with $d_0 = 0.325$ Å: (a) initial stage of DB evolution; (b) all stages of DB evolution showing a stepwise ‘quantum’ nature of its decay.

DB excitations in [20] were done in a cell with initial and boundary conditions imitating a perfect crystal at the lattice temperature of 0 K, i.e. when all other atoms were initially at their lattice positions and had zero initial velocities. This poses an important question on the effect of lattice temperature and the crystal size on the robustness of DBs, since the most successful LENR experiments were conducted at temperatures above 300 K and employed metal-based (such as Pd, Pt or Ni) small (or even nanosized) particles. Recently, Zhang and Douglas [23] investigated the interfacial dynamics of Ni nanoparticles at elevated temperatures exceeding 1000 K and discovered a string-like collective motion of surface atoms with energies in the electron-volt range, i.e. exceeding the average lattice temperature by an order of magnitude. One of the most intriguing observations of this study was the propagation of the *breather excitations* along the strings, providing a possible mechanism for driving the correlated string-like atomic displacement movements. The authors conclude that these dynamic structures might be of crucial significance in *relation to catalysis*.

Various electrolytic reactions which can proceed during the course of absorption/desorption at the cathode surface can be a source of the vibrational energy required for the formation of DBs in the subsurface layer (see e.g. [4] p. 664 and discussion in the present paper). It should be noted that, based on the MD modeling results, only a fraction of an electron-volt may be sufficient to initiate a moving DB along any of the 12 close-packed directions $\langle 110 \rangle$ in fcc Pd sub-lattice.

In heavily deuterated palladium, a compound PdD forms where each octahedral site of the fcc-Pd structure is occupied by one D atom (thus forming another fcc sub-lattice: Fig. 3) and where the lattice constant expands by 6%. Moving DBs may be produced in the D sub-lattice as well. The nearest-neighbor separation between D atoms in PdD is 2.9 Å, while the equilibrium distance between two D atoms inside one octahedral site (in the hypothetical crystal PdD₂) is 0.94 Å, as demonstrated by the *ab initio* density-functional calculations [24]. Thus, the equilibrium distance between two D atoms is increased by 0.2 Å from the gas value of 0.74 Å, which makes the LENR extremely improbable for any *equilibrium configuration* of D atoms in the palladium lattice. However, a dynamic closing of

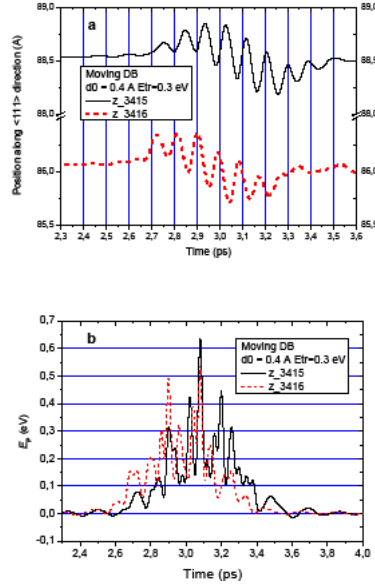


Figure 2. (a) Oscillation of x coordinate of two neighbouring atoms, 3415 and 3416 in a [111] row in Fe during the passage of a moving DB ($d_0 = 0.4$ Å, $E_{tr} = 0.3$ eV); (b) deviation of the potential energy of the atoms from the ground state during the passage of DB [20].

two D atoms performing *anti-phase oscillations* in a DB within a deuterium sub-lattice cannot be excluded, as will be demonstrated in the following subsection.

2.2. Diatomic crystals

Oscillation frequencies of the DBs in ionic crystals are found to be in the gaps of the phonon spectrum, being essentially dependent on *long-range forces*. This means that disregarding the long-range polarization effects, which cause a strong broadening of the optical phonon band, results in a totally unrealistic value of the DB frequency in the optical band of

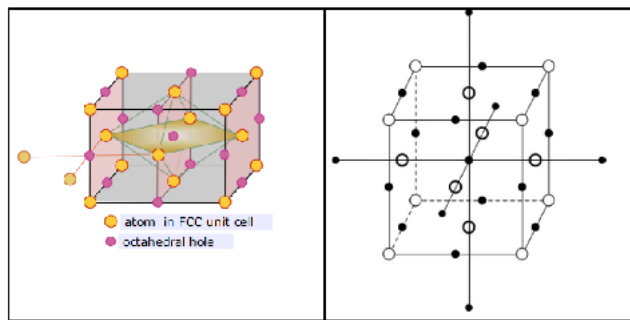


Figure 3. Left: PdD crystal structure. Right: the crystal with NaCl structure modeled in [10]. Heavy (light) atoms are shown by open (filled) circles. Adapted from [10], Copyright APS.

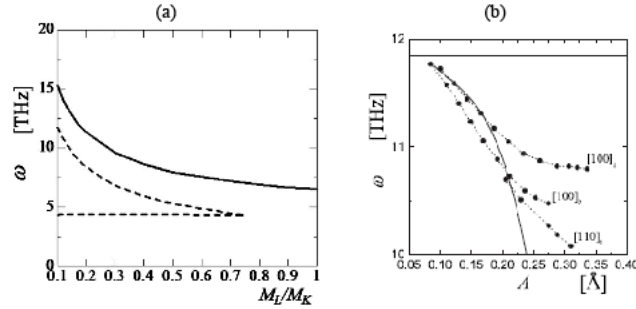


Figure 4. (a) The maximum frequency ω (solid line) and edges of the gap (dashed line) of the phonon spectrum, as the functions of the mass ratio, M_L/M_K . (b) Frequencies, as the functions of the DB amplitudes, A , for the DBs of three types: $[110]_1$, $[100]_1$, and $[110]_2$, excited by simulations [10] for $M_L/M_K = 0.1$ where figures in brackets describe polarization and the subscript indicates the number of the atoms oscillating with large amplitude. Solid line gives $\omega(A)$ found for the DB $[100]_1$ in frame of the single degree of freedom model developed in [10]. Horizontal line gives the upper edge of the phonon gap. Adapted from [10], Copyright APS.

the real phonon spectrum [25]. So, only a correct account of the localized anharmonic forces with long-range harmonic forces can produce an adequate description of DBs.

PdD has the NaCl structure, which consists of two face-centered cubic lattices with lattice parameter a , one occupied by the light and another one by the heavy ions, displaced with respect to each other by the vector $(a/2, 0, 0)$ as shown in Fig. 3. In order to preserve its identity, a DB must have oscillation frequency and its entire higher harmonics lying outside the phonon bands of the crystal lattice. MD simulations have revealed that diatomic crystals with Morse interatomic interactions typically demonstrate a *soft type* of anharmonicity [10], which means that a DB's frequency decreases with increasing amplitude, and one can expect to find only so-called gap DBs with frequency within the phonon gap of the crystal. A necessary condition of existence of such DBs is the presence of a sufficiently *wide gap* in the phonon spectrum of the crystal, which can be expected in crystals with components having sufficiently different atomic weights. The atomic weight ratio effect on the properties of DBs was studied by Khadeeva and Dmitriev [10] who used interatomic parameters that are not related to any particular crystal but give stable NaCl structure and realistic values of interaction energies, lattice parameter, vibrational frequencies, etc. This makes their results relevant also in the case of PdD even though the explored weight ratio was in the range of 1–0.1, i.e. considerably larger than the D/Pd weight ratio of 0.019. It means that the weight difference in the PdD case is larger by a factor of 5 than the maximum difference considered in [10].

Figure 4(a) clearly shows that the gap width grows with decreasing weight ratio M_L/M_K , so it might be expected to be wider in the case of PdD. The DBs were excited in [10] simply by shifting one *light atom* or two neighboring light atoms from their equilibrium positions while all other atoms were initially at their lattice positions and had zero initial velocities, similar to the DB excitation procedure employed in [20] for Fe. Breather's initial amplitude, d_0 , was taken from the range $0.01a < d_0 < 0.05a$, where $a = 6.25\text{Å}$ is the equilibrium lattice parameter of the NaCl structure. In this way, for the minimal weight ratio $M_L/M_K = 0.1$, three types of stable DBs have been excited, frequencies of which are shown in Fig. 4(b) as the functions of their amplitudes. One can see that the maximum DB amplitude was about 0.35Å (similar to the iron case [20]), which could bring two adjacent light atoms with initial spacing $b = \sqrt{2}a/2 \approx 1.77\text{Å}$, as close as to the distance of $\sim 1\text{Å}$, which, although being much smaller than any phonon-induced closing, is not yet sufficient for tunneling. However, numerical results on the gap DB in NaI and KI crystals has shown that DB amplitudes along $\langle 111 \rangle$ directions can be as high as 1Å , and the lifetimes can be as long as 10^{-8}s (more than 20000 oscillations) [6]. Besides, decreasing the weight ratio down to the PdD value of 0.019 can

be expected to decrease the minimum attainable spacing within a DB down to a fraction of an angstrom, but such MD modeling has not been tried so far.

Another principle question concerns the mechanisms of excitation and the properties of gap DBs at elevated temperatures. This problem was studied by Kistanov and Dmitriev [26] for the different weight ratios and temperatures. Density of phonon states (DOS) of the NaCl-type crystal for the weight ratio $M_L/M_K = 0.1$ at temperatures ranging from 0 to 620 K is shown in Fig. 5 (a–d). A small decrease in the gap width of the phonon spectrum with increasing temperature is observed. The appearance of two additional broad peaks in the DOS at elevated temperatures (starting from $T = 310$ K) is observed. One of them is arranged in the gap of the phonon spectrum, while another one lies above the phonon spectrum. The appearance of the peak *in the gap* of the phonon spectrum can be associated with the spontaneous excitation of gap DBs at sufficiently high temperatures, when nonlinear terms in the expansion of interatomic forces near the equilibrium atomic sites acquire a noticeable role. In connection with this, it has been concluded that as the temperature increases, if the difference in weights of anions and cations is sufficiently large, the lifetime and concentration of gap DBs in the crystal with the NaCl structure increase. The appearance of the peak *above* the phonon spectrum at sufficiently high temperatures can be associated with the excitation of DBs of another type, which manifest *hard nonlinearity*.

Figure 5(f) shows DOS for PdD and PdH based on the force constants obtained from the Born von Karman model [27], which quantitatively reproduces the intensity distribution in the experimental $S(Q, E)$ spectrum of PdD obtained in [28] at deuterium pressure of 5 GPa and $T = 600$ K. A slight discrepancy between the calculated and experimental spectra of the second and higher optical bands in PdD suggests a certain *anharmonicity of D vibrations* in these bands [28]. Quantitative estimates [28] show the anharmonicity of the potential well for D atoms at energies as low as ~ 0.1 eV, counting from the bottom of the well.

High-temperature excitation of DBs has been demonstrated also for the two-dimensional crystal of A_3B composition with long-range Morse interactions [11]. The lifetime of high-energy atoms was measured for various temperatures for two atomic weight ratios, $M_A/M_B = 0.1$ and 0.46 . In the first case, the crystal supported gap DBs in the sub-lattice of light atoms, whereas in the other case there were no DBs in the crystal due to the absence of the gap in the phonon spectrum. Figure 6 shows atomic displacements and DB frequency as the function of its amplitude, which can be as large as 1.3 \AA for one oscillating atom at zero Kelvin. This means that two adjacent atoms oscillating in the anti-phase mode could span 2.6 \AA (which equals the lattice parameter of the A_3B crystal) and bring the two atoms

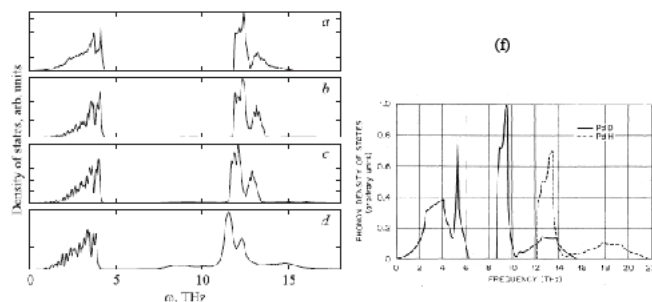


Figure 5. DOS of the NaCl-type crystal for the weight ratio $M_L/M_K = 0.1$ at temperatures $T =$ (a) 0, (b) 155, (c) 310, and (d) 620 K. Adapted from [26], Copyright APS. (f) DOS for PdD and PdH crystals based on the force constants obtained from the Born von Karman model [27], which quantitatively reproduces the intensity distribution in the experimental $S(Q, E)$ spectrum of PdD obtained in [28] at deuterium pressure of 5 GPa and $T = 600$ K. Adapted from [27] Copyright by APS.

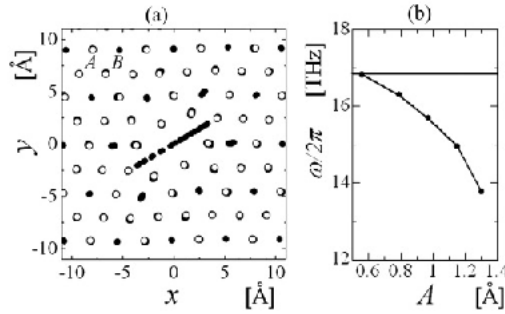


Figure 6. (a) Stroboscopic picture of atomic displacements in the vicinity of gap DB in the crystal A_3B with atomic weight ratio $M_B/M_A = 0.1$ at zero Kelvin. Open (solid) circles correspond to heavy “A” (light “B”) atoms. Displacements of atoms are multiplied by a factor of 4. (b) DB frequency as the function of its amplitude. The horizontal line indicates the upper edge of the phonon gap. Adapted from [11], Copyright APS.

quite close to each other. Excitation of such DBs has not been looked at, but the most important result of [11] is the demonstration of the “natural” thermally activated way of the DB excitation in a crystal under thermal equilibrium conditions. To do so the authors obtained a crystal at thermal equilibrium using a special thermalization procedure for 100 ps. After that the analysis of *thermal fluctuations* in the crystal was carried out within 200 ps. The temperature of the crystal was characterized by spatially (over the ensemble) and temporally averaged kinetic energy per atom, \bar{K} , as $T = \bar{K}/k_B$, where k_B is the Boltzmann constant. Atoms with kinetic energy $K_{A,n}, K_{B,n} > e\bar{K}$ were considered to be high-energy atoms, and their energies averaged over the lifetime were evaluated separately for heavy and light atoms. An example of the time evolution of the relative kinetic energy of a particular light atom, $K_{B,n}/\bar{K}$, is presented in Fig. 7 in the units of the DB’s oscillation period Θ for $\bar{K} = 0.1$ eV corresponding to the lattice temperature of 1160 K. The kinetic energy of the light atom, $K_{B,n}$, was averaged over time $0.18 \text{ ps} \approx 3\Theta$. In this example, the lifetime of the high-energy state of an atom is $t^*/\Theta \approx 70$, and its kinetic energy averaged over the lifetime is $K_{B,n}^*/\bar{K} \approx 5.1$. Analogously, high-energy heavy atoms were analyzed and concentrations of heavy and light high-energy atoms were evaluated. It appears that the average lifetime and concentration of *high-energy light atoms* increases exponentially

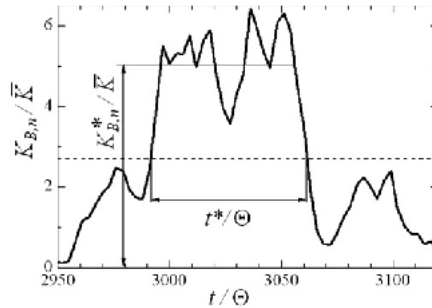


Figure 7. Relative kinetic energy of particular light atom, $K_{B,n}/\bar{K}$, as a function of dimensionless time, t/Θ where $\Theta = 0.06 \text{ ps}$ is the DB’s period. The kinetic energy of the light atom, $K_{B,n}$, was averaged over time $0.18 \text{ ps} \approx 3\Theta$. The horizontal dashed line indicates the level of kinetic energy equal to $e\bar{K}$, where $e \approx 2.7$ is the base of the natural logarithm. The lifetime of the high-energy state of the atom is $t^*/\Theta \approx 70$ and its kinetic energy averaged over the lifetime is $K_{B,n}^*/\bar{K} \approx 5.1$. Results are for $M_B/M_A = 0.1$ and $\bar{K} = 0.1 \text{ eV}$. Adapted from [11], Copyright APS.

with increasing average energy, \bar{K} , in a marked contrast to heavy atoms, which is consistent with the fact that only light atoms have large vibrational amplitudes in DBs. It is the amplitude rather than the energy of atomic vibrations that plays a key role in the triggering of LENR, since the probability of tunneling through the Coulomb barrier depends crucially on the separation of D ions before the tunneling (see Section 4), which can be drastically reduced in DBs due to the *specific combination of localized (anharmonic) and long-range (harmonic) forces*.

These findings are of primary importance for the concept of LENR driven by DBs, since they point out at the *two ways* of creation of the so called “nuclear active environment” (NAE, as defined by Storms [3]), which is associated with an *environment supporting DBs* in the present paper. The first way is *thermal activation* of DBs in the sub-lattice of D or H within the compound nanocrystal, in which the heavy component is represented by a suitable metal such as Pd, Pt, or Ni. This way seems to be the basic mechanism for the LENR observed, e.g. in specially treated nickel surface exposed to hydrogen at high temperatures (see refs. 76–79 in [3]). The second way is the DB excitation by *external triggering* such as the atomic displacements in the course of exothermic electrolysis at metal cathodes (majority of LENR experiments) or due to energetic ions, obtained by discharge in gas containing hydrogen isotopes (see refs. 48,49 in [3]). Naturally, both mechanisms may operate simultaneously under LENR conditions, and this synergy should be reflected in a viable model of DB excitation, the construction of which is attempted in the next section.

3. Rate theory of DB Excitation Under Thermal Equilibrium and External Driving

The rate equation for the concentration of DBs with energy E , $C_{DB}(E, t)$ can be written as follows [17]

$$\frac{\partial C_{DB}(E, t)}{\partial t} = K_{DB}(E) - \frac{C_{DB}(E, t)}{\tau_{DB}(E)}, \quad (1)$$

where $K_{DB}(E)$ is the rate of creation of DBs with energy $E > E_{\min}$ and $\tau_{DB}(E)$ is the DB lifetime. It has an obvious steady-state solution ($\partial C_{DB}(E, t)/\partial t = 0$):

$$C_{DB}(E) = K_{DB}(E) \tau_{DB}(E). \quad (2)$$

In the following sections we will consider the breather formation by thermal activation, and then extend the model to non-equilibrium systems with external driving.

3.1. Thermal activation

The exponential dependence of the concentration of high-energy light atoms on temperature in the MD simulations [11] gives evidence in favor of their thermal activation at a rate given by a typical Arrhenius law [7]

$$K_{DB}(E, T) = \omega_{DB} \exp\left(-\frac{E}{k_B T}\right), \quad (3)$$

where ω_{DB} is the natural frequency that should be close to the DB frequency. The breather lifetime has been proposed in [7] to be determined by a phenomenological law based on fairly general principles: (i) DBs in two and three dimensions have a minimum energy E_{\min} , (ii) The lifetime of a breather grows with its energy as

$$\tau_{DB} = \tau_{DB}^0 \left(\frac{E}{E_{\min}} - 1\right)^z$$

with z and τ_{DB}^0 being constants, whence it follows that under thermal equilibrium, the DB energy distribution function $C_{DB}(E, T)$ and the mean number of breathers per site $n_{DB}(T)$ are given by

$$C_{DB}(E, T) = \omega_{DB} \tau_{DB} \exp\left(-\frac{E}{k_B T}\right), \quad (4)$$

$$n_{\text{DB}}(T) = \int_{E_{\min}}^{E_{\max}} C_{\text{DB}}(E, T) dE = \omega_{\text{DB}} \tau_{\text{DB}}^0 \frac{\exp\left(-\frac{E_{\min}}{k_{\text{B}}T}\right)}{(E_{\min}/k_{\text{B}}T)^{z+1}} \int_0^{\frac{E_{\max}-E_{\min}}{k_{\text{B}}T}} y^z \exp(-y) dy. \quad (5)$$

Noting that

$$\Gamma(z+1, x) = \int_0^x y^z \exp(-y) dy$$

is the second incomplete gamma function, Eq. (5) can be written as [17]

$$n_{\text{DB}} = \omega_{\text{DB}} \tau_{\text{DB}}^0 \frac{\exp(-E_{\min}/k_{\text{B}}T)}{(E_{\min}/k_{\text{B}}T)^{z+1}} \Gamma\left(z+1, \frac{E_{\max}-E_{\min}}{k_{\text{B}}T}\right). \quad (6)$$

It can be seen that the mean DB energy is higher than the averaged energy density (or temperature):

$$\langle E_{\text{DB}} \rangle = \frac{\int_{E_{\min}}^{E_{\max}} C_{\text{DB}}(E, T) E dE}{\int_{E_{\min}}^{E_{\max}} C_{\text{DB}}(E, T) dE} \xrightarrow{E_{\max} \gg E_{\min}} \left(\frac{E_{\min}}{k_{\text{B}}T} + z + 1 \right) \times k_{\text{B}}T. \quad (7)$$

Assuming, according to [11] (Fig. 5), that $E_{\min}/k_{\text{B}}T \approx 3$ and $\langle E_{\text{DB}} \rangle \approx 5k_{\text{B}}T$, one obtains an estimate for $z \approx 1$, which corresponds to linear increase of the DB lifetime with energy.

3.2. External driving

The fluctuation activated nature of DB creation can be described in the framework of classical Kramers model, which is archetypal for investigations in reaction-rate theory [29]. The model considers a Brownian particle moving in a symmetric double-well potential $U(x)$ (Fig. 8(a)). The particle is subject to fluctuational forces that are, for example,

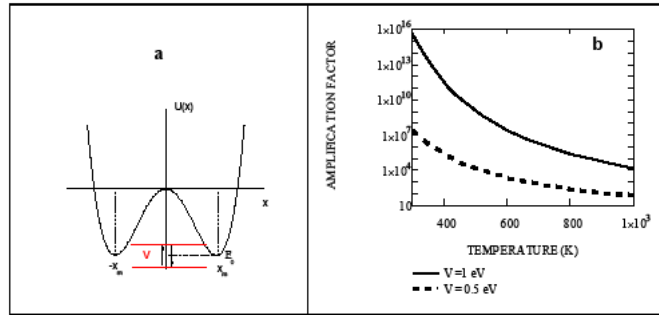


Figure 8. (a) Sketch of the double-well *potential landscape* with minima located at $\pm x_m$. These are stable states before and after the reaction, separated by a potential “barrier” with the height changing periodically or stochastically within the V band. (b) Amplification factor, $I_0 (V/k_{\text{B}}T)$, for the average escape rate of a thermalized Brownian particle from a periodically modulated potential barrier at different temperatures and modulation amplitudes, V [17]. .

induced by coupling to a heat bath. The fluctuational forces cause transitions between the neighboring potential wells with a rate given by the famous Kramers rate:

$$\dot{R}_K(E_0, T) = \omega_0 \exp(-E_0/k_B T), \quad (8)$$

where ω_0 is the natural frequency and E_0 is the height of the potential barrier separating the two stable states, which, in the case of fluctuational DB creation, corresponds to the minimum energy that should be transferred to particular atoms in order to initiate a stable DB. Thus, the DB creation rate (3) is given by the Kramers rate: $K_{DB}(E, T) = \dot{R}_K(E, T)$.

In the presence of *periodic modulation* (driving) of the well depth (or the reaction barrier height) such as $U(x, t) = U(x) - V(x/x_m) \cos(\Omega t)$, the reaction rate \dot{R}_K averaged over times exceeding the modulation period has been shown to increase according to the following equation [17]:

$$\langle \dot{R} \rangle_m = \dot{R}_K I_0 \left(\frac{V}{k_B T} \right), \quad (9)$$

where the amplification factor $I_0(x)$ is the zero order modified Bessel function of the first kind. Note that the amplification factor is determined by the ratio of the modulation amplitude V to temperature, and it does not depend on the modulation frequency or the mean barrier height. Thus, although the periodic forcing may be too weak to induce *athermal* reaction (if $V < E_0$), it can amplify the average reaction rate drastically if the ratio $V/k_B T$ is high enough, as it is demonstrated in Fig. 8(b).

Another mechanism of enhancing the DB creation rate is based on small *stochastic modulations* of the DB activation barriers caused by external driving. Stochastic driving has been shown to enhance the reaction rates via effective reduction of the underlying reaction barriers [18,19] as:

$$\langle \dot{R} \rangle = \omega_0 \exp(-E_a^{DB}/k_B T), \quad E_a^{DB} = E_0 - \frac{\langle V \rangle_{SD}^2}{2k_B T}, \quad (10)$$

where $\langle V \rangle_{SD}$ is the standard deviation of the potential energy of atoms surrounding the activation site.

Consider the periodic driving of the DB creation in more detail. It can be provided, e.g. by focusons or *quodons* formed by knocking of surface atoms out of equilibrium position by energetic ions or molecules under non-equilibrium deposition of deuterium, which may be sufficient to initiate a quodon propagating inside the material along a close-packed direction up to the depth equal to the quodon propagation range, l_q . The amplitude of the quasi-periodic energy deviation of metal atoms along the quodon pathway can reach almost 1 eV with the excitation time, τ_{ex} , of about 10 oscillation periods (Fig. 2). In the modified Kramers model (9), this energy deviation corresponds to the modulation of the DB activation barrier. Then, a *macroscopic* rate of generation of DBs of energy E_{DB} (per atom per second) may be written as follows:

$$\langle K_{DB} \rangle_{macro} = \omega_{DB} \exp \left(-\frac{E_{DB}}{k_B T} \right) \left(1 + \left\langle I_0 \left(\frac{V_{ex}}{k_B T} \right) \right\rangle \omega_{ex} \tau_{ex} \right), \quad (11)$$

where V_{ex} is the excitation energy and ω_{ex} is the mean number of excitations per atom per second caused by the flux of quodons, F_q , which is proportional to the electric current density, J , in the case of radiolysis (or to the ion flux, for the plasma deposition) and is given by

$$\omega_{ex}(F_q) = F_q b^2 \frac{4\pi R_P^2 l_q}{4\pi R_P^3 / 3} = F_q b^2 \frac{3l_q}{R_P}, \quad F_q(J) = \frac{1}{2} J, \quad (12)$$

where b is the atomic spacing, and so the product $F_q b^2$ is the frequency of the excitations per atom within the layer of the quodon propagation of a thickness l_q , while the ratio $3l_q/R_P$ is the geometrical factor that corresponds to the relative number of atoms within the quodon range in a PdD particle of a radius R_P . The coefficient of proportionality

between F_q and the electron flux J/e (where e is the electron charge) assumes that each electrolytic reaction that involves a pair of electrons, releases a vibrational energy of ~ 1 eV, which is sufficient to generate one quodon with energy $V_q \approx V_{ex} < 1$ eV. Multiplying the DB generation rate (11) by their lifetime τ_{DB} and the oscillation frequency ω_{DB} one obtains the mean frequency of D–D “collisions” in DBs (per atom per second) as a function of temperature, electric current density and material parameters listed in Table 1:

$$W_{D-D}(T, J) = (\omega_{DB})^2 \tau_{DB} \exp\left(-\frac{E_{DB}}{k_B T}\right) \left(1 + \left\langle I_0 \left(\frac{V_{ex}}{k_B T}\right) \right\rangle \omega_{ex}(J) \tau_{ex}\right), \quad (13)$$

Figure 9 shows that the DB-induced mean frequency of D–D “collisions” grows linearly with electric current density and exponentially with temperature, which results in a deviation from the linear dependence of W_{D-D} on J , if temperature increases with increasing electric current density.

In this way, DBs can provide up to 10^{25} “collisions” per cubic cm per second, which can be regarded as sufficient to penetrate the Coulomb barrier and initiate LENR, provided that the minimum D–D spacing attainable within DBs is sufficiently small. In the next section we estimate the required spacing by evaluating the tunneling coefficient as a function of the barrier width, with account of electron screening.

4. Tunneling with Account of Electron Screening

The tunneling coefficient (TC) first derived by Gamow (1928) for a pure Coulomb barrier is the Gamow factor, given by

$$G \approx \exp\left\{-\frac{2}{\hbar} \int_{r_1}^{r_2} dr \sqrt{2\mu(V(r) - E)}\right\}, \quad (14)$$

where $2\pi\hbar$ is the Plank’s constant, E is the nucleus CM energy, μ is the reduced mass, r_1, r_2 are the two classical turning points for the potential barrier, which for the D–D reaction are given simply by $\mu = m_D/2$, $V(r) = e^2/r$.

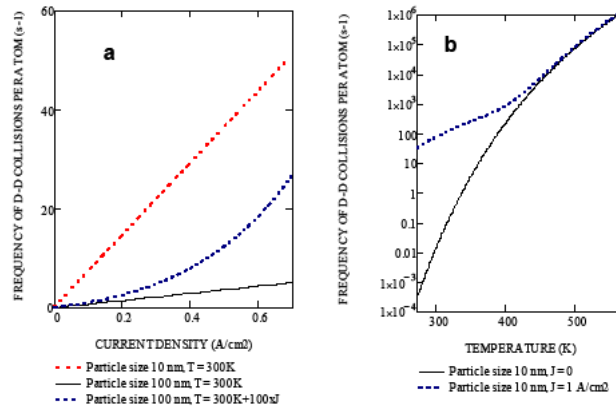


Figure 9. Mean frequency of D–D “collisions” in DBs as a function of electric current density, temperature assuming material parameters listed in Table 1.

For two D's at room temperature with thermal energies of $E \sim 0.025$ eV, one has $G \sim 10^{-2760}$, which explains a pessimism about LENR and shows a need for possible mechanisms of electron shielding of the barrier in a solid.

We will use a conventional model of a spherical shell of radius R of negative charge surrounding each D, which results essentially in a shifted Coulomb potential

$$V(r) = e^2 \left[\frac{1}{r} - \frac{1}{R} \right], \quad r_n \leq r \leq R, \quad (15)$$

where $r_n \ll R$ is the nuclear well radius. In this model, one has a modified TC ([4] p. 620)

$$G^*(R) = \exp \left\{ -\frac{2\pi e^2}{\hbar} \sqrt{\frac{\mu}{2(E + e^2/R)}} \right\}, \quad (16)$$

which depends crucially on the D ions spacing before the tunneling, as shown in Fig. 10. This model is the simplest both conceptually and computationally, so it cannot be expected to give an *exact* value, which can differ from the model values by many orders of magnitude. But this model demonstrates the most important property of the electron screening, namely, the *equivalence of the deuteron kinetic energy needed for the tunneling and the screening depth, R* : they enter into denominator of Eq. (16) as a sum $E + e^2/R$, which means that decreasing screening depth R increases the tunneling probability as strongly as increasing the deuteron's energy up to the level of e^2/R . It can be seen that in the angstrom range expected in any equilibrium D–D structure, the tunneling probability is too low for practical applications, but it picks up ~ 100 orders of magnitude with R decreasing down to 0.01 Å. This R range is lower by almost two orders of magnitude than the range of *conventional chemical forces*, but it is higher by three orders of magnitude than the range of *nuclear forces*, and the main hypothesis of the present paper is that it can be attainable in DBs due to the *specific combination of localized (anharmonic) and long-range (harmonic) forces*. Based on this hypothesis, the LENR energy production rate is evaluated in the next section as a function of temperature and electric current density and compared with experimental data.

It should be noted that the reaction rate per deuteron–deuteron pair evaluated in the next section, based on Eq. (16), does not take into account many physical effects, such as the volume factor and nuclear potential, which could result in corrections to the reaction rate of 5–6 orders of magnitude. However, one can see that changing the screening depth

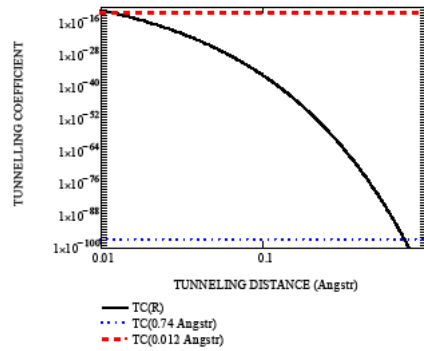


Figure 10. Tunneling coefficient dependence on the tunneling distance R for two deuterons with thermal energies of $E \sim 0.025$ eV. The horizontal lines correspond to $R = 0.74$ Å (equilibrium D–D spacing in D_2 molecule) and to $R = 0.012$ Å (minimum dynamic spacing required for LENR by the DB mechanism).

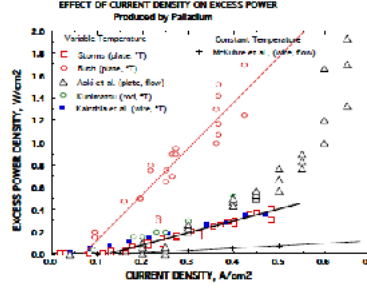


Figure 11. Comparison between several studies showing the effect of current density on power density [3].

by only 0.01 Å results in the change of the tunneling probability by 5 orders of magnitude, and so making the model more complex does not seem to make it more accurate.

5. LENR Energy Production Rate Under Heavy Water Electrolysis

We consider the following reaction [2]



which is based on experimentally observed production of excess heat correlated with production of a “nuclear ash”, i.e. ${}^4\text{He}$ [2,3]. Multiplying the DB-induced mean frequency of D–D “collisions” (13) by the tunneling probability in each collision (16) and the energy $E_{D-D} = 23.8 \text{ MeV}$, produced in D–D fusion one obtains the LENR power production rate per atom, P_{D-D} :

$$P_{D-D}(T, J) = W_{D-D}(T, J) G^* (R_{DB}) E_{D-D}. \quad (18)$$

Usually, experimentalists measure the output power density per unit surface of a macroscopic cell, P_{D-D}^S , as a function of the electric current density, as demonstrated by many researchers (see e.g. [3] p. 77) and illustrated in Fig. 11. This is given by the product of P_{D-D} , the number of atoms per unit volume, $1/\omega_{PdD}$ (ω_{PdD} being the atomic volume of PdD) and the ratio of the cell volume to the cell surface:

$$P_{D-D}^S(T, J) = \frac{P_{D-D}(T, J)}{\omega_{PdD}} \frac{L_S^3}{L_S^2} = P_{D-D}(T, J) \frac{L_S}{\omega_{PdD}}, \quad (19)$$

where L_S is the cell size, if cubic, or thickness, in case of a plate.

Figure 12 shows the LENR output power density DBs as a function of electric current density and temperature evaluated by Eq. (19) assuming material parameters listed in Table 1. Comparison of Fig. 12 (a) with experimental data (Fig. 11) shows that the present model describes quantitatively the observed linear dependence of P_{D-D}^S on the current density at a constant temperature as well as the deviation from the linear dependence, if temperature increases with increasing electric current density. Thermally activated nature of the reactions leading to LENR has been noted for quite a long time (see e.g. [3] p. 76: In general, the larger the temperature, the more excess energy is reported), and the activation energy was estimated in some cases to be $\sim 15 \text{ kcal/mol} \approx 0.65 \text{ eV}$. The present model not only explains these observations, but reveals that the underlying physics is a consequence of the synergy between thermally activated and externally driven mechanisms of the DB excitation in deuterated palladium, which results in a violation of the classical Arrhenius law and in the renormalization of the underlying activation energies [17].

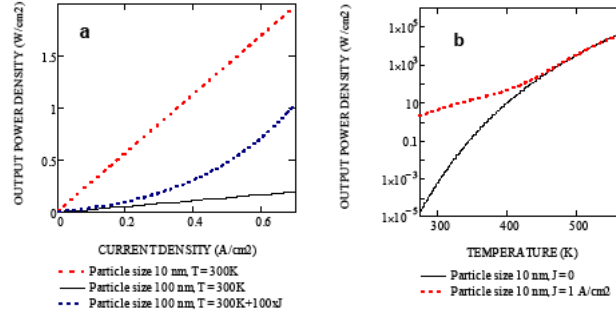


Figure 12. LENR output power density as a function of electric current density and temperature evaluated by Eq. (19) assuming material parameters listed in Table 1.

It should be noted that among the material parameters listed in Table 1 the most important is the minimum attainable D–D spacing in DBs, R_{DB} , since its increase from the fitted value of 0.012 \AA by one order of magnitude, to 0.1 \AA suppresses the LENR rate by 23 orders of magnitude (Fig. 13) which could not be compensated by any choice of other material parameters within the framework of the present model.

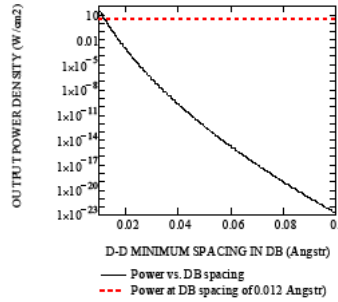


Figure 13. LENR output power density as a function of D–D minimum spacing in DBs evaluated by Eq. (19) at $J = 1 \text{ A/cm}^2$, $T = 300 \text{ K}$ assuming material parameters listed in Table 1.

6. Discussion

In the introduction we cited the problem formulated by McKubre et al. [2] concerning the coupling of the adsorption/desorption reaction energy into modes of lattice vibration appropriate to stimulate $\text{D} + \text{D}$ interaction. Indeed, in spite of a number of models trying to take into account the phonons, i.e. packets of wave-energy present in a lattice, as the LENR drivers (see e.g. refs to Hagelstein, Swartz, and F. S. Liu in [3]), one could not help feeling that something important was missing in the theory. Phonons were expected to move energy between nuclei, thereby creating enough localized energy to overcome the Coulomb barrier. But phonons are plane harmonic waves, essentially *delocalized* in the crystal, and the amplitude of atomic vibrations in the harmonic range does not exceed $\sim 0.1 \text{ \AA}$, which is abso-

Table 1. Material and DB parameters used in calculations

Parameter	Value
D–D equilibrium spacing in PdD, b (Å)	0.29
D–D minimal dynamic spacing in DB, R_{DB} (Å)	0.012
DB minimal activation energy, E_{min} (eV)	0.1
Mean DB energy, E_{DB} (eV)	1
DB oscillation frequency, ω_{DB} (THz)	10
Mean DB lifetime, $\tau_{DB} = 100/\omega_{DB}$ (s)	10^{-11}
Quodon excitation energy $V_q \approx V_{ex}$ (eV)	0.8
Quodon excitation time, $\tau_{ex} = 10/\omega_{DB}$ (s)	10^{-12}
Quodon propagation range, $l_q = 10b$ (nm)	2.9
Cathod size/thickness (mm)	5

lutely insufficient for bringing atoms closely enough for any significant tunneling (Fig. 13), whatever the underlying mathematics is. In contrast to phonons, DBs, also known as *intrinsic localized modes*, are essentially localized atomic vibrations that have large amplitudes of ~ 1 Å, which, at least in principle, can bring atoms very close to each other in the anti-phase oscillation mode. DBs can be excited either thermally at sufficiently high temperatures (which are above the temperature range of typical radiolysis) or by external triggering producing atomic displacements in the subsurface layer, which facilitate the DB creation.

In this view, the first two LENR requirements: (i, ii) high loading of D within the Pd lattice and long initiation time, can be understood as preconditioning needed to prepare PdD particles of small sizes out of initially bulk Pd crystal, in which DBs can be excited, and the requirements (iii, iv) on the D flux and electric current density, are natural prerequisites for the DB creation by the input energy transformed into the lattice vibrations.

The importance of the Fermi-Pasta-Ulam type of energy localization in nano-PdD particles was stressed also by Ahern [30]: Energy localized vibrational modes are so large that they can break and reform bonds. Locally, the vibrations act like very hot regions with active chemistry. Ahern sustained that the phenomenon of localization of energy could even explain the triggering of LENR in nanostructures saturated with hydrogen/deuterium, which is confirmed by the present model. In this connection, it should be noted that for the first time to our knowledge, the idea to link the nonlinear mechanisms of energy localization in the forms of quodons with the Lattice Assisted Nuclear Fusion (LANF), was expressed by Russell and Eilbeck at the LENCOS-09 conference in 2009, which proceedings were published in 2011 [31]. It was suggested that once a quodon is created then atoms of high speed are repeatedly brought close together in head-on collisions without expenditure of energy. If this happened in a crystal containing deuterium, then there would be an enhanced finite probability for fusion to occur, no matter how small the fusion cross-section might be. The proposed LANF mechanism was based on rather high quodon energies (up to ~ 300 eV) with essentially unlimited lifetimes (and propagation ranges) that could be excited in a LiD *crystal ring* by external driving. Although estimates [31] lead the authors to conclude that the contribution of quodons to additional fusion was negligible, the expressed ideas gave a strong motivation for further research in this direction to the present author. While more recent MD modeling of DBs in real crystals demonstrated the importance of *low-energy atomic collisions* (\sim eV) as drivers of LENR via the DB excitation.

An important implication of the present theory is that it may be helpful in selecting a frequency interval for the terahertz stimulation of DBs in deuterated palladium, similar to the method by Letts and Hagelstein [32] of stimulation of optical phonons by a laser. The stimulation was provided by tuning dual lasers to one of three specific beat frequencies, which were believed to correspond to the frequencies of optical phonons of deuterated palladium. Indeed, the excess power has been produced peaking at frequencies of 8, 15 and 20 THz. However, the comparison of these frequencies with experimentally verified DOS for PdD crystals [27,28], shows that the first frequency corresponded to the *gap in the phonon spectrum* of PdD while the last two frequencies were *above the phonon band*, as demonstrated in

Fig. 5(f). So the results [32] give some evidence in favor of the laser-induced stimulation of the “soft” gap DBs as well as of the “hard” high-frequency ones. It should be noted here that the position of the phonon gap may be questioned due to the uncertainty connected with the extent of D loading in the experiment [32], but the existence of the highest resonance peak at ~ 20 THz present a puzzle for the phonon mechanism of LENR. On the other hand, the appearance of high-frequency (hard-type) breathers in NaCl type crystals at elevated temperatures was discussed and demonstrated recently in [11] (see Fig. 5 (d)). This problem clearly needs further investigations as well as the perspective way of the laser-induced stimulation of DB creation in nuclear (i.e. breather) active environment.

Probably the most serious criticism of the present theory may be due to the extremely small D–D separation $R_{DB} \approx 0.012 \text{ \AA}$ that should be attainable within DBs in order to provide the tunneling probability required to fit the experimental data. Such distances are larger than those, at which nuclear forces operate, by three orders of magnitude, but they are considerably smaller than the range of conventional chemical forces based on electronic properties. So the question arises whether electrons can be effective in screening the Coulomb barrier at distances small enough in order to significantly facilitate the nuclear tunneling? Recent experiments on fusion of elements in accelerators, analyzed in [33], give a positive answer to this question. The analysis is based on corrections to the cross section of fusion due to the screening effect of atomic electrons, obtained in so called Born-Oppenheimer static approximation by Assenbaum et al. [34]. Using this approach, it was shown that the so-called “screening potential” acts as additional energy of collision at the center of mass. Apparently, this approach is equivalent to taking into account the *reduced thickness* of the potential barrier in the calculation of the tunneling probability adopted in the present paper (Eq. (16)). However, other models for the fusion reaction rate should be considered in future, where the tunneling rate could be determined more adequately from the time average deuteron-deuteron overlap.

The screening potential for D–D fusion in platinum for deuterons with kinetic energy ranging from 4 to 23 keV was found to be $675 \pm 50 \text{ eV}$, which is 25 times larger than for free atoms of deuterium. This may mean that in a crystal of platinum, deuterons of such energies do not feel the Coulomb repulsion up to distances of 25 times smaller than the size of the deuterium atoms. The screening potential for palladium was reported to be $\sim 300 \text{ eV}$. These results provide experimental evidence in favor of the electron screening as such, but it should be stressed that they do not represent the complicated cooperative dynamics of ions and electrons in a DB. Indeed, the velocity of a deuteron accelerated up to 4 keV is about 10^8 cm/s , which exceeds the atomic velocities in DBs almost by three orders of magnitude. Such deuteron movement is too fast for effective electron screening, since Fermi electrons move at comparable speed, in contrast to the slow D movement in a DB, which allows electrons to follow ions adiabatically. Thus we may conclude that screening distances under DB conditions may be significantly smaller than those obtained under accelerator conditions, due to *specific combination of localized (anharmonic) and long-range (harmonic) forces* acting on deuterons under dynamic oscillation within a discrete breather. In a crude analogy, one can imagine a DB as a *nano-collider* of deuterons, which operates with energies within the electron-volt range rather than the kilo-electron volt range examined in the ‘low energy’ beam experiments. There is no analytical theory developed for these conditions, and the only data available so far could be obtained from the MD or *ab initio* modeling. So the minimal D–D dynamic spacing attainable in DBs should be regarded as an *adjustable parameter* of the model (all of which are listed in Table 1).

In the existing electrochemical loading models (see e.g. [35]), three reactions are used: the Volmer reaction, the Tafel reaction and the Heyrovsky reaction, which complicate a quantitative analysis of the vibrational energy produced during the loading. But it should be emphasized that only a fraction of an electron volt may be sufficient for the DB creation, and the experimentally confirmed presence of vacancies in PdD during electrolysis [34] gives evidence of that such energy is indeed deposited, since vacancies require $\sim 1 \text{ eV}$ to form in Pd. What is more, vacancies do not diffuse near room temperature by thermal activation; so the only way they can be formed in the Fleischmann–Pons experiments was thought to be through inadvertent codeposition of Pd at high loading [34]. The present concept offers an alternative explanation of the accelerated formation and diffusion of vacancies in crystals via DB-induced

acceleration of chemical reactions, as have been argued in [18]. So the present model simply assumes that each electrolytic reaction that involves a pair of electrons, releases a vibrational energy of ~ 1 eV, which is sufficient for the generation of one quodon, and the quodon flux accelerates thermally activated DB creation in sub-surface layers.

At first glance, the DB persistence and robustness even at high temperatures may seem astonishing. However, DBs do not radiate their energy in the form of small-amplitude waves because they vibrate at frequencies outside the phonon spectrum of crystal. DB frequency can leave the phonon spectrum when its amplitude is sufficiently large because the frequency of a nonlinear oscillator is amplitude-dependent. There are two types of nonlinearity, the hard-type and the soft-type. In the former case the DB frequency increases with increase in its amplitude, and in the latter case it decreases. In the case of the hard-type nonlinearity the DB frequency can be above the phonon spectrum. For the soft-type nonlinearity DBs can exist only if the phonon spectrum possesses a gap, which is the case e.g. in the crystals with the NaCl structure with large mass difference of atoms, *which is the case for the PdD crystal*. Numerical results on the gap DB in NaI and KI crystals has shown that DB amplitudes along $\langle 111 \rangle$ directions can be as high as 1 \AA , and the lifetimes can be as long as 10^{-8} s (more than 20 000 oscillations) [6]. So the mean DB lifetime (100 oscillations) and the excitation time (10 oscillations) assumed in the present model for a quantitative comparison with experiment are rather modest estimates based upon recent MD modeling of DBs using large scale classical MD simulations in 3D periodic bcc Fe [20]. Two well spread interatomic potentials (IAPs) have been checked, derived to account for the electronic charge distribution depending on the local atomic arrangement which are known to provide a good compromise between computationally expensive *ab initio* calculations and over-simplified pairwise potentials. What is more, the latest DFT (*ab initio*) calculations, which are independent from the choice of IAP, have shown that a standing DB in Fe can be stable up to 160 oscillations [36].

One of the fundamental questions concerning the robustness of DBs in metals is connected with phonon–electron relaxation in metals, which is one of the reasons behind the fast optical phonon relaxation in metals. In fact, the electron–phonon coupling is a basic mechanism of the DB creation in *thermal spikes* in metals produced by fast electrons and especially by fast heavy ions (with energy exceeding 1 MeV/amu) that lose their energy via the excitation of electron system rather than via collisions with crystal atoms [17]. Although DBs (similar to lattice phonons) may lose part of their energy to free electrons, they can also gain energy from the phonons. So a DB should be regarded as an open dissipative system rather than an isolated one, which provides a natural explanation of thermally activated creation of DBs at elevated and high temperatures demonstrated in recent works [11,23,26]. Besides, the realistic MD and especially DFT calculations take into account the electronic charge distribution adjusting adiabatically to the local atomic arrangement under DB conditions. Note, however, that in typical DFT simulations, the core electrons are kept frozen, which is fine for large atomic separations, as the interaction with neighbors is almost fully determined by the higher-energy, outer-lying electrons. However, in the case under consideration, one should use the Linearized Augmented Plane Wave Method (LAPW), which is an all electron DFT method.

A small size of PdD particles is required since the triggering of DB creation occurs due to the propagation of the vibrational energy from the surface (by quodons, focusons, etc.) down to some depth, and the smaller the particles, the more atoms can be involved in the DB creation, i.e. become “nuclear active”. This is manifested in the model by the inversely proportional dependence of the power output on the particle size (see expression (12) for excitation frequency ω_{ex} and Fig. 12 (a)). Storms [3] emphasizes that “not all small particles are nuclear-active, other factors must play a role as well”. From the point of view of the present model, this can be explained by two factors: (i) *impurity atoms* and (ii) *crystal disorder*. Impurity atoms can strongly affect the phonon spectrum of PdD. Although impurity atoms are localized and their concentration may be low, they may change the phonon spectrum of *the whole crystal* and extend it into the DB range, which would suppress the DB formation and make the particle “nuclear inactive” (or vice versa!). This consideration may be a useful tool in the search for the “nuclear active environment” (NAE), by the way of doping the Metal-D or Metal-H crystals with elements changing the phonon spectrum to mediate DB creation.

Another factor concerns the role of crystal disorder in LENR, which typically start after prolonged loading resulting

in formation of numerous defects, or occurs in specially prepared fine powders consisting of nanosized particles [2,3]. As noted by Storms [3], p. 123: “Cracks and small particles are the Yin and Yang of the cold fusion environment. Small particles are created between cracks and crack-like gaps are formed in the near-contact regions between small particles. The greater the numbers of cracks, the smaller are the isolated regions (particles) between cracks.” The present model offers the following hypothesis for the importance of the crystal disorder caused by structural defects and nano-dimensions of the particles.

Piazza and Sanejouand [37] reported a striking *site selectiveness* of energy localization in the presence of spatial disorder. In particular, while studying thermal excitation of DBs in protein clusters, they found that, as a sheer consequence of disorder, a *non-zero energy gap* for exciting a DB at a given site either exists or not.^b Remarkably, in the former case, the gaps arise as a result of the impossibility of exciting small-amplitude modes in the first place. In contrast, in the latter case, a small subset of linear edge modes acts as accumulation points, whereby DBs can be continued to arbitrary small energies, while unavoidably approaching one of such normal modes. Concerning the structure–dynamics relationship, the authors [37] found that the regions of protein structures where DBs form easily (*zero or small gaps*) were unfailingly the most highly connected ones, also characterized by weak local clustering. This result means that the process of loading or special “nano-treatment” creates the disordered cluster structures, which may be enriched with sites of *zero or small gaps* for the DB excitation. Such sites are expected to become the nuclear active sites, according to the present model. The most important consequence of this hypothesis is that it may offer the ways of *engineering* the nuclear active environment based on the MD modeling of DB creation in nanoparticles and disordered structures.

Finally, it is known that LENR have been shown to produce excess heat and ^4He as the only significant “nuclear ash”, which is hard to explain in the framework of conventional nuclear physics. It has been argued that if a mechanism to overcome the Coulomb barrier is proposed, a mechanism to release the energy must be proposed at the same time, and these two mechanisms must be able to work together. The second mechanism may require modification of the known nuclear reactions, which is beyond the scope of the present paper, and has been discussed extensively, e.g. in a recent review [38]. However, the author believes that the method to overcome the Coulomb barrier proposed in the present paper is more important from a practical point of view, since it may suggest new ways of engineering the NAE by preparing relevant cluster structures so that to facilitate in them creation of discrete breathers as the most constitutive catalyzer of LENR.

7. Summary

A new mechanism of LENR in solids is proposed, in which DBs play the role of a catalyzer via extreme dynamic closing of adjacent H/D atoms required for the tunneling through the Coulomb barrier. DBs have been shown to arise either via thermal activation at elevated temperatures or via knocking atoms out of equilibrium positions under non-equilibrium gas loading conditions, employed under radiolysis or plasma deposition methods.

The present mechanism explains all the salient LENR requirements: (i, ii) long initiation time and high loading of D within the Pd lattice as preconditioning needed to prepare small PdD crystals, in which DBs can be excited more easily, and (iii, iv) the triggering by D flux or electric current, which facilitates the DB creation by the input energy transformed into the lattice vibrations.

An attempt is made to quantify part of the vibrational problem in terms of electrochemical current or ion flux and to connect it with external triggering of the DB creation subsequently leading to the triggering of LENR. Simple analytical expressions for the cold fusion energy production rate are derived as the functions of temperature, ion (electric) current

^bFor a long time it was known that in two-dimensional and three-dimensional *perfect lattices* there is always a *non-zero* energy gap for exciting a DB [7].

and material parameters. These expressions (under a selected set of material parameters) describe quantitatively the observed exponential dependence on temperature and linear dependence on the electric (or ion) current.

The present results are based only on the *known physical principles* and on independent atomistic simulations of DBs in metals and ion crystals using realistic many-body interatomic potentials. Further research in this direction is needed and planned in order to verify the proposed mechanism by atomistic simulations of DBs in Metal-D and Metal-H systems. An outstanding goal of this research is to suggest new ways of *engineering the nuclear active environment* by preparing relevant cluster structures (by special doping and mechanical treatment) so as to facilitate in them creation of discrete breathers as the most constitutive *catalyzer* of LENR.

Acknowledgements

The author is grateful to Mike Russell who devoted his attention to the potential importance of anharmonic lattice vibrations in LENR, to Francesco Piazza for the note on breathers in disordered structures, to Juan Archilla for interesting discussions and to Vladimir Hizhnyakov for valuable criticism and hospitality during a stay at the Tartu University.

References

- [1] M. Fleischmann, S. Pons and M. Hawkins, Electrochemically induced nuclear fusion of deuterium, *J. Electroanal. Chem.* **261** (1989) 301–308 and errata in Vol. 263, 187–188.
- [2] M. McKubre, F. Tanzella, P. Hagelstein, K. Mullican and M. Trevithick, The need for triggering in cold fusion reactions, in *Tenth International Conference on Cold Fusion* MA: LENR-CANR.org., Cambridge, 2003.
- [3] E.K. Storms, *The Science of Low Energy Nuclear Reaction*, World Scientific, Singapore, 2007.
- [4] V.A. Chechin, V.A. Tsarev, M. Rabinovich and Y.E. Kim, Critical review of theoretical models for anomalous effects in deuterated metals, *Int. J. Theoret. Phys.* **33** (1994) 617–670.
- [5] A.J. Sievers and S. Takeno, Intrinsic localized modes in anharmonic crystals, *Phys. Rev. Lett.* **61** (1988) 970–973.
- [6] V. Hizhnyakov, D. Nevedrov and A.J. Sievers, Quantum properties of intrinsic localized modes, *Physica B* **316–317** (2002) 132–135.
- [7] F. Piazza, S. Lepri and R. Livi, Cooling nonlinear lattices toward energy localization, *Chaos* **13** (2003) 637–645.
- [8] S. Flach and A.V. Gorbach, Discrete breathers—Advances in theory and applications, *Phys. Rep.* **467** (2008) 1–116.
- [9] M.E. Manley, Impact of intrinsic localized modes of atomic motion on materials properties, *Acta Materialia* **58** (2010) 2926–2935.
- [10] L.Z. Khadeeva and S.V. Dmitriev, Discrete breathers in crystals with NaCl structure, *Phys. Rev. B* **81** (2010) 214306–1–214306–8.
- [11] L.Z. Khadeeva and S.V. Dmitriev, Lifetime of gap discrete breathers in diatomic crystals at thermal equilibrium, *Phys. Rev. B* **84** (2011) 144304–1 – 144304–8.
- [12] B. Liu, C.D. Reddy, J. Jiang, J.A. Baimova, S.V. Dmitriev, A.A. Nazarov and K. Zhou, Discrete breathers in hydrogenated graphene, *J. Phys. D-Appl. Phys.* **46** (2013) 305302–1–305302–9.
- [13] T. Shimada, D. Shirasaki, Y. Kinoshita, Y. Doi, A. Nakatani and T. Kitamura, Influence of nonlinear atomic interaction on excitation of intrinsic localized modes in carbon nanotubes, *Physica D* **239** (2010) 407–413.
- [14] M. Haas, V. Hizhnyakov, A. Shelkan and M. Klopov, Prediction of high-frequency intrinsic localized modes in Ni and Nb, *Phys. Rev. B* **84** (2011) 144303–1–144303–8.
- [15] V. Hizhnyakov, M. Haas, A. Shelkan and M. Klopov, Theory and molecular dynamics simulations of intrinsic localized modes and defect formation in solids, *Phys. Sci.* **89** (2014) 044003 (5pp).
- [16] V.I. Dubinko and F.M. Russell, Radiation damage and recovery due to the interaction of crystal defects with anharmonic lattice excitations, *J. Nucl. Materials* **419** (2011) 378–385.
- [17] V.I. Dubinko, P.A. Selyshchev and J.F.R. Archilla, Reaction-rate theory with account of the crystal anharmonicity, *Phys. Rev. E* **83**(4) (2011), doi: 10.1103/PhysRevE.83.041124.

- [18] V.I. Dubinko and A.V. Dubinko, Modification of reaction rates under irradiation of crystalline solids: contribution from intrinsic localized modes, *Nucl. Inst. and Methods Phys. Res. B* **303** (2013) 133–135.
- [19] V. Dubinko and R. Shapovalov, *Theory of a Quodon Gas. With Application to Precipitation Kinetics in Solids Under Irradiation*, Springer, Switzerland, 2014.
- [20] D. Terentyev, A. Dubinko, V. Dubinko, S. Dmitriev, E. Zhurkin, Interaction of discrete breathers with primary lattice defects in bcc Fe, *Europhys. Lett.*, Submitted.
- [21] F.M. Russell and J.C. Eilbeck, Evidence for moving breathers in a layered crystal insulator at 300 K, *Europhys. Lett.* **78** (2007) 10004–10012.
- [22] V. Hizhnyakov, Relaxation jumps of strong vibration, *Phys. Rev. B* **53** (1996) 13981–13984.
- [23] H. Zhang and J.F. Douglas, Glassy interfacial dynamics of Ni nanoparticles: Part II Discrete breathers as an explanation of two-level energy fluctuations, *Soft Matter* **9** (2013) 1266–1280.
- [24] Z. Sun and D. Tomanek, Cold fusion: How close can deuterium atoms come inside palladium?, *Phys. Rev. Lett.* **63** (1989) 59–61.
- [25] M. Haas, V. Hizhnyakov, M. Klopov and A. Shelkan, Effects of long-range forces in nonlinear dynamics of crystals: creation of defects and self-localized vibrations, in *11th Europhysical Conference on Defects in Insulating Materials (EURODIM 2010)* doi:10.1088/1757-899X/15/1/012045.
- [26] A.A. Kistanov and S.V. Dmitriev, Spontaneous excitation of discrete breathers in crystals with the NaCl structure at elevated temperatures, *Phys. Solid State* **54** (2012) 1648–1651.
- [27] J.M. Rowe, J.J. Rush, H.G. Smith, M. Mostoller and H.E. Flotow, Lattice dynamics of a single crystal of PdD_{0.63}, *Phys. Rev. Lett.* **33** (1974) 1297–1300.
- [28] V.E. Antonov, A.I. Davydov, V.K. Fedotov, A.S. Ivanov., A.I. Kolesnikov and M.A. Kuzovnikov Neutron spectroscopy of H impurities in PdD: Covibrations of the H and D atoms, *Phys. Rev. B* **80** (2009) 134302–1–134302–7.
- [29] P. Hanggi, P. Talkner and M. Borkovec, Reaction-rate theory: fifty years after Kramers, *Rev. Mod. Phys.* **62** (1990) 251–341.
- [30] B. Ahern, “Energy Localization, the key to understanding energy in nanotechnology and nature”, <http://lenr-canr.org/acrobat/AhernBSenergyloca.pdf>
- [31] F.M. Russell and J.C. Eilbeck, Persistent mobile lattice excitations in a crystalline insulator, In: *Discrete and Continuous Dynamical Systems – Series S*, Vol. 4, No. 5, 10.2011, pp. 1267–1285.
- [32] D. Letts and P.L. Hagelstein, Stimulation of optical phonons in deuterated palladium, in *ICCF-14 Int. Conf. on Condensed Matter Nucl. Sci.*, Washington, DC, 2008.
- [33] E.N. Tsyganov, Cold nuclear fusion, *Phys. Atomic Nuclei* **75** (2012) 153–159.
- [34] H.J. Assenbaum, K. Langanke and C. Rolfs, Effect of electron screening on low-energy fusion cross section, *Z. Phys. A* **327** (1987) 461–468.
- [35] S. Chubb and T. Dolan, Summary of the 2010 Colloquium on Lattice-Assisted Nuclear Reactions at MIT, <http://www.infinite-energy.com/images/pdfs/Colloquium2010.pdf>
- [36] V.I. Dubinko, D.A. Terentyev, S.V. Dmitriev, V. Hizhnyakov and A.J. Sievers, Discrete breathers in Iron: ab initio simulations and physical effects, to be published.
- [37] F. Piazza and Y.H. Sanejouand, Discrete breathers in protein structures, *Phys. Biol.* **5** (2008) 026001 (14pp) doi:10.1088/1478–3975/5/2/026001
- [38] V.F. Zelensky, Nuclear processes in deuterium/natural hydrogen – metal systems, Problems of atomic science and technology, **85**(3) (2013), Series: Nuclear Physics Investigations (60), pp.76–118.